Role of integrin-linked kinase (ILK) in vascularization of pancreatic islets and blood glucose homeostasis

Inaugural-Dissertation

zur Erlangung des Doktorgrades
der Mathematisch-Naturwissenschaftlichen Fakultät
der Heinrich-Heine-Universität Düsseldorf

vorgelegt von

Haiko Karsjens
aus Osnabrück

Düsseldorf, April 2020

aus dem Institut für Stoffwechselphysiologie
der Heinrich-Heine-Universität Düsseldorf

aus dem Institut für Vaskular- und Inselzellbiologie
am Deutschen Diabetes Zentrum

Gedruckt mit der Genehmigung der
Mathematisch-Naturwissenschaftlichen Fakultät der
Heinrich-Heine-Universität Düsseldorf

Berichterstatter:

1. Prof. Dr. Eckhard Lammert

2. Priv.-Doz. Dr. Volker Burkart

Tag der mündlichen Prüfung: 19.06.2020

Table of Content

1 Summary

Blood vessels are more than just tubes that carry oxygen and nutrients to, and carbon dioxide and waste products away from tissues. How the vascularization of a tissue is established during development and altered during disease are questions regarding fundamental biological processes, those mechanisms are not fully understood yet. A highly vascularized tissue is the pancreatic islet, which controls glucose homeostasis. Their endocrine cells are in close contact with the endothelial cells of the capillaries and enable vascularization during development as well as appropriate hormone release.

Angiogenesis describes the outgrowth of endothelial cells from an existing vasculature. The formation of new blood vessels is of critical importance in embryonic development as well as in physiological and pathophysiological processes in the adult. Pericytes extend long cytoplasmic processes that encircle the endothelial tube and ensure vascular homeostasis. Here, we present an optimized *in vitro* bead sprouting assay that enables pharmacologic manipulation of lumenized vascular sprouts composed of human endothelial cells wrapped by human pericytes. Our new assay can screen the effect of multiple compounds on angiogenesis simultaneously and our novel ImageJ plugin allows an automated analysis of sprout morphology as well as quantification of pericyte coverage.

Integrins expressed by beta cells facilitate the adhesion to the vascular basement membrane of capillaries. In a second project, we investigated the role of the β1 integrin-binding adaptor protein integrin-linked kinase (ILK) *in vitro* and *in vivo* in pancreatic islet cells. We found that ILK regulates cell cortex tension of islet cells, and thereby facilitates their adhesion to endothelial cells. Thus, ILK enables the vascularization of pancreatic islets and an immediate insulin secretion.

Furthermore, we studied the role of ILK as well as the intra-islet vasculature for beta cell function and proliferation in more detail. Therefore, we analyzed insulin-resistant mice with beta cell-specific *Ilk* deficiency. During the beginning of insulin resistance, beta cells compensate the increased metabolic demands by increasing their functional mass and their insulin release. We found that ILK supports beta cell proliferation during insulin resistance and is critical for insulin release during a glucose tolerance test.

In conclusion, my thesis provides a novel *in vitro* angiogenesis assay and an accompanying ImageJ plugin, which allows automated analysis of sprout morphology and pericyte coverage in a defined human cellular system. Additionally, our study is the first to consider the biomechanical properties of an epithelial tissue as a regulator for its vascularization. We show that in pancreatic islet cells, ILK controls the cell cortex tension and adhesion force to endothelial cells, which enable islet vascularization. Furthermore, ILK supports beta cell proliferation as well as insulin secretion during insulin resistance.

2 Zusammenfassung

Blutgefäße sind mehr als nur Röhren, die Sauerstoff und Nährstoffe zu, sowie Kohlendioxid und Abfallprodukte von den Geweben abtransportieren. Wie das Blutgefäßsystem innerhalb eines Gewebes während der Entwicklung entsteht und wie dieses sich während einer Krankheit verändert, sind Fragen bezüglich grundlegender biologischer Prozesse, deren Mechanismen bis heute noch nicht vollständig aufgeklärt sind. Die Langerhans-Inseln der Bauchspeicheldrüse haben ein dichtes Blutgefäßsystem, welches für die Regulation der Blutglukose Homöostase notwendig ist. Dabei stehen die hormonproduzierenden endokrinen Zellen in Verbindung mit den Endothelzellen der Blutgefäße und ermöglichen so die Vaskularisierung der Langerhans-Inseln sowie eine angemessene Hormonausschüttung.

Angiogenese bezeichnet das Aussprossen von Endothelzellen aus einem bereits vorhandenen Blutgefäß. Dies ist ein komplexer Prozess, der sowohl in der embryonalen Entwicklung als auch in physiologischen und pathologischen Prozessen von entscheidender Bedeutung ist. Perizyten bilden zusammen mit Endothelzellen die Kapillaren. Dabei umspannt ein Perizyt die Außenwand eines Blutgefäßes, sodass dieses stabilisiert wird. Wir stellen hier einen *in vitro* Angiogenese Assay vor, in dem sich einfache Blutgefäße, bestehend aus menschlichen Endothelzellen und Perizyten, bilden. Unser Angiogenese Assay ermöglicht das parallele Screening von Angiogenese-Inhibitoren und -Stimulatoren. Das dazugehörige ImageJ-Plugin ermöglicht eine automatisierte Analyse der Blutgefäß-Morphologie sowie der Perizytenabdeckung.

Betazellen exprimieren Integrine, welche die Adhäsion an die Basalmembran der Kapillaren vermitteln. In einem weiteren Projekt untersuchten wir die Rolle des β1 Integrin bindenden Proteins Integrin-Linked Kinase (ILK) *in vivo* und *in vitro* in Zellen der Langerhans-Inseln. Wir zeigen, dass ILK die Zellkortexspannung dieser Zellen reguliert und dadurch die Adhäsion an Endothelzellen ermöglicht. ILK fördert somit die Vaskularisierung der Langerhans-Inseln und eine sofortige Insulinsekretion, die zu Erhaltung der Blutglukose Homöostase notwendig ist.

Darüber hinaus untersuchten wir den Einfluss von ILK und der Blutgefäße innerhalb der Langerhans-Inseln auf die Funktion und Vermehrung von Betazellen. Dafür analysierten wir insulinresistente Mäuse mit einer betazell-spezifischen Deletion des *Ilk* Genes. Bei einer beginnenden Insulinresistenz kompensieren die Betazellen den erhöhten Stoffwechselbedarf durch eine Erhöhung der Zellzahl sowie der Insulinausschüttung. Wir zeigen, dass ILK die Betazellproliferation bei einer Insulinresistenz unterstützt und zudem für die Insulinsekretion während eines Glukosetoleranztests nötig ist.

Zusammenfassend beschreibt meine Dissertation einen neuen *in vitro* Angiogenese Assay und ein dazugehöriges ImageJ-Plugin, das eine automatisierte Analyse der Blutgefäße sowie der Perizytenabdeckung ermöglicht. Darüber hinaus ist unsere Studie die erste, die den

Einfluss der biomechanischen Eigenschaften eines Epithelgewebes für dessen Vaskularisierung berücksichtigt. Wir zeigen, dass die ILK in Zellen der Langerhans-Inseln die Spannung des Zellkortexes und die Adhäsion an Endothelzellen kontrolliert und dadurch die Vaskularisierung ermöglicht. Darüber hinaus unterstützt die ILK die Proliferation sowie die Insulinsekretion der Betazellen bei einer Insulinresistenz.

3 Annotation to this thesis

The results part of this thesis consists of three independent sections. Each section contains an autonomous scientific question and a series of experiments. The first two sections refer to published original research articles, while the third section describes follow-up experiments.

The first section shows the publication Eglinger et al.[1]. Here, an *in vitro* bead sprouting assay was extended by the presence of pericytes. Furthermore, a Fiji plug-in was developed that allows a standardized analysis of sprout morphology as well as pericyte coverage:

> J. Eglinger, **H. Karsjens** & E. Lammert – Quantitative assessment of angiogenesis and pericyte coverage in human cell-derived vascular sprouts – Inflammation and Regeneration 2017[1]
> Original research article

Next, the article Kragl et al.[2] is presented. This article demonstrates that the protein integrin-linked kinase (ILK) alters the biomechanical properties of pancreatic islet cells and thereby determines the location of their vasculature:

> M. Kragl*, R. Schubert*, **H. Karsjens***, S. Otter, B. Bartosinska, K. Jeruschke, J. Weiss, C. Chen, D. Alsteens, O. Kuss, S. Speier, D. Eberhard, D. Müller & E. Lammert – The biomechanical properties of an epithelial tissue determine the location of its vasculature – Nature Communications 2016[2]
> Original research article, *equally contributed

Finally, follow-up experiments that are based on the obtained results of Kragl et al.[2] are shown. Here, mice with *Ilk*-deficient beta cells were challenged by an induced insulin resistance. Subsequently, the role of ILK as well as the islet vasculature during beta cell compensation were analyzed.

Each section begins with its own background part, which offers essential information about the performed experiments. A results, discussion, methods and an additional information part including authors contributions complete each section. The references and abbreviations of all sections are combined at the end of this thesis (see section 8). To achieve consistency within the thesis, the numbering of figures and references were changed compared to the online version of the published articles.

4 Introduction

Merely a few centuries ago, the majority of the world population died from fatal diseases (e.g. pestilence) or famine. Thanks to scientists who made outstanding discoveries (e.g. antibiotics or vaccinations) and unveiled mechanisms of fatal diseases (e.g. smallpox) many diseases can be cured or are (almost) extinct nowadays. According to the World Health Organization (WHO) one of the fastest growing health challenges with an expected 51% increase and over 700 million people affected in the next years is diabetes[3, 4]. Since there is yet no cure for diabetes and its life-threatening complications, there is an urgent need for new therapies. Therefore, a better understanding of the underlying mechanisms of insulin producing beta cells, as well as the action of insulin on peripheral tissues are vitally needed.

4.1 The islets of Langerhans and beta cells

The pancreas is a glandular organ in the upper abdomen, encompassed by the spleen, liver, intestine and stomach (Figure 1). The main functions are the production of exocrine digestive enzymes and endocrine hormones which control blood glucose concentrations. With more than 95% the pancreas mainly consists of exocrine tissue that is built up predominantly by acinar and ductal cells[5, 6]. Acinar cells are arranged in grape like structures and produce digestive enzymes like trypsin, lipase or amylase and bicarbonate[5]. This enzyme cocktail, called pancreatic juice, is secreted into a network of ducts that issue via the *ampulla of Vater* into the duodenum of the small intestine[6]. Here these enzymes facilitate the breakdown and absorption of peptides, lipids and carbohydrates.

Endocrine cells account for approximately 1-2% of the pancreatic mass and secrete several hormones into the blood circulatory system[5]. They accumulate to island shaped clusters that are scattered throughout the exocrine pancreas (Figure 1). These clusters are termed islets of Langerhans named after their namesake, pathologist Paul Langerhans who was the first to describe pancreatic islets in 1869 in his medical dissertation: "...small cells of almost perfect homogeneous content and of a polygonal form, with round nuclei, mostly lying together in pairs or small groups"[7]. Around 1,000-5,000 islets (with diameters ranging from 10-350 µm) in rodents and 1,000,000-15,000,000 islets (20-160 µm diameter) in humans are distributed throughout the pancreas[8, 9]. The islets consist of five different endocrine cell types. In mice the islet core is build up by insulin secreting beta cells that account for ~75% of total islet cells. The beta cell core is surrounded by alpha cells (~19%), which represent the second largest endocrine cell population and secrete the counterplayer of insulin, glucagon. With ~6% delta cells, PP-cells and epsilon cells that produce and secrete somatostatin, pancreatic polypeptide and ghrelin, respectively are the less frequent cells in the islet periphery[10]. Besides hormone secreting cells other cell types such as nerves, fibroblasts, macrophages, dendritic cells and endothelial cells (ECs) are present in the islet[11]. These cells intermingle with the

endocrine cells. Human islets have no beta cell core, in contrast the endocrine cells seem to be randomly distributed throughout the islet[10]. Furthermore, the composition of human endocrine cells is more diverse compared to murine islets.

In summary, the pancreas is a gland covering exocrine and endocrine cells that overtake different physiological functions. On one hand it plays a crucial role in nutrient breakdown and absorption, and on the other hand it controls glucose homeostasis.

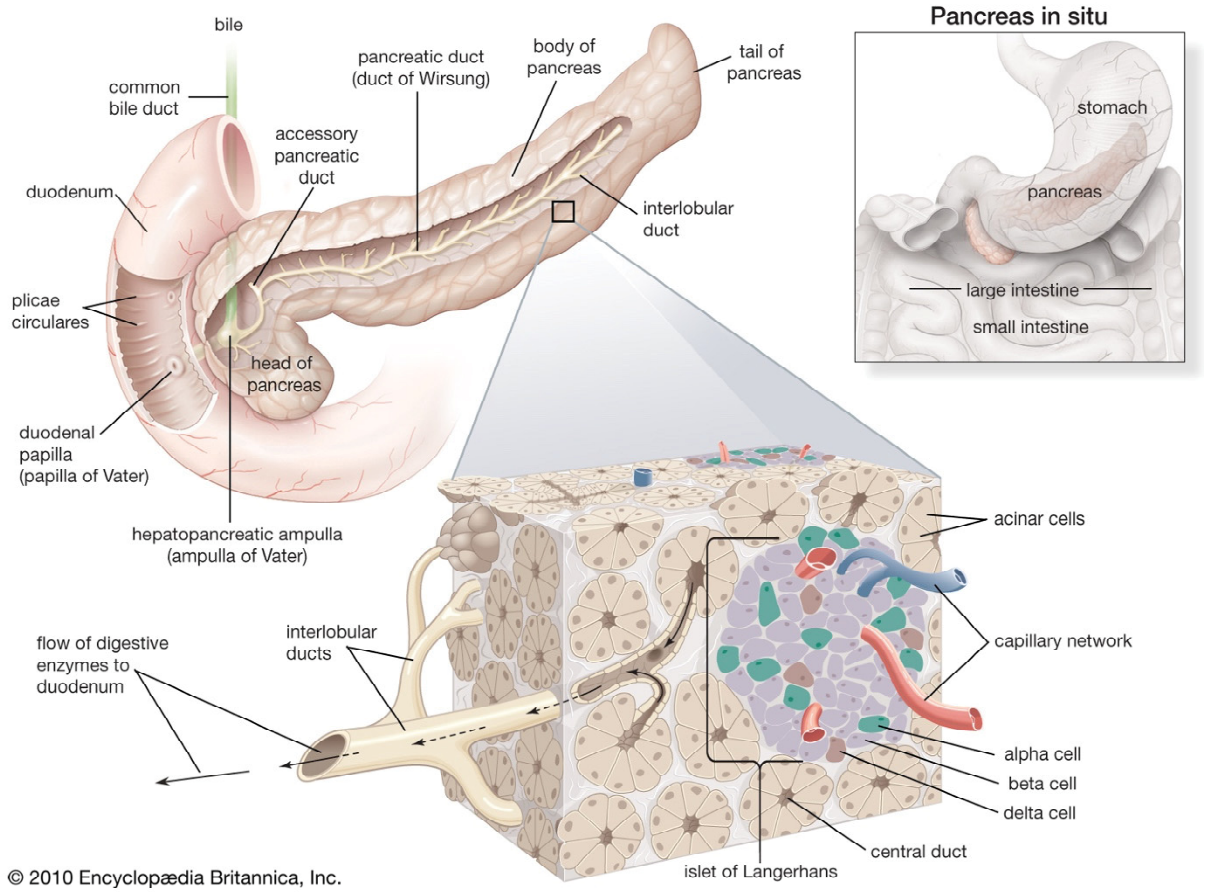

Figure 1: ***Overview of the pancreas and an islet of Langerhans.*** An overview of the anatomy of the pancreas plus a closeup on an islet of Langerhans. The main exocrine cell types like acinar cells and ductal cell as well as the endocrine alpha, beta and delta cells are shown. This image is taken from: Encyclopedia Britannica, Inc.[12].

4.1.1 Regulation of blood glucose homeostasis

As the main source of energy, mammalian cells are in constant need of glucose to function appropriately. Long lasting disturbances of blood glucose concentrations can lead to severe complications, meaning that just a few minutes of too low blood glucose concentrations (hypoglycemia) can cause acute brain injuries or death[13]. In contrast, extended high blood glucose concentrations (hyperglycemia) manifest ultimately into diabetes and cardiovascular complications[14]. Thus, blood glucose concentrations have to be kept in a narrow range, which is termed glucose homeostasis. To ensure that glucose concentrations stay within this narrow range the body has a sophisticated system that tightly regulates blood glucose levels.

Two counter regulatory hormones, secreted by the islets of Langerhans, play a key role in this balancing act: insulin and glucagon[5]. Insulin action causes decreasing blood glucose concentrations, whereas glucagon on the contrary leads to an increase of blood glucose levels. Beta cells synthesize and secrete insulin. After protein translation and maturation via the precursors preproinsulin and proinsulin, six insulin monomers assemble with two zinc and calcium ions to hexamers[15]. Insulin hexamers are stored in crystalline form in secretory vesicles at the plasma membrane. Every beta cell contains around 9,000-13,000 vesicles, pending to be released into the circulatory system during high blood glucose levels[16, 17]. After release, insulin action lowers blood glucose concentrations. Once the glucose concentration falls below a certain threshold, the release of the insulin antagonist glucagon is stimulated. Glucagon is secreted from alpha cells and induces among others hepatic glucose production that in turn leads to an increase of blood glucose concentrations[18]. The interplay between insulin and glucagon are the key factors maintaining glucose homeostasis.

The following paragraph describes the basic mechanism of glucose stimulated insulin secretion (GSIS). Beta cells are permanently sensing plasma glucose levels. Glucose enters the murine beta cell via the low affinity glucose transporter type 2 (GLUT2) isoform[19]. In human beta cells GLUT1 and GLUT3 are the predominant glucose transporters[20]. Cytosolic glucose enters the glycolysis pathway, where in the initial step glucose is phosphorylated by the enzyme glucokinase (hexokinase IV). Glucokinase has a relatively low affinity to glucose and is not inhibited by its product glucose-6-phosphate (G6P)[21]. The stable phosphorylation of glucose ensures a low intracellular glucose concentration and a continuous glucose influx, which enables equilibration of intracellular and extracellular glucose levels[20]. Glycolysis results in the production of ATP, NAD(H) and pyruvate. During aerobic conditions pyruvate is metabolized in the mitochondria to acetyl coenzyme A (acetyl-CoA) via the pyruvate dehydrogenase. Further breakdown of acetyl-CoA in the tricarboxylic acid cycle and additional oxidative phosphorylation of its products results in an increased ATP/ADP ratio. High cytosolic ATP concentrations lead to closure of ATP-sensitive potassium (K_{ATP}) channels[22]. The decrease of potassium (K^+) efflux leads to plasma membrane depolarization, which in turn opens voltage dependent calcium (Ca^{2+}) channels (VDCC), allowing influx of extracellular Ca^{2+} ions. Rise in intracellular calcium concentrations triggers the exocytotic fusion of insulin secretory vesicles with the plasma membrane and release of insulin into the circulatory system (see Figure 2).

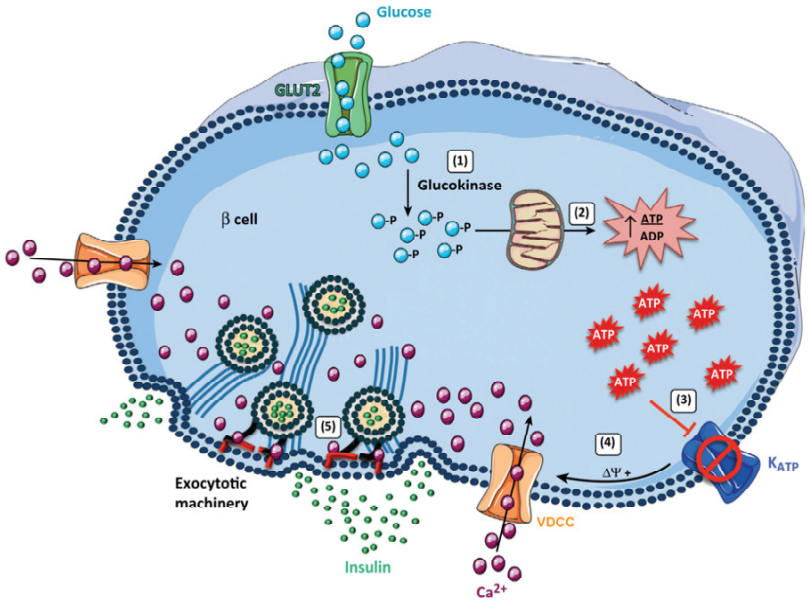

Figure 2: ***Basic mechanism of glucose stimulated insulin secretion (GSIS).*** Glucose enters the murine beta cell via GLUT2 and gets directly phosphorylated by glucokinase to G6P (1). Further metabolization via glycolysis pathway and the tricarboxylic acid cycle generates a numerous amount of ATP (2). Elevated ATP concentration triggers the closure of ATP-sensitive potassium (K_{ATP}) channels (3), causing membrane depolarization and opening of voltage dependent calcium (Ca^{2+}) channels (VDCC) (4). Calcium influx leads to exocytosis of secretory vesicles and release of insulin into the circulatory system (5). Modified from Mancini et al. 2013[23].

Glucose stimulated insulin secretion follows a biphasic time course that is most likely due to two different pools of insulin secretory vesicles. Shortly after elevation of blood glucose concentrations a rapid insulin secretion is observed, referred to as first phase of insulin secretion. This phase is followed by a second, prolonged phase of insulin release. The readily releasable pool (RRP) describes vesicles that are already pre-docked via SNARE (soluble N-ethylmaleimide-sensitive factor attachment protein receptor) and calcium-regulated proteins (e.g. Synaptotagmin) to the plasma membrane[24]. Granules of the RRP represent only a small fraction (1-5%), but release a rapid amount of insulin during the first phase of insulin secretion[25, 26]. The granules of the insulin reserve pool are situated at least one granule diameter away from the plasma membrane, and have to undergo chemical modification before refilling the RRP[26]. This may explain the second phase of insulin secretion, where insulin is secreted slowly and steadily until blood glucose concentrations lower to basal levels.

Although glucose is the main trigger for insulin secretion, beta cells also respond to the two other primary nutrient classes: amino acids and fatty acids. Amino acids can enhance or inhibit insulin secretion, depending on type and concentration of the amino acid (reviewed in Newsholme et al. 2007[27]). For example, the amino acids glutamate, alanine or glutamine activate mitochondrial metabolism, which results in an increased ATP production and thus enhances insulin secretion[28]. Besides glucose and amino acids, free fatty acids (FFA) also influence insulin secretion[29]. In beta cells, FFA can either enter the tricarboxylic acid cycle and

further increase ATP ratio and potentiate insulin secretion[30] or influence insulin secretion independent of the glucose metabolism. For example, long-chain FFAs bind to the free fatty acid receptor FFA1 (also known as GPR40), which is predominantly expressed on beta cells. Activation of FFA1 directly triggers the fusion of secretory vesicles with the plasma membrane[23]. FFAs can also induce fusion of secretory vesicles via activation of mammalian uncoordinated (Munc) proteins. The Munc protein family forms complexes with SNARE proteins that play a key role in vesicle exocytosis and insulin release[31, 32].

Beta cells do not only respond to increased nutrient levels but also to circulating hormones. For example, the endocrine pancreatic delta cells release somatostatin, a hormone that impairs insulin secretion of beta cells by suppression of (insulin vesicle exocytosis[25, 33]. On the contrary, non-pancreatic derived hormones, so called incretins, potentiate insulin secretion during hyperglycemia. The incretins glucagon like peptide 1 (GLP1) and glucose-dependent insulinotropic polypeptide (GIP) are produced by enteroendocrine L-cells or K-cells, respectively, and are released after food intake[34]. Incretins bind to their receptors, which are predominantly expressed on beta cells. Receptor activation leads to cyclic AMP production and protein kinase A activation, both influencing pathways that trigger insulin exocytosis[35].

To sum up, beta cells monitor blood nutrient levels and respond primarily to elevated blood glucose concentrations with the secretion of insulin. Furthermore, amino acids, fatty acids and hormones can induce insulin secretion. The interplay of insulin and glucagon ensures glucose homeostasis.

4.1.2 Action of insulin

Insulin is the main anabolic hormone and a key regulator for blood glucose homeostasis. High blood glucose levels trigger beta cells to secrete insulin into the circulatory system. Insulin acts mainly via binding to its insulin receptor (IR), which is predominantly expressed in muscle, liver and adipose tissue[36]. Binding of insulin to its receptor activates or inhibits several pathways and signaling cascades that lead in the end to a reduction of glucose, amino acid, and free fatty acid concentration in the blood[36].

The IR is a transmembrane receptor tyrosine kinase (RTK). It is a homodimer consisting of two extracellular α-chains (135 kDa), each linked via disulfide bonds to transmembrane β-chains (95 kDa), followed by two intracellular tyrosine kinase domains[37]. There are two isoforms of the IR, IR-A and IR-B, which are a result of alternative splicing[38]. IR-A and IR-B have the same affinity for insulin but differ in insulin growth factor (IGF) affinity. However, their functional and physiological roles are not fully understood.

Insulin binds to the extracellular domain of the IR, inducing receptor dimerization and activation of the cytosolic kinase domains[39]. The IR phosphorylates various substrates, and

initiates several signaling cascades, like the insulin receptor substrates (IRSs)[37]. IRSs act as docking sites for different signaling complexes regulating the expression and activation of a wide range of proteins. One key pathway activated by insulin via IRSs is the Phosphoinositide 3-kinase (PI3K) and Protein kinase B (also known as Akt) pathway. Both play a key role in multiple cellular processes such as glucose metabolism, apoptosis and proliferation[39]. Another key pathway controlled by IRSs is the MAPK/ERK pathway (also known as the Ras-Raf-MEK-ERK pathway) that is crucial for cell proliferation, differentiation and cytoskeletal organization[40].

The primary metabolic function of insulin is lowering blood glucose levels. Around 90% of glucose is taken up by skeletal muscle cells via the glucose transporter type 4 (GLUT4)[41]. During fasting only ~5% of GLUT4 is present at the cell surface. Most GLUT4 are stored intracellularly in specialized insulin-responsive GLUT4 storage vesicles (GSVs)[42]. Activation of the IR by insulin leads to phosphorylation of IRS proteins functioning as a docking station for PI3K, an activator of the Akt pathway. Akt in turn induces translocation of GSVs to the plasma membrane, where GLUT4 is inserted via exocytosis into the plasma membrane. This enables a tenfold higher glucose uptake into muscle cells[43]. In hepatic and muscle cells insulin inhibits generation of glucose from amino and fatty acids (gluconeogenesis) as well as the breakdown of glycogen to glucose (glycogenolysis). In contrast, insulin increases the conversion from glucose to glycogen in hepatic cells (glycogenesis)[44]. Furthermore, insulin influences lipid metabolism by promoting the uptake of FFAs from the blood, inducing the synthesis of fatty acids, triglycerides, and cholesterol (lipogenesis) as well as inhibiting their degradation (lipolysis)[45, 46]. Amino acid uptake, induction of protein synthesis and inhibition of protein breakdown are also facilitated by insulin action in peripheral tissues[47]. Thereby insulin decreases blood nutrient concentrations and promotes anabolic pathways.

The IR is also expressed on beta cells and is required for normal beta cell function as well as beta cell function during chronic hyperglycemia[48]. However, whether this is due to a direct autocrine effect of insulin or to IRS signaling cascades is still under debate, since exact mechanisms of the IR pathway in beta cells are still not fully understood[49].

Constitutive knockout of the IR gene (*Insr)* leads to normal embryonic development and slightly smaller newborns compared to control mice[50]. This indicates that rodents can develop without IR signaling, probably due to compensation of insulin growth factor receptor signaling. However, a few weeks after birth knockout mice show severe metabolic alterations with 1000-fold increased insulin levels and simultaneously elevated blood glucose levels. Since insulin action is eliminated, glucose is not taken up and is not available as an energy source. Lipid breakdown via beta oxidation produces energy; however, accumulation of its end products (ketones) induces diabetic ketoacidosis and subsequent death of *Insr* knockout mice[50].

In conclusion, insulin operates primarily via its IR. In peripheral cells, IR activation leads to induction of several anabolic pathways and inhibition of catabolic pathways. The main purpose of insulin action is to decrease blood glucose levels and maintain glucose homeostasis.

4.1.3 Insulin resistance and type 2 diabetes mellitus

Peripheral insulin resistance is simultaneously a precursor and hallmark of type 2 diabetes mellitus (T2D). It is characterized by an insufficient response of insulin-sensitive cells to insulin[37]. As described previously (see section 4.1.2), under normal conditions, insulin is secreted by beta cells during high blood glucose concentrations into the bloodstream. On peripheral tissues insulin binds to its IR and activates several signaling cascades that in the end lead to a decrease of blood glucose concentrations and maintain glucose homeostasis.

During insulin resistance, the IR becomes less sensitive to insulin concentrations, leading to a higher demand of insulin (relative insulin-deficiency). Beta cells can initially compensate the changed demands by increasing their functional mass and/or their insulin release (hyperinsulinemia)[51-53]. Thereby, beta cells overcome the reduced efficiency of insulin action and maintain glucose homeostasis[54]. Over time, the enhanced insulin secretion by beta cells is not sufficient to overcome insulin resistance leading to a manifestation of hyperglycemia. A decline of functional beta cell mass (due to beta cell apoptosis or dedifferentiation remains controversial[55-57]) intensifies hyperglycemia and paves the way for T2D formation.

The exact underlying mechanisms of insulin resistance are incompletely understood. However, many studies indicate that several metabolic alterations including obesity, glucotoxicity or lipotoxicity play a crucial role in the development of insulin resistance as well as in beta cell function and development of T2D[58].

Obesity describes the enlargement of adipose tissue and is often present during insulin resistance. Adipocytes are the most abundant cell type of the adipose tissue and their main function is the storage of high caloric fatty acids during feeding as well as their breakdown and release during fasting[59]. This equilibrium is disturbed during obesity. Adipocytes promote increased breakdown of triacylglycerols (lipolysis) and increased release of non-esterified fatty acids (NEFAs) into the circulation. Chronic accumulation of NEFAs in the blood induces beta cell dysfunction and apoptosis (a process called lipotoxicity)[60]. Furthermore, the adipose tissue functions as an endocrine organ. Adipocytes secrete hormones and cytokines (adipokines) that play an important role in many biological processes, such as immune response (e.g. adipsin), inflammation (e.g. tumor necrosis factor α), glucose metabolism (e.g. leptin) or insulin sensitivity (e.g. adiponectin)[59]. More than 100 adipokines have been described, and their secretion is dysregulated during obesity and/or insulin resistance. During obesity,

adipokines that impair insulin sensitivity in peripheral tissues (e.g. resistin[61]), as well as pro-inflammatory adipokines that negatively regulate beta cell function (e.g. leptin, TNFα[62]), are increasingly secreted and induce insulin resistance[58].

Furthermore, chronic elevated blood glucose levels (hyperglycemia), as it is often the case during obesity, induce oxidative stress and endoplasmic reticulum (ER) stress in beta cells[58]. Under normal conditions, reactive oxygen species (ROS) are generated during glucose metabolism and are instantly detoxified and proinsulin, an insulin precursor, is folded at the ER and prepared for conversion to insulin. Chronic hyperglycemia leads to an elevated glucose metabolism that in turn results in higher levels of ROS and an increased insulin production. Accumulation of ROS directly damages DNA, proteins and lipids, resulting in oxidative stress[63]. Additionally, the increased insulin synthesis overwhelms the ER, misfolded insulin accumulates and triggers ER stress[64]. Oxidative stress and ER stress ultimately lead to beta cell apoptosis, a process called glucotoxicity, which promotes the development of insulin resistance[65].

Alpha cells, which produce the insulin antagonist glucagon, are also affected by hyperglycemia and increased insulin levels[66]. The imbalance of the bihormonal system induces increased glucagon secretion of alpha cells (hyperglucagonemia), elevated fasting glucagon concentrations and an impaired glucose-induced glucagon suppression. This causes elevated hepatic glucose production, increased blood glucose concentrations, and promotes the formation of diabetes pathophysiology[67].

The formation of insulin resistance (and T2D) is not necessarily linked to obesity and its associated metabolic disturbances. A genome-wide association study (GWAS) found 15 single-nucleotide polymorphisms (SNP) to be associated with insulin resistance and 88 loci that are linked with T2D development (reviewed in Brown & Walker 2016[68]). Most of the genetic variants account for key roles in beta cell function or insulin signaling/resistance. For example, variants of the transcription factor 7-like 2 (*TCF7L2)* gene are strongly linked with the development of T2D as they influence beta cell function and insulin signaling in peripheral tissue cells[69, 70].

In summary, obesity and genetics have an impact on beta cell function as well as on insulin sensitivity of peripheral tissues. Disturbances of the tight balance between insulin and glucagon aid the formation of insulin resistance, hyperinsulinemia and chronic hyperglycemia that ultimately may progress to T2D.

4.1.4 Type 2 diabetes mellitus – Numbers

The term diabetes mellitus originates from the ancient Greek and means “honey sweet flow through”. Ancient cultures discovered that diabetic people have an increased urination and sweet-smelling urine. Diabetes is characterized by chronic elevated blood glucose

concentrations (hyperglycemia)[65]. The causes are an insufficient secretion of insulin from beta cells, no proper insulin response of the periphery tissues or both (see section 4.1.3). Long-term hyperglycemia increases the risk for vascular damages that can proceed into life-threatening diseases like cardiovascular diseases (e.g. hypertension, stroke), eye diseases (e.g. diabetic retinopathy, the leading cause of preventable blindness)[71], nerve damage (diabetic neuropathy) or kidney diseases (diabetic nephropathy). The global expenses to treat diabetes and its complications are estimated to be 760 billion US dollar in 2019[3]. Worldwide 463 million people suffer from diabetes (9.3% of the current world population) and it is anticipated that the quantity will further increase to 700 million people (10.9%) in 2045[3]. The American Diabetes Association categorized diabetes into four main types[72]:

Type 1 diabetes mellitus (T1D) is an autoimmune disorder and the major cause for diabetes during childhood. The abnormal immune response leads to progressive destruction of beta cells, absolute insulin deficiency and persistent hyperglycemia[73, 74].

Type 2 diabetes mellitus (T2D) accounts for around 90% of entire diabetes types and is the leading cause for diabetes in adults[72]. Nevertheless, nowadays T2D occurs frequently in adolescence. The onset of T2D occurs gradually and is nearly impossible to determine exactly. Commonly, T2D starts with an insulin resistance, followed by reduction of functional beta cell mass (whether by beta cell apoptosis or dedifferentiation is still under debate[55-57]). The loss of the first phase insulin secretion is a prominent feature of a developing T2D, and reflects the first beta cell and metabolic disturbances[75]. Insulin resistance and chronic hyperglycemia as well as genetic variants aid the formation of T2D (see section 4.1.3). A recent study identified five different subgroups of T2D, based on specific prevalence for diabetic complications (e.g. non-alcoholic fatty liver disease, diabetic neuropathy)[76]. The new classification allows early and specific treatment for patients as well as possible prevention of diabetic complications.

Gestational diabetes is another type of diabetes categorized by the American Diabetes Association, and is a pregnancy complication that occurs in around 16.5% of all pregnancies worldwide[77]. Expectant mothers develop chronic hyperglycemia that is largely caused by insulin resistance.

The fourth diabetes type includes a variety of diabetes forms, such as the monogenetic disorder maturity onset diabetes of the young (MODY) or diseases of the exocrine pancreas (e.g. pancreatitis). Combined, the third and fourth type account for approximately 1-2% of all diabetes cases[72].

The treatment of diabetes aims to keep the individual blood glucose concentrations in a narrow physiological range in order to suppress the progress and the long-term complications of diabetes[78]. Since the causes of the four types of diabetes are different, also the treatments have different strategies to achieve this aim. T1D is characterized by loss of

functional beta cell mass and insulin deficiency[73, 74]. Therefore, the treatment of choice is continuous blood glucose measurements coupled with exogenous administration (via injections or pumps) of insulin[74]. Because of the progressive development of T2D the first treatments contain lifestyle interventions like exercise and weight loss to manage weight and to improve blood glucose levels. When T2D progresses, there is a wide range of medications that target different mechanisms of the glucose metabolism[79]. Some medicaments impair hepatic glucose production and increase insulin sensitivity (biguanides), others increase the insulin secretion of beta cells (sulfonylureas) or increase the urinary glucose excretion (sodium-glucose co-transporter 2 inhibitors)[80]. The transplantation of pancreatic islets or the induction of beta cell proliferation to increase the functional beta cell mass and insulin output are approaches that might remedy diabetes one day[74]. However, to present there is no cure for diabetes, and patients have to be medically supervised for their entire life to prevent diabetes progression and its life-threatening complications[79].

In sum, diabetes is a multifactorial disease and its prevalence is increasing worldwide. Diabetes is classified into four main types of diabetes and until today, there is no cure for any type of diabetes.

4.2 The vascular network in the pancreas

The pancreas is a glandular organ supplied by the celiac as well as the superior mesenteric artery that both branch from the abdominal aorta[9]. The celiac artery branches further into the splenic artery and supplies the tail of the pancreas. The head in turn is supplied by the hepatic and gastroduodenal artery that derive from the mesenteric artery[9]. Arteries branch into numerous arterioles, which further divide into capillaries. Here, the exchange of gas, nutrients, hormone and waste products between the pancreatic cells and circulatory system is taking place.

4.2.1 The vascular system of the islet of Langerhans

Small pancreatic islets (<100 µm) are incorporated into the exocrine vasculature[81]. Bigger islets (>100 µm) are supplied by one to five arterioles that enter the islet and branch into capillaries, forming a dense glomerular-like vascular network[82, 83]. The capillaries exit the islet as venules, and drain the blood either into veins that surround the islet like a basket or directly into veins of the exocrine tissue[84]. In the end, pancreatic veins empty into the portal vein and carry hormones and waste products to the liver[85].

To ensure glucose homeostasis, pancreatic islets permanently sense blood glucose concentrations and continuously secrete hormones into the circulatory system. Almost every beta cell is in contact with an islet endothelial cell (EC)[86, 87]. Moreover, a dense network of blood capillaries with a vessel density five times higher, a vessel diameter 20-30% wider and

vessels with ten times more fenestrae compared to the capillaries of the exocrine tissue pervade the pancreatic islets[83, 88]. Even though islets comprise for only 1-2% of the total pancreas volume, its capillaries deliver 10-20% of the total pancreatic blood flow to the endocrine cells.[84, 89, 90].

The blood vessels of pancreatic islets consist of two cell types. A thin, single layer of ECs forms the inner capillary tube. These ECs are highly fenestrated in order to facilitate the rapid exchange of nutrients as well as hormones between the blood circulatory system and the endocrine cells[91-93]. Moreover, ECs secrete a vascular basement membrane, a specialized extracellular matrix (ECM). The ECM is built up by a dense network of fibrous proteins that surrounds the islet capillaries and provides several cues for beta cell function (for detailed information see section 4.2.3)[94]. *In vivo and in vitro* studies revealed that islet ECs provide signals (e.g. hepatic growth factor) that are important for beta cell proliferation and function[95, 96].

The second cell type of islet capillaries are pericytes. Pericytes, the mural cells of microvessels, are wrapped around the endothelial tube and are embedded into the vascular basement membrane of ECs. With their long cytoplasmic processes pericytes contact several ECs and cover around 40% of the islet capillaries[97]. In pancreatic islets, pericytes support vessel stability, morphology and function[98-100], and also regulate blood flow by fine-tuning capillary diameter[97]. Furthermore, *in vivo and in vitro* studies displayed key functions of pericytes for beta cell proliferation[101]. Lack of pericytes in pancreatic islets leads to a downregulation of beta cell transcription factors (*Mafa*, *Ins1*, *Ins2* and *Pdx1*), causing an impaired glucose tolerance and a reduced insulin content of beta cells[102].

Several studies identified vascular endothelial growth factor A (VEGF-A) and its receptor 2 (VEGFR2) as key regulators for islet vascularization[92, 103, 104]. Endocrine cells secrete VEGF-A during development. VEGFR2 is expressed in ECs, and binding of VEGF-A induces EC proliferation[105]. ECs form new blood vessels that sprout from the pre-existing vasculature and migrate along a VEGF-A gradient towards the VEGF-A producing endocrine cells - a process termed angiogenesis[105]. Newly formed blood vessels in turn provide cues that lead to differentiation of insulin-producing beta cells and islet formation[103]. Adult islets still show a high expression of VEGF-A, since it is important for the maintenance of the islet vasculature and endothelial fenestration[106]. Besides pro-angiogenic factors (like VEGF-A), also anti-angiogenic factors are present in the islet. The angiostatic factor thrombospondin-1 is also secreted by endocrine islet cells and restricts vascular density by blocking angiogenesis and selectively inducing apoptosis in activated ECs[107, 108]. The tight balance between pro- and antiangiogenic factors regulates an optimal islet vascularization.

The vasculature of pancreatic islets is necessary to keep glucose levels in a narrow, controlled range[91, 92]. In rodents, the absence of the intra-islet vasculature allows islet growth,

but results in a delayed insulin secretion plus an impaired glucose tolerance[92]. These findings emphasize the important role of the islet microvasculature for fine-tuning blood glucose regulation.

In summary, endothelial cells and pericytes build the capillaries of the pancreatic islet. Blood vessels create a microenvironment where beta cells can differentiate, proliferate and function properly, and thus maintain glucose homeostasis. In turn, beta cells provide cues that enable islet vascularization.

4.2.2 Islet vascular system during chronic hyperglycemia

During insulin resistance, beta cells compensate the decreased insulin sensitivity of the peripheral tissues with an increased secretion of insulin and an expansion of beta cell mass (reviewed in detail in section 4.1.3)[51, 52]. These compensatory changes of beta cells are necessary to maintain normoglycemia. The extensive capillary network of pancreatic islets plays a crucial role for beta cell function and insulin secretion[91, 93, 94]. To meet the increased metabolism and mass of beta cells, the vascular system of pancreatic islets experiences adaptive changes. The absolute vessel area of pancreatic islets, the islet capillary blood flow as well as the blood pressure increase during chronic hyperglycemia[84, 109]. The vascular changes are not mediated by EC proliferation, but exclusively by dilation of preexisting vessels[110]. This provides a bigger beta cell to EC surface area, supporting the increased blood flow as well as accommodating the enhanced demand for insulin delivery to the peripheral tissues. Besides the increased vessel diameter, ultrastructural changes of islet capillaries occur during hyperglycemia. While EC fenestration and proliferation are unchanged, the ECM surrounding the capillaries doubles in width, which possibly is a direct response of islet ECs to the increased blood flow and shear stress[110]. Furthermore, a recent study reports pericyte loss of the islet vasculature of obese mice and humans with T2D[97]. Hyperglycemia and increased beta cell action lead to pericyte relaxation and subsequent pericyte loss. Other studies report pericyte hypertrophy after induced insulin resistance[110, 111]. This may be a compensation to the increased islet blood pressure, since these pericytes display an increased alpha smooth muscle actin expression that usually is expressed by vascular smooth muscle cells. Irregularities of the pericyte EC communication as well as increased islet blood pressure can trigger vascular leakage (hemorrhages) as it is observed in the islets of obese mice[110, 112]. The extravasation of red blood cells into the islet parenchyma causes nutrient deficiency for the challenged beta cells as well as islet dysfunction[113]. Consequently, activated ECs recruit monocytes that infiltrate the islet and secrete pro-inflammatory cytokines (e.g. interleukin-6), which promote beta cell apoptosis[114].

During chronic hyperglycemia (e.g. insulin resistance or T2D), beta cells and their supplying blood vessels initially adapt to satisfy the increased demands for insulin. However,

an abnormal vascular bed, increased blood flow, dilation of vessels, ultrastructural changes of the ECM and disturbances of the pericyte EC interaction result in islet hemorrhages and beta cell apoptosis that contribute to the progression of T2D.

4.2.3 Extracellular matrix (ECM)

The vascular basement membrane is a specialized ECM, a three-dimensional, non-cellular network that is present in all mammalian tissues[115]. It forms a physical scaffold made of glycosaminoglycans (GAGs) and different fibrous and non-fibrous proteins that give structural and biological support to adjacent cells[115, 116]. The main components of the ECM are collagens, laminins and fibronectins. Several studies have shown that the ECM plays an important role in cellular processes like cell-cell communication, cell proliferation or cell adhesion (reviewed in Rozario & DeSimone 2010[117]). Each tissue shows a unique composition of ECM proteins, indicating a specific role of the ECM for the adjacent cells. Endothelial cells exclusively produce an extensive ECM network in pancreatic islets that surrounds the islet capillaries[118, 119]. Furthermore, a capsule made up of ECM proteins and fibroblasts surrounds each islet, separating the endocrine cells from the exocrine tissue[120]. The major ECM component of pancreatic islets is collagen. Collagens consist of three α-chains that coil to a helix and either assemble into fibrils (e.g. collagen I) or form a network (e.g. collagen IV)[115, 119]. Beta cell differentiation and insulin secretion are positively influenced by collagen IV[11, 121]. Another highly abundant islet ECM molecule is fibronectin: a protein dimer that is build up by two same-sized subunits that are connected via disulfide bonds[122]. Although deriving from a single gene, there are several soluble and insoluble fibronectin isoforms (due to alternative splicing) in pancreatic islets. *In vitro* and *in vivo* studies show an increased insulin secretion when beta cells are in contact with fibronectin[95, 123]. The third major component of the ECM are Laminins, heterotrimeric glycoproteins that are composed of an α-, β- and γ-chain. There are several chain isoforms resulting in sixteen different laminin isoforms found *in vivo*[124]. Islets contain several laminin isoforms, but the most prominent are laminin-411 (α-4, β-1,γ-1) and laminin-511 (α-5, β-1,γ-1). These isoforms enhance beta cell proliferation as well as insulin expression[120, 125].

In summary, the ECM in pancreatic islets is produced by endothelial cells and gives support as well as structure to the endocrine cells.[91]. The ECM provides a niche for beta cells that promotes beta cell differentiation, proliferation and function[95, 126].

4.2.4 Beta cell – endothelial cell communication: The Integrin – ECM connection

As described above, the islet ECM strongly influences beta cell function (see section 4.2.3). Since beta cells are unable to synthesize an ECM, they have to bind to the ECM that surrounds

the islet capillaries[95]. Around 15% of the beta cell surface area is in contact with the ECM and the main receptor for beta cell to ECM adhesion are the integrin receptors[86, 127].

Integrins are heterodimeric transmembrane cell surface receptors that are composed of an α- and a β-subunit[128]. They facilitate the adhesion between the actin cytoskeleton of the cell and its extracellular environment. Despite lack of an intracellular kinase activity, integrins mediate `outside-in` as well as `inside-out` signaling upon binding to an ECM component via the recruitment of intracellular adaptor proteins[128]. Several cellular processes, including cell survival, migration and proliferation are regulated by adhesion of distinct integrin isoforms (reviewed in Hynes 2007[128]).

β1 integrin is the most abundant integrin isoform in beta cells and forms heterodimers with different α subunits[129]. For example, α1β1 integrin binds to collagen IV and induces beta cell proliferation, whereas α5β1 integrin enables adhesion to fibronectin and enhances insulin secretion[95, 121]. Beta cell-specific knockout of β1 integrin gene (*Itgb1*) gene leads to a dramatically reduced beta cell number (-80%), stressing the importance of β1 integrin for beta cell expansion[127]. Composition of different integrin subunits and their binding to distinct ECM molecules enables activation of various signaling pathways that regulate key mechanisms of beta cell function[121, 130, 131]. Clusters of integrins, named focal adhesions, serve as mechanical link between the ECM and the cytoskeleton of the cell. Several adaptor proteins are recruited to the cytoplasmic tails of integrins to stabilize the complex and serve as signaling hub[132].

Besides endothelial cells, beta cells are in touch with other endocrine/ beta cells[86]. They adhere via different cell adhesion molecules (CAMs), e.g. gap junctions, adherens junctions or tight junctions. Noteworthy, there is neither an extracellular matrix nor β1 integrin activation between endocrine cells[133].

To sum up, integrin binding to ECM ligands activates a broad range of cellular signaling pathways. Since endothelial cells exclusively synthesize the ECM in pancreatic islets, beta cells have to adhere to their ECM to activate integrin signaling. This interaction is crucial for normal beta cell function.

4.2.5 Integrin-linked kinase and the IPP complex

Integrin signaling is crucial for various cellular processes (see section 4.2.4). To transduce signals, integrins have to recruit intracellular adaptor proteins, since they lack intrinsic enzymatic or kinase activity[134]. Binding of β1 integrin to ECM ligands induces β1 integrin activation and formation of focal adhesions. Integrins recruit several adaptor proteins to their cytoplasmic tails, which assemble to multiprotein complexes, and forward signals[132]. One of the key β1 integrin adaptor proteins is the integrin-linked kinase (ILK).

ILK is an ubiquitously expressed, 59-kDA, highly conserved protein that is present in worms, flies, rodents and humans[132]. More than 20 years ago Hannigan et al. identified ILK in

a yeast two-hybrid system as a new interaction partner of the cytoplasmic domain of β1 integrin[135]. ILK consists of three domains: four ankyrin repeats at the N-terminus, followed by a pleckstrin homology (PH)-like domain and a C-terminal kinase-like domain, which can bind to β1 and β3 integrins[132, 135]. ILK is a central downstream protein of integrin signaling and crucial for integrin signaling *in vivo*[136]. The importance of ILK is demonstrated by the fact that a global *Ilk* knockout, similar to a global *Itgb1* knockout, leads to embryonic death during peri-implantation state, because *Ilk*-deficient embryos fail actin organization, cell adhesion and epiblast polarization[137-139]. Initially, ILK was identified as a serine / threonine kinase due to sequence homology[135]. Today, several studies disproved the catalytic activity and classify ILK as a pseudokinase. Genetic studies in *drosophila melanogaster*[140], *Caenorhabditis elegans*[141] and mice[137, 142] demonstrated that the kinase ability of ILK is not necessary for survival. The analysis of the crystal protein structure further supports the opinion that ILK has no catalytic activity, since the catalytic core lacks necessary motifs and the ATP γ-phosphate is geometrically too far away from the catalytic loop[143]. However, ILK is important for many cellular processes and regulates actin organization, cell polarization, spreading, migration and proliferation (reviewed in Legate et al. 2006[132]).

ILK is the central component of the trimeric ILK/PINCH/Parvin (IPP) complex and ensures stability of this signaling hub. PINCH (Particularly interesting new cysteine-histidine-rich protein) has two isoforms, PINCH1 and PINCH2. Both bind to the N-terminal ankyrin repeats of ILK and are important for integrin-mediated cell adhesion and cell spreading[144, 145]. Interestingly, knockout of PINCH1 also leads to embryonical death during peri-implantation state[146, 147]. In contrast, PINCH2 knockout mice are viable, fertile and have no explicit phenotype. However, these mice show an increased PINCH1 expression, suggesting a compensation through PINCH1[148]. Parvin is the third component of the IPP complex, and binds to the kinase-like domain at the C-terminus of ILK[143, 149]. Parvin features three isoforms: α-parvin, also called actopaxin or CH-ILKBP, β-parvin or affixin, and γ-parvin. These isoforms are encoded by the *Parva, Parvb* or *Parvg* genes respectively, and recruit actin-binding proteins. α-parvin recruits α-actinin, β-parvin vinculin, and γ-parvin proteins that regulate actin polymerization[150]. Global knockout of *Parva* leads to embryonic lethality at E10.5, similar to *Ilk* knockout mice[151].

Within the heterotrimeric IPP complex, ILK is simultaneously assembled with one PINCH isoform and one parvin isoform. This causes several IPP complex compositions, which process different signal transductions[145, 151]. The IPP complex recruits additional proteins that regulate several pathways (e.g. Akt pathway or RTK pathway) downstream of integrin signaling, and play a critical role for cell adhesion, spreading, migration and survival[132].

Tissue-specific knockout of *Ilk* causes different phenotyoes. *Ilk* knockout in vascular smooth muscle cells and pericytes leads to vascular malformations and death after embryonic

stage E18.5[152]. Intestinal epithelial *Ilk*-deficient mice show reduced cell proliferation[153]. These findings underline that ILK, like β1 integrin, has tissue-specific properties and influences several signaling pathways that regulate various cellular processes (like proliferation, differentiation or migration).

In summary, ILK is a key downstream adaptor protein of β1 integrin. ILK forms multiprotein complexes (preferably with PINCH and parvin) at the cytoplasmic tail of β1 integrin. The IPP complex links integrin to the cytoskeleton and initiates several signaling pathways that are important for cell function.

4.3 Aims of this study

The β1 integrin signaling pathway has been studied thoroughly in previous years. Several *in vitro* and *in vivo* studies nicely showed that β1 integrin influences beta cell proliferation, differentiation and function. Surprisingly, little is known about ILK, one of the main cytosolic interaction partners of β1 integrin in the islet of Langerhans. Therefore, the major aim of this thesis was to elucidate the role of ILK for islet function.

First, *Ilk* was specifically deleted in the pancreatic epithelium of mice in order to characterize its role in islet function. We analyzed glucose tolerance and insulin secretion of *Ilk* knockout mice and of isolated pancreatic islets. Differences in the *in vivo* and *in vitro* insulin secretion encouraged us to analyze the islet vasculature, because the islet vascularization plays a critical role in insulin secretion. We classified islet ECs in intra- and periphery-islet ECs and determined the onset of a striking vascular phenotype. Next, we analyzed beta cell proliferation, apoptosis, VEGF-A secretion and adhesion between isolated islets and basement membrane components. Furthermore, we used an atomic force microscope (AFM) to perform single-cell force spectroscopy (SCFS) and measured the adhesion strength between beta cells and ECs as well as cortex tension of *Ilk* knockout islet cells. To get an idea of the underlying mechanisms of ILK and its role in pancreatic islet vascularization, we used inhibitors that influence actomyosin contraction. Finally, we could show that the biomechanical properties of pancreatic epithelial cells determine the localization of its vasculature.

In a follow-up project we continued our work on the basis of our newly obtained findings. The dense vascular network of pancreatic islets is crucial for maintaining glucose homeostasis and beta cell function. During a beginning diabetes, which is characterized by elevated blood glucose levels (hyperglycemia), beta cells can compensate the increased metabolic demands by increasing their insulin release and/or their functional beta cell mass. Moreover, the islet vasculature also adapts in order to support the challenged beta cells. Here, we aimed to determine the role of ILK in beta cells as well as the role of the intra-islet vasculature for beta cell function during insulin resistance.

We generated beta cell-specific *Ilk* knockout mice and administered the insulin receptor antagonist S961 to these mice. To verify that S961 induced insulin resistance, we measured random blood plasma glucose and insulin levels. Subsequently, we analyzed if *Ilk*-deficient beta cells and/or insulin resistance resulted in changes of the islet vasculature. Next, we investigated how an *Ilk* knockout and the intra-islet vasculature affect beta cell function during insulin resistance. Therefore, we determined glucose tolerance as well as insulin secretion of *Ilk*-deficient mice and isolated pancreatic islets. To determine the role of ILK for beta cell proliferation during insulin resistance, we injected mice with EdU, a thymidine analog that incorporates into the DNA of dividing cells. Finally, we quantified beta cell proliferation, apoptosis and islet size of *Ilk* knockout mice. With the obtained results, we underline the relevance of ILK as well as the intra-islet vasculature for beta cell proliferation and insulin secretion during insulin resistance.

In a second project, we aimed to develop an *in vitro* assay that allows the analysis of sprouting angiogenesis and pericyte coverage. Today, there are several *in vitro* and *ex vivo* assays that can nicely mimic angiogenesis. Strikingly, no assay offers the formation of vascular, lumenized tubes built up by human ECs and human pericytes in a defined setup.

We extended a previously reported bead sprouting assay by including pericytes to EC-derived sprouts. Pericytes surround capillaries and fulfill crucial functions that ensure vascular homeostasis. Furthermore, we transferred the setup into a multi-well format to compare multiple treatments simultaneously under reproducible conditions. Next, we established an immunostaining protocol to distinguish between ECs and pericytes within the angiogenic sprouts. For consistent analysis of sprout morphology and pericytes coverage, an ImageJ plugin was developed that allows a standardized, automated as well as quantitative analysis of both. Finally, we tested more than 40 compounds for their biological effects on sprouting angiogenesis and pericyte coverage.

With this thesis, we significantly contribute to the knowledge of the role of ILK in islet cells during standard and insulin resistance conditions. Our findings show that the biomechanical properties of an epithelial tissue determine the location of its vasculature. In addition, we provide a robust *in vitro* angiogenesis assay plus an accompanying ImageJ plugin for analysis of sprout morphology and pericytes coverage.

5 Results

5.1 Quantitative assessment of angiogenesis and pericyte coverage in human cell-derived vascular sprouts

This paragraph contains the original research article “Quantitative assessment of angiogenesis and pericyte coverage in human cell-derived vascular sprouts” (Eglinger et al.[1]). The article presents a Fiji Plug-in that enables an easy and timesaving analysis of *in vitro* grown vascular sprouts that are build up from endothelial cells and pericytes.

5.1.1 Background

Sprouting angiogenesis, the formation of new capillary branches from pre-existing blood vessels or lymphatic vessels, is required to build functional vascular networks, and altered sprouting angiogenesis is involved in many diseases[154]. Sprouting is induced by activation of endothelial cells (ECs) via growth factors such as vascular endothelial growth factor (VEGF), platelet-derived growth factor (PDGF), placental growth factor (PlGF), and hypoxia-inducible factor (HIF)-1α[155]. Activated ECs proliferate, extend into the surrounding tissue[156], and recruit pericytes to attach to the outer wall of the newly formed vessels[157]. The presence of pericytes on mature capillaries is required for stabilization of the endothelium and for regulation of blood flow, as observed in the blood–brain barrier[158, 159]. Pericytes are in close contact with ECs, as they extend long cytoplasmic processes across several ECs to encircle the EC-derived vascular tubes. Moreover, they share a basement membrane and physically interact via numerous contacts such as for example peg-socket junctions, adhesion plaques, or gap junctions[160]. Dysfunctional interplay between pericytes and the endothelium is frequently the cause or consequence of many diseases[98, 161, 162], resulting in increased vascular permeability and defective vessel maturation, which promote vessel leakage and inflammation[163]. Cancer cells, for instance, can induce detachment of pericytes from quiescent vasculature, thereby activating ECs to sprout into the surrounding tissue[164]. Pericyte detachment is also one of the first pathological hallmarks during diabetic retinopathy. The disease begins with a thickening of the vascular basement membrane, followed by a loss of pericytes and an increase in vascular permeability[165]. Ultimately, neovascularization causes hemorrhaging and vision loss[166]. On the contrary, after stroke, pericytes constrict around capillaries to decrease blood flow. When these pericytes die, the blood–brain barrier is disrupted, leading to progressive neuronal damage[167].

It is hypothesized that pericytes also play a regulatory role during angiogenesis[163, 168]. Our aim was to develop a method to assess pericyte coverage during sprouting angiogenesis in a defined human cellular system. We modified a sprouting assay that involves ECs and was

previously used in a number of recent publications[169-171]. Nakatsu et al. described an optimized angiogenesis assay that leads to vascular sprouts with a defined lumen. This assay uses fibrin as an extracellular matrix and is characterized by the formation of vascular sprouts that harbor patent multi-cellular lumens and a basement membrane[94]. The sprouts undergo many critical steps that occur *in vivo* during angiogenesis. In order to mimic the *in vivo* vasculature as accurately as possible, we have modified their protocol to include human vascular pericytes[160]. After co-culturing ECs and pericytes, we verified that sprouts have lumens and that pericytes attach to the outer wall of vascular sprouts. Further, we adapted the original method for use in multi-well plates in order to simultaneously test and compare multiple treatments under reproducible conditions. Finally, for consistent analysis of sprout morphology and pericyte coverage, we developed an ImageJ plugin that measures sprout number, length and width, as well as cell density and pericyte coverage of vascular sprouts. While similar tools were published for standardized quantification of other angiogenesis assays, such as “Angiotool” for the quantification of retinal vascular networks[172], or “Aqual” for the aortic ring assay[173], no such standardized tool was previously available for the bead sprouting assay. Using our optimized analysis workflow, we tested more than 40 compounds for their biological effects on sprout morphology and pericyte coverage.

Here, we describe a standardized procedure of the bead sprouting assay using human umbilical vein ECs (HUVECs) and human brain vascular pericytes (HBVPs). To ensure comparability between experimental repetitions as well as between different researchers performing the experiments, we developed, using the plugin tool described below, a standardized automated quantitative analysis of developing angiogenic sprouts covered with pericytes.

5.1.2 Results

5.1.2.1 Lumen formation and pericyte coverage in multi-cellular sprouts

To assess vascular lumen formation within endothelial cell (EC)-derived vascular sprouts with and without pericytes, we seeded HUVEC in the presence or absence of HBVP onto microcarrier beads that subsequently were embedded into fibrin gels. In Figure 3, a summary of the experimental design is shown, which can be performed in either 96-well plates to screen compounds (Figure 3a, left side) or in glass-bottom dishes for staining with various different antibodies (Figure 3a, right side). A timeline of the assay and the structure of a typical vascular sprout derived from human ECs and pericytes is also shown (Figure 3b, c).

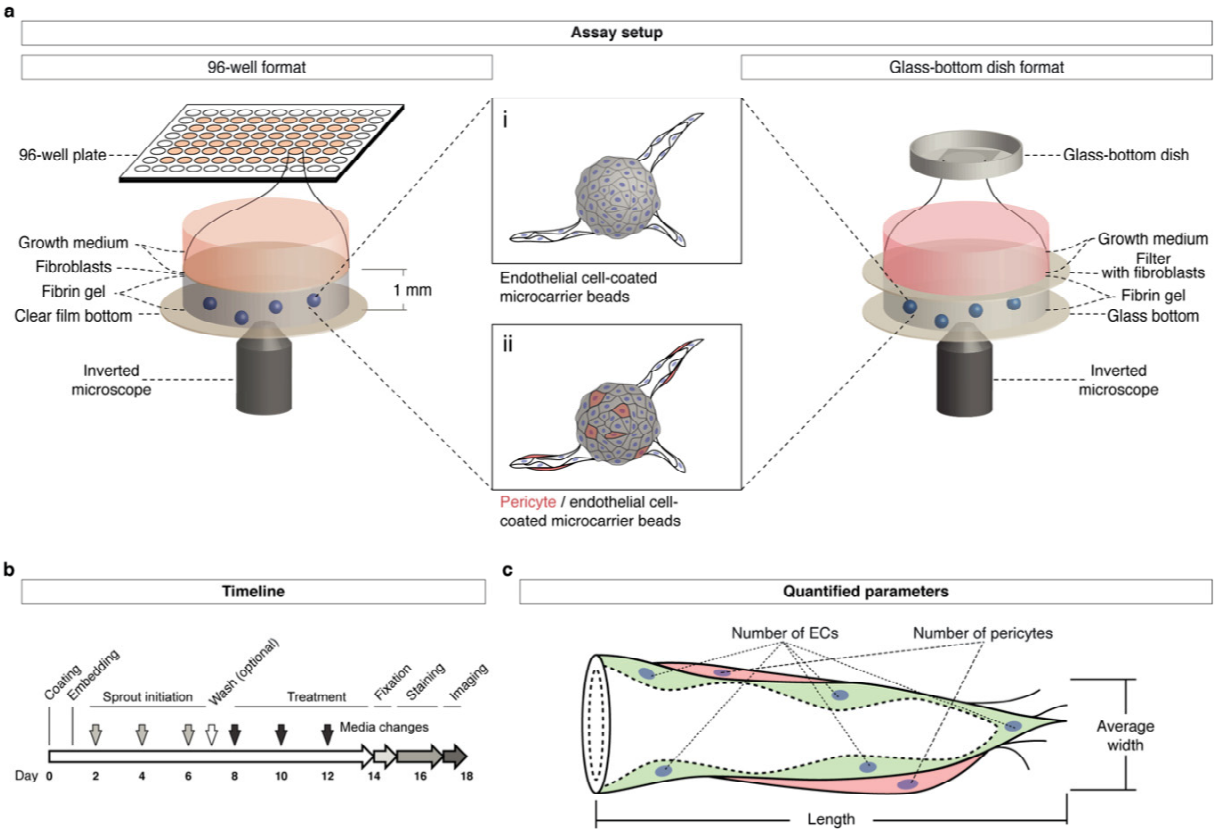

Figure 3: ***Setup and workflow of the EC/pericyte sprouting assay***. (**a**) Schematic drawing of the assay setup: A 1:10 co-culture of pericytes (red) and endothelial cells are coated on microcarrier beads (center) that are then embedded into fibrin gels in each of the inner 60 wells of a 96-well plate (left). Alternatively, cell-coated beads are embedded into fibrin gels in a glass-bottom culture dish (right). The fibrin gels are subsequently covered with a layer of fibroblast cells (left), which can also be placed onto filters (right) to facilitate removal and subsequent staining. Developing sprouts are cultured in growth medium containing the desired treatment, and they can be imaged using an inverted microscope. (**b**) Timeline of the assay procedure: after coating ECs or ECs/pericytes on microcarrier beads and embedding them in fibrin gels, sprouts are grown for up to 6 days, optionally supplied with 10 µM vanadate to accelerate sprout growth; after removal of vanadate by washing with growth medium, treatment with test compounds or growth factors can be pursued for another 6 days; for image analysis, sprouts are fixed, stained, and imaged using an inverted microscope. (**c**) Schematic representation of a sprout containing ECs (green) and pericytes (red), indicating the quantified sprout parameters.

After an incubation of either 2 (with pericytes) or 4 days (without pericytes), the first sprouts formed a patent vascular lumen detectable by bright field transmission light microscopy (Figure 4a). After fixation and staining of the F-actin cytoskeleton by fluorescently labeled phalloidin, a lumen was also detected in optical cross-sections of confocal z-stacks (Figure 4b). Vascular sprouts were composed of multiple cells connected through VE-cadherin positive junctions and surrounded by a vascular basement membrane containing laminin (Figure 4c). Pericytes aligned to the abluminal side of the vascular sprouts (Figure 4d, e).

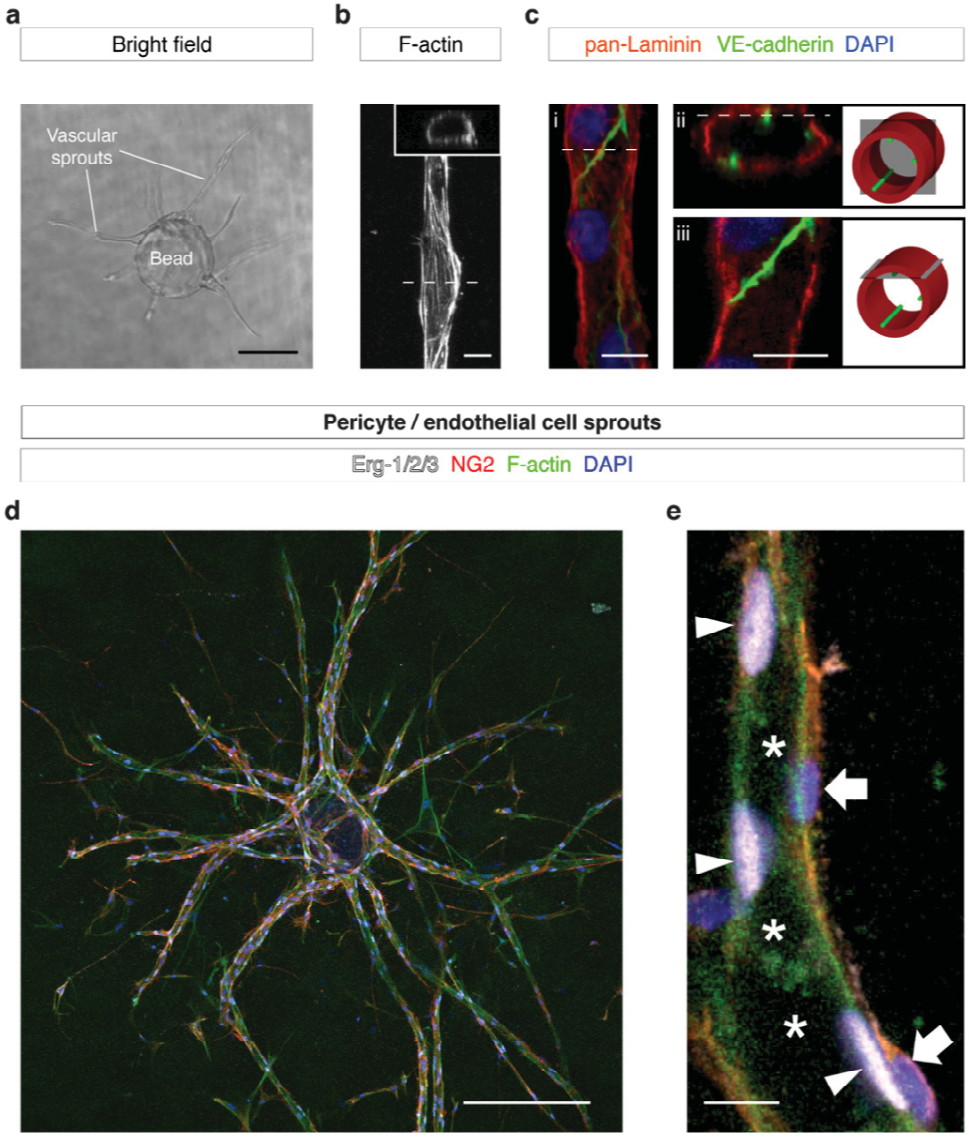

Figure 4: ***Validation of sprout morphology.*** (**a**) Bright field image of vascular sprouts growing out from an EC-coated bead. (**b**) Confocal micrograph of a vascular sprout stained for F-actin; a patent lumen is seen on an optical cross-section (inset). (**c**) Confocal micrographs of a vascular sprout stained for laminin (red), VE-cadherin (green), and nuclei (DAPI, blue); maximum intensity projection (i), optical cross-section (ii), and optical longitudinal section (iii); 3D configuration of the optical sections is depicted in simplified illustrations (right). (**d**, **e**) Confocal micrographs of human pericyte/EC-derived vascular sprouts stained for endothelial nuclei (Erg-1/2/3, white), pericytes (NG2, red), F-actin (phalloidin, green), and nuclei (DAPI, blue); maximum intensity projection showing a bead with connected sprouts (**d**), optical longitudinal section of a single sprout (**e**), showing the vascular lumen (asterisks), EC nuclei (arrowheads), and pericyte nuclei (block arrows). Scale bars, 200 µm (**a**); 10 µm (**b**, **c**); 200 µm (**d**); 10 µm (**e**).

5.1.2.2 Quantitative measurement of sprout morphology and pericyte coverage

We developed a plugin for ImageJ to measure parameters of sprout morphology (Figure 5). For image analysis with our plugin, maximum intensity projections (MIPs) of sprout images were created. The adjustment of analysis parameters was performed on a selected subset of images representative of the variability within the whole dataset. We adjusted the measurement parameters for each of the analysis steps (Figure 5a-c), including the number of beads (Figure 5d-f), number of vascular sprouts (Figure 5g-i), total number of nuclei (Figure 5j-l), and area covered with pericytes (Figure 5m-p). The MIPs of whole well images from 96-well plates or single beads in glass-bottom dishes were analyzed using the ImageJ plugin we developed.

An example of the produced image-based quantitation is shown in Figure 6. Starting with the original input image (Figure 6a), our plugin detects the bead (Figure 6b) and the sprouts connected to it (Figure 6c). The intensity of immunostaining against NG2, a pericyte marker, is used to segment pericyte area in the image (Figure 6d). The presence or absence of Erg-1/2/3 staining is used to classify DAPI-positive cell nuclei into EC and pericyte-derived nuclei (Figure 6e-g). For length measurements, the morphological skeleton of the sprouts is generated (Figure 6h). The segmentation results are then used to measure morphological parameters of vascular sprouts, such as sprout number, length and width, as well as cell density, the ratio between ECs and pericytes, and the area of pericyte coverage (Figure 6m).

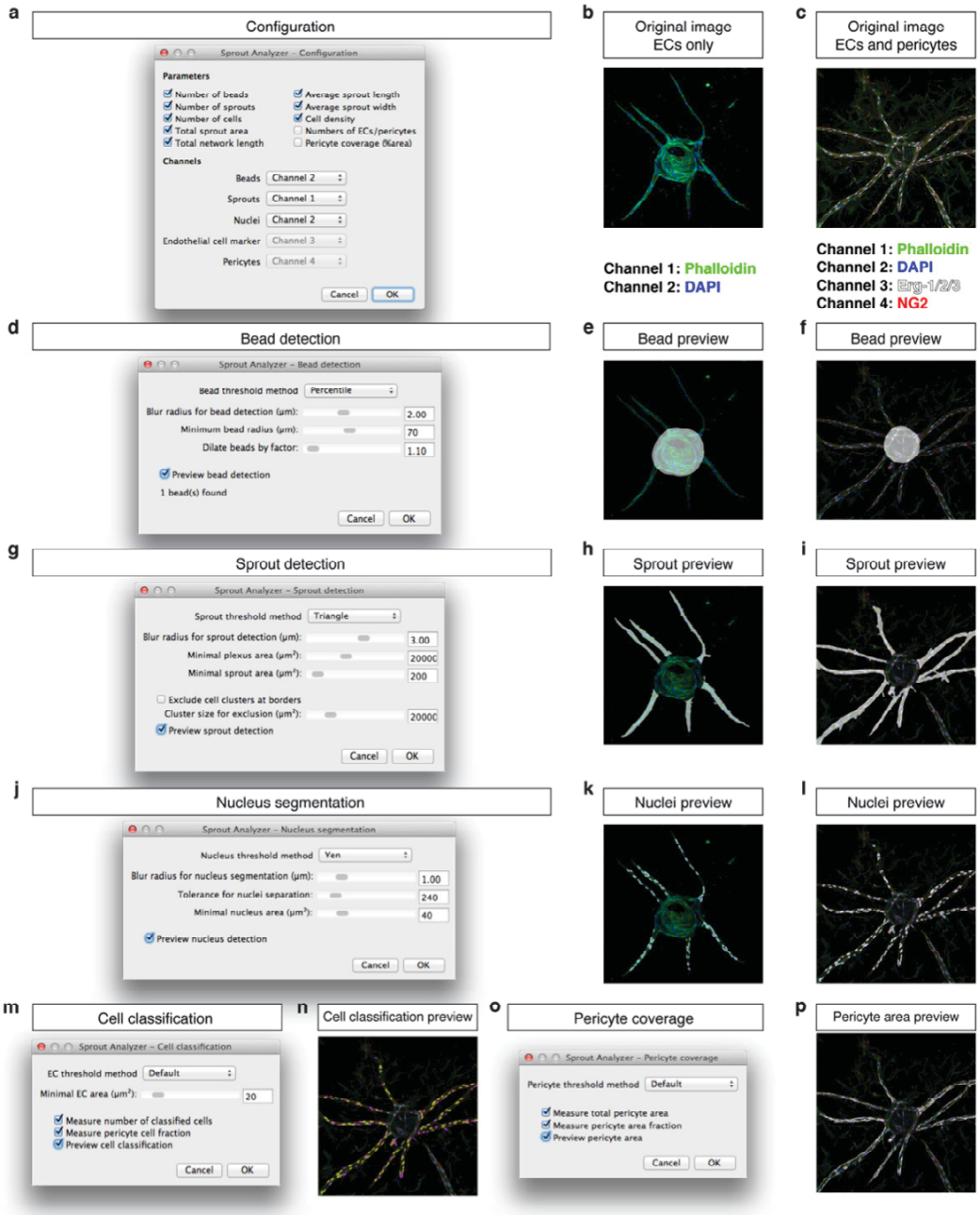

Figure 5: ***Configuration of the Sprout Analyzer plugin.*** (**a**) Dialog to configure output measurement parameters and to define input configuration, i.e., which image channel contains which staining information. (**b**) Example image showing a microcarrier bead with vascular sprouts stained for F-actin using phalloidin-AF488 (green) and nuclei using DAPI (blue). (**c**) Example image with EC/pericyte-derived sprouts stained for F-actin using phalloidin-AF488 (green), nuclei using DAPI (blue), EC nuclei using an anti-Erg-1/2/3 antibody (white), and pericytes using an anti-NG2 antibody (red). (**d**) Dialog to configure bead detection; when the preview checkbox is activated, a bead mask image (white) is overlaid onto the image (**e** and **f** for the original images in **b** and **c**, respectively). (**g**) Dialog to configure sprout detection; when the preview checkbox is activated, a sprout mask image (white) is overlaid onto the image (**h**, **i**). (**j**) Dialog to configure nucleus detection; when the preview checkbox is activated, a nucleus mask image (white) is overlaid onto the image (**k**, **l**). (**m**) Dialog to configure cell classification; when the preview checkbox is activated, a preview showing ECs (yellow) and pericytes (magenta) is overlaid onto the image (**n**). (**o**) Dialog to configure pericyte coverage measurement; when the preview checkbox is activated, a pericyte area mask image (white) is overlaid onto the image (**p**). For detailed instructions, see protocol in Additional file 3, Additional file 1: Video S1, and Additional file 2: Video S2.

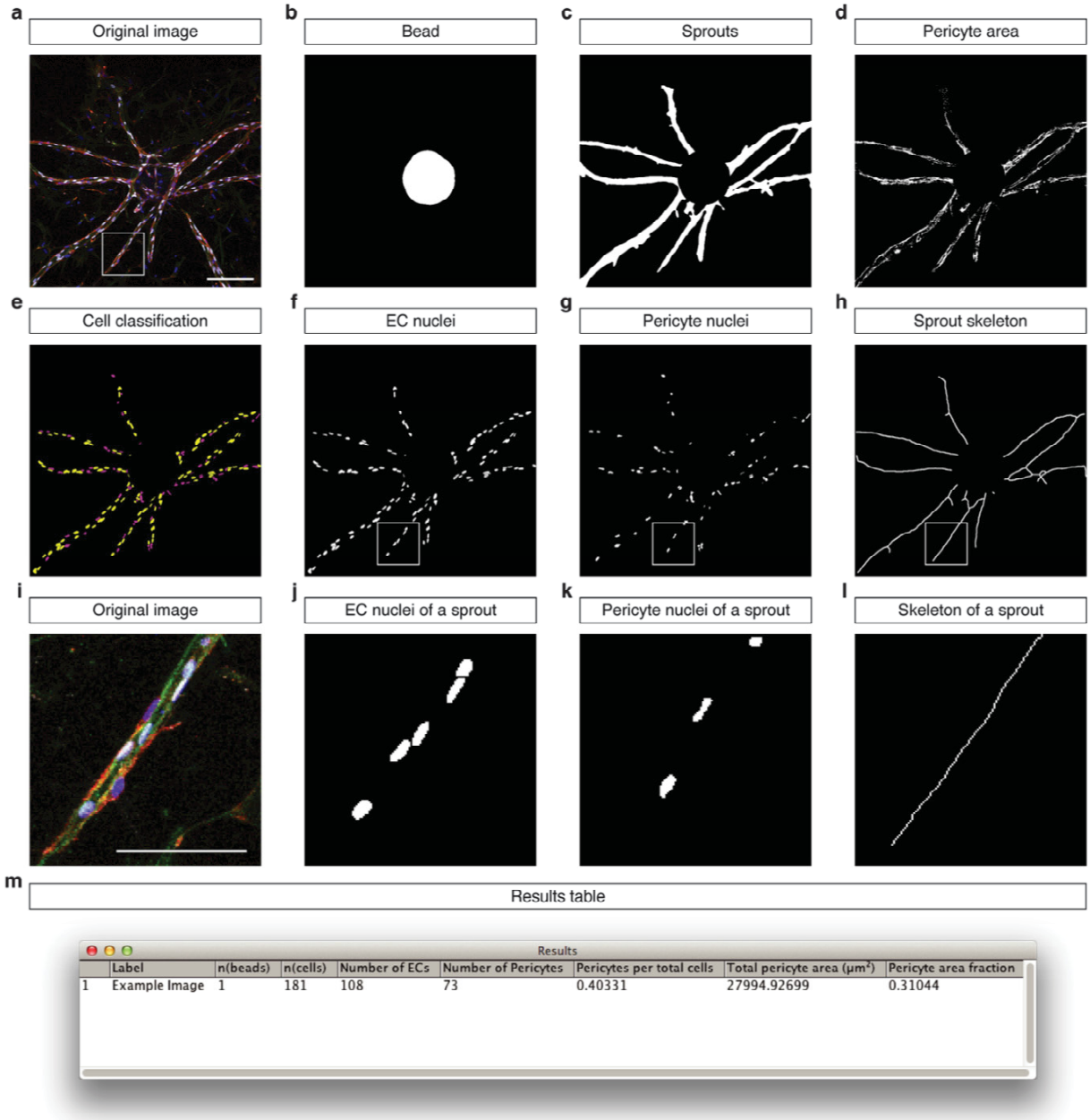

Figure 6: ***Automated multi-parametric image analysis of sprouting angiogenesis with pericytes.*** (**a**) Confocal micrograph (maximum intensity projection) showing a bead with sprouts stained for F-actin (green), nuclei (blue), endothelial nuclei (white), and pericytes (red). (**b**-**d**) Result images showing segmentation results (white): segmented bead (**b**), total sprout area (**c**) and pericyte area (**d**). (**e**) Cell classification result showing endothelial nuclei (yellow) and pericyte nuclei (magenta). (**f**-**g**) Result images from the cell classification showing EC nuclei (**f**) and pericyte nuclei (**g**). h Sprout skeleton for length measurements. (**i**-**l**) Magnified details of the marked region in (**a**, **f**-**h**). (**m**) Result table shown after running our plugin on the example image shown in **a**. Scale bars, 200 µm (**a**-**h**); 100 µm (**i**-**l**).

5.1.2.3 Assessment of small molecule modifiers of angiogenesis identifies specific modulators of pericyte coverage

Using our analysis workflow, we tested more than 40 compounds on their effect on sprout morphology and pericyte coverage (Additional file 6: Table S1). We selected in particular those compounds that target pathways reported to modulate angiogenesis (e.g., SU5416, a potent inhibitor of VEGFR-2[174]; PDGFR inhibitors[98]; Y27632, a Rho kinase inhibitor[175]; a γ-secretase inhibitor (Notch signaling)[176]; and modulators of cAMP signaling[177]) in order to come up with a set of molecules to be used in a proof-of-concept study. The results are summarized in Additional file 7: Table S2 and Additional file 8: Table S3. In sprouts consisting of only ECs, we identified compounds that significantly decreased (11 compounds) or increased (6 compounds) sprout number ($P < 0.05$) with at least one of the concentrations used (Additional file 7: Table S2). Using a cut-off value of $P < 0.01$ (to reduce the chance of finding false positives), the number of compounds considered significantly decreasing or increasing sprout number was 6 and 3, respectively. Similarly, sprout length was significantly decreased with 12 (with $P < 0.01$, 5) compounds and increased with 3 compounds (with $P < 0.01$, 1). In the presence of pericytes, none of the compounds decreased the number of sprouts significantly with the concentrations used, and only 3 compounds significantly increased sprout number (with $P < 0.01$, 0; Additional file 8: Table S3). Sprout length was significantly decreased with 8 (with $P < 0.01$, 3) compounds and significantly increased with 2 (with $P < 0.01$, 0) compounds.

For EC-only sprouts, we measured sprout width and cell density as additional parameters. We found that 8 out of 41 compounds specifically and significantly ($P < 0.05$) change sprout width and/or cell density without affecting sprout number or length (Additional file 7: Table S2). Similarly, we found that 12 out of 42 compounds specifically changed pericyte coverage in human EC/ pericyte-derived vascular sprouts (Additional file 8: Table S3).

5.1.3 Discussion

The bead sprouting angiogenesis assay in its original form as described by Nakatsu et al. has been used in a number of publications to test the specific effects of agents (e.g., siRNAs, antibodies, chemical inhibitors) on angiogenesis, and to complement results from *in vivo* experiments[178-181]. However, until now, this assay has not included the important influence of pericytes on vascular sprout formation. We believe that the presented assay compares favorably with prior uses of published assays, since the co-culture of pericytes and ECs better mimics the *in vivo* vascular system. In addition, the three-dimensional bead angiogenic sprouting assay has been used with other cell types than HUVEC such as human lung ECs[182] and human lymphatic ECs[183].

The bead sprouting assay experimental design has several advantages over many comparable *in vitro* methods, namely, a defined cellular composition including ECs and pericytes. Based on a reproducible 3D environment, the assay produces multi-cellular lumenized sprouts that possess an abluminal basement membrane[94].

The assay reproduces the cellular mechanisms necessary to form lumenized tubes, in contrast to assays that focus solely on EC migration[184]. The new ImageJ plugin allows for straightforward quantification of pericyte coverage in addition to sprout morphology (see Additional file 2: Video S2). Future applications of this assay will benefit from the detailed quantitative analysis provided by our toolkit. Admittedly, a limitation of the assay is the absence of blood flow. However, methods providing a blood flow require a more complex setup, thereby limiting the sample size. A detailed comparison of assays highlighting their respective features is shown in Additional file 9: Table S4.

With the addition of pericytes, this sprouting angiogenesis assay is useful to measure effects of different compounds on pericyte coverage. In our assay, we often observed vascular sprouts with leading ECs and pericytes in close vicinity to the endothelium, covering the abluminal side of sprouts with long cellular protrusions (Figure 6i–l). The observed sprout morphology is characteristic of pericyte-covered sprouting capillaries *in vivo*[98, 159, 160].

Within our test compounds, the number of compounds that decreased sprout number and length was higher than those that increased these two parameters. On an evolutionary-optimized cellular mechanism like angiogenesis, it is not surprising to find more inhibiting than activating factors. In addition, we observed that the presence of pericytes on the vessel walls stabilized vascular sprouts; in the EC/pericyte sprouts, fewer compounds were able to decrease sprout number, although they were used at the same concentrations in both experiments.

It should be noted that our sprouting assay, while recapitulating the *in vivo* morphology of pericyte-wrapped sprouts, suffers from the natural biological variability present in primary human cells. A careful analysis of its statistical power should therefore be performed when designing larger studies using this assay to draw meaningful conclusions. Our proof-of-concept study is limited by its small sample size, since no robotic platform for high-throughput screening was used. However, when comparing groups of compounds with shared properties, we observed similar behaviors. For example, we observed that compounds regulating intracellular cyclic adenosine monophosphate (cAMP) levels or activating protein kinase A (i.e., 6-Bnz, Forskolin, IBMX, Sp-cAMPS) tended to increase sprout width in our assay (see Additional file 7: Table S2). In addition, the assay setup also allows measuring the number of branch points per sprout, in particular when sprouts are given enough time to form branched networks and a larger sample size is used. Therefore, we also added an option to measure the number

of branch points in our plugin (Additional file 10: Figure S1), based on the “Analyze Skeleton” plugin included in Fiji[185].

The ImageJ plugin we developed provides a comprehensive quantification of morphological parameters in vascular sprouts. By providing an analysis specific to the bead sprouting assay, it helps researchers using this assay to get useful measurements, while still offering flexibility in the choice of parameters as well as the possibility of adaptations, as its source code is fully available.

Our methodology allows for quantitative assessment of morphology and pericyte coverage in vascular sprouts developed from human endothelial cells and human pericytes *in vitro*. We were also able to observe some of the expected effects of anti-angiogenic substances, such as those of VEGF and PDGF receptor inhibitors. The *in vitro* bead sprouting angiogenesis assay with pericytes therefore represents a novel, helpful addition to various *in vivo* experiments. Our plugin for ImageJ allows to quantify the results of this assay and is a novel and freely available quantification tool in the field of digital pathology.

5.1.4 Methods

5.1.4.1 Cell culture

We used HUVEC (Lonza) up to passage 6[186], HBVP (ScienCell) were used up to passage 4, and Detroit-551 human skin fibroblasts (HSF; ATCC) up to passage 20. For experimental reproducibility, primary cells were used up to the passage number recommended by the respective supplier (Lonza, ScienCell, ATCC), as primary cells lose their identity and responsiveness to angiogenic stimuli at higher passages[186]. Cells were cultured in endothelial growth medium (EGM-2; Lonza) at least 24 h prior to starting the sprouting assay.

5.1.4.2 Sprouting Assay

A detailed step-by-step protocol for the sprouting assay is available in Additional files 1, 2 and 3. The procedure is based on a sprouting assay reported previously[169-171] that we extended to include pericytes and be adaptable for culture in a 96-well plate. In short, dextran-coated Cytodex-3 microcarrier beads (GE Healthcare) were incubated with HUVEC and HBVP in EGM-2 (Lonza) overnight. We found an endothelial-to-pericyte ratio of 10:1 to yield optimal pericyte coverage of developing sprouts in accordance with cell ratios found in tissues varying between 1:1 and 10:1[160, 187]. Cell-coated beads were then embedded into fibrin gels by adding 90 µl beads in PBS (200 beads ml^{-1}) with 2.5 mg/ml fibrinogen (Sigma-Aldrich) to 8 µl thrombin (0.625 U ml^{-1}, Sigma-Aldrich) per well in a 96-well plate (µclear, Greiner Bio-One). The gels were overlaid with human skin fibroblasts at 1000 cells per well. As previously published, the cross-talk between ECs and fibroblasts, but not their direct contact, was shown to be required for the formation of stable lumenized sprouts[169]. Two hundred microliters of EGM-2 were

subsequently added to each well. Plates were incubated at 37 °C, 5% CO_2, and medium was changed every other day. After 6 days, when lumenized sprouts were observed, treatment was started by adding compounds at the respective concentrations to each well. Medium and compounds were changed every other day. The frequency of changing medium and compounds was chosen based on preliminary experiments that showed a significant decrease in sprout number and length upon treatment with the VEGFR inhibitor SU5416.

5.1.4.3 Phalloidin staining

For assays containing ECs only, fibrin gels were fixed overnight using 4% paraformaldehyde in PBS. Subsequently, gels were washed with PBS, blocked with PBS containing 0.2% Triton X-100 and 1% BSA, and stained with Alexa Fluor 488-conjugated phalloidin and DAPI (for timing and details, see protocol in Additional file 3). After three washes (10 min in PBS), the plate containing the gels was imaged as described below.

5.1.4.4 Immunostaining

Fibrin gels containing EC/pericyte sprouts were fixed using 4% paraformaldehyde in PBS. Subsequently, gels were washed with PBS, blocked with PBS containing 3% Triton X-100 and 1% BSA, incubated with primary antibodies (rabbit polyclonal anti-human Erg-1/2/3, Santa Cruz; mouse monoclonal anti-human NG2, Abcam) for at least 60 h, washed with PBS, and stained with secondary antibodies (Alexa Fluor 488 donkey anti-mouse IgG, Life Technologies; Cy3 AffiniPure donkey anti-rabbit IgG, Jackson ImmunoResearch), as well as Alexa Fluor 647-conjugated phalloidin and DAPI for at least 40 h (for timing and details, see protocol in Additional file 3). After three washes (PBS), the plate containing the gels was imaged as described below.

5.1.4.5 Microscopy

We used an inverted microscope (Zeiss Axio Observer.Z1) with an automated stage to acquire multi-tile z-stacks (10 µm intervals) of stained sprouts, using a Zeiss 10 x/NA0.45 objective lens. Both a Zeiss ApoTome system equipped with Colibri LED light source, as well as a Zeiss LSM 710 confocal microscope system were used for imaging. Images were acquired in grid positions and subsequently stitched using the Grid/Collection stitching plugin in Fiji[188], resulting in a continuous image coverage of 70% of each well (3 x 3 mm).

5.1.4.6 Image analysis

Images were analyzed using the Fiji distribution of ImageJ[189] at version ImageJ 2.0.0-rc-15/1.49k; Java 1.6.0_65 (available as a Life-Line Version from https:// imagej.net/Downloads). We developed a plugin for sprout analysis that is available from the Angiogenesis update site

within ImageJ and is maintained to work with the newest version of Fiji (see https://imagej.net/Following_an_update_site for instructions how to install the plugin in Fiji). Documentation for our plugin is available at https://imagej.net/Sprout_Morphology. For each z-stack acquired, the maximum intensity projection (MIP) was created (see Additional file 4) and processed using our plugin. For each 96-well plate, representative MIPs were used to adjust analysis parameters to improve image clarity across the entire dataset. Using the provided script (see Additional file 5), the plugin was then run on every continuous image to consistently analyze the entire dataset.

5.1.4.7 Statistical analysis

The results of the sprout analysis were normalized to either a PBS control or a DMSO control, depending on the solvent used to reconstitute each treatment com- pound (see Additional file 6: Table S1). Within one assay, the values for repeated conditions in separate wells were weighted according to the number of beads in each well. Significant increase or decrease of each measurement parameter at each treatment condition was determined using a one-sample t test.

5.1.5 Additional Information

5.1.5.1 Supplementary Information

Additional files of this manuscript are presented in section 9.1 “Supplementary Information of section 5.1” and at https://inflammregen.biomedcentral.com/articles/10.1186/s41232-016-0033-2

5.1.5.2 Availability of data and materials

The ImageJ plugin for quantitative sprout analysis is available from the update site: https://sites.imagej.net/Angiogenesis/. The source code is available from the repository at https://github.com/angiogenesis/Sprout_Analysis. The data generated for this study using our plugin are included in this published article. The full dataset is available from the corresponding author on request.

5.1.5.3 Acknowledgements

We thank the members of the Institute of Metabolic Physiology for helpful comments, in particular to M. Kelly-Goss for her helpful suggestions.

5.1.5.4 Competing interests

The authors declare that they have no competing interests.

5.1.5.5 Authors & author details

J. Eglinger[1,2,3*], **H. Karsjens[1,2]** & E. Lammert[1,2]

[1]Institute of Metabolic Physiology, Heinrich-Heine University, Düsseldorf, Germany. [2]Institute for Beta Cell Biology, Leibniz Center for Diabetes Research, German Diabetes Center (DDZ), Düsseldorf, Germany. [3]Current address: Friedrich Miescher Institute for Biomedical Research, Basel, Switzerland.

5.1.5.6 Authors` contribution

See section 5.1.6 “Personal contribution and general information”.

5.1.5.7 Funding

This work was supported by the German Center for Diabetes Research (DZD e.V.), the Federal Ministry of Health, and the Ministry for Innovation, Science and Research of North Rhine-Westphalia.

5.1.5.8 Consent for publication

Not applicable.

5.1.5.9 Ethics approval and consent to participate

Not applicable.

5.1.6 Personal contribution and general information

Personal contribution of Haiko Karsjens (HK) to the manuscript “Quantitative assessment of angiogenesis and pericyte coverage in human cell-derived vascular sprouts” that was published in the journal of inflammation and regeneration in 2017. Contrary to the online version of this article, the numbering of the figures and citations was changed, the conclusions part was included into the discussion part and the chronology of single parts was modified to achieve consistency within this thesis.

Name of the journal:	Inflammation and Regeneration
Impact factor (2017):	0.31
Author position:	Second author
Tasks:	Correction of manuscript, figures, tables and supplement. developing the staining protocol to distinguish between endothelial cells and pericytes.

Author`s contribution (as written in the manuscript):

JE performed the assay experiments, prepared the figures, performed the statistics, programmed the ImageJ plugin, and wrote the manuscript. **HK** optimized the immunostaining procedure for 96-well plates. EL supervised JE and **HK** during their Ph.D. theses, provided advice, and wrote the manuscript together with JE. All authors read and approved the final manuscript.

Contribution in detail:

HK transferred the staining protocol from glass-bottom dish to multi-well format, which allows large scale compound testing. Furthermore, **HK** developed a staining protocol in 96-well plates that enables distinction between endothelial cells and pericytes within a vascular sprout. This in turn allowed the analysis of pericyte coverage.

HK contributed to the experiments for the following figures: Figure 4d,e; Figure 5c,f,i,l,n,p; Figure 6a-j

In sum, Haiko Karsjens contributed to the work of this manuscript with approximately 20%.

5.2 The biomechanical properties of an epithelial tissue determine the location of its vasculature

This paragraph contains the published research article “The biomechanical properties of an epithelial tissue determine the location of its vasculature” (Kragl et al.[2]). The article shows that the adaptor protein integrin-linked kinase controls the flexibility of pancreatic epithelial cells and thereby enables blood vessels to penetrate the pancreatic islet.

5.2.1 Background

Formation and maintenance of a blood vessel network has a key role both during development and disease[190, 191]. In pancreatic islets, a dense network of blood capillaries contributes to glucose homeostasis by transporting blood glucose to and insulin (the key blood glucose-lowering hormone) from pancreatic beta cells (the major endocrine cell type in pancreatic islets)[11]. The beta cells interact with blood vessels via the vascular basement membrane that surrounds the islet capillaries[192]. Several *in vitro* studies on rodent and human islets, pancreatic beta cells, and pancreatic epithelium provided evidence that their integrins bind to basement membranes and endothelial cell-derived factors to facilitate beta cell differentiation, proliferation, and function[120, 130, 193]. Some, but not all, *in vivo* studies also support a role of integrins in beta cell proliferation and function[127, 194-196]. Notably, integrin-linked kinase (ILK) binds to the cytoplasmic tails of integrins expressed in pancreatic islets[132].

Here we investigated the role of ILK in islet endocrine cells *in vitro* and *in vivo* and found that knockdown of *Ilk* in mouse insulinoma cells and deletion of *Ilk* in the pancreatic epithelium of mice reduce the adhesion strength of the endocrine cells to a vascular endothelial cell line, while at the same time increase cortex tension of the endocrine cells. The latter findings help to explain why deletion of *Ilk* in pancreatic epithelium leads to a loss of the intra-islet vasculature and excessive accumulation of the vasculature at the islet periphery. Notably, the sum of intra- and peri-islet vascular endothelial cells was unchanged, no ‘empty sleeves’ of vascular basement membrane were observed during the onset of this vascular phenotype, and endothelial cell proliferation, apoptosis and morphology as well as secretion of vascular endothelial growth factor-A (VEGF-A) were not altered. The data suggest a mechanical sorting event, rather than a chemotactic one in response to angiogenic growth factors, driving the segregation of vascular endothelial cells and *Ilk*-deficient endocrine cells during pancreatic islet growth.

5.2.2 Results

5.2.2.1 Requirement of *Ilk* for normal insulin secretion *in vivo*

First, we specifically deleted *Ilk* in the pancreatic epithelium by generating pancreas-duodenum homeobox 1 (*Pdx1*)-*Cre*; $Ilk^{loxP/loxP}$ mice (referred to as ILK cKO hereafter) (Supplementary Figure 1). In adult mice, a strong reduction of *Ilk* messenger RNA (mRNA) and protein expression was observed in ILK cKO islets compared with those of heterozygous control islets (Supplementary Figure 1a, b). The ILK cKO mice appeared to be normal in their fasting blood glucose concentrations, but exhibited a reduced glucose tolerance when challenged in an intra-peritoneal glucose tolerance test (Figure 7a, b). Moreover, after an intraperitoneal glucose injection, plasma insulin concentrations failed to rise in ILK cKO mice at 30 min post injection, but did rise after 120min, indicating a delayed insulin secretion from pancreatic islets (Figure 7c). In contrast, insulin tolerance remained normal (Supplementary Figure 1c, d).

Next, we measured insulin secretion from isolated control and ILK cKO islets under low (2.5mM) and high (20mM) glucose concentrations *in vitro*. To our surprise, and in contrast to the *in vivo* situation, virtually no reduction of glucose-stimulated insulin secretion from *Ilk*-deficient islets was observed *in vitro* when compared with control islets (Figure 7d). Further, ILK cKO islets had a normal insulin content and also responded to an increase in glucose concentration from 5 to 10mM with enhanced insulin release (Supplementary Figure 1e, f).

5.2.2.2 Mislocalized pancreatic islet vasculature in ILK cKO mice

To explain the discrepancy between the *in vitro* and *in vivo* situation, we next investigated whether the *in vivo* failure of ILK cKO mice to rapidly increase plasma insulin concentrations upon glucose injection might have been caused more by a failure of the ILK cKO islets to deliver insulin into the blood stream than a failure of these islets to secrete insulin. The islet capillary network enables glucose tolerance by distributing insulin from islets to peripheral tissues[91, 92, 197]; thus, we analyzed islet vascular networks in the pancreas from ILK cKO and heterozygous control mice (Figure 7e). Notably, immunohistochemical staining of pancreatic sections from adult mice for the endothelial cell marker CD31 revealed a striking defect in vascular organization of ILK cKO islets (Figure 7e), implicating a possible reason for the failure of ILK cKO mice to control blood glucose concentrations (Figure 7a, b).

An ~80% reduction of intra-islet capillaries was observed in ILK cKO islets (Figure 7e), while no signs of increased hypoxia were noted (Supplementary Figure 2). In contrast, significantly more blood vessels were found at the islet periphery (Figure 7e). Notably, the total number of islet endothelial cells, or the sum of intra- and peri-islet endothelial cells, did not significantly differ between control and ILK cKO islets (Figure 7e; Supplementary Movies 1 and 2). Moreover, a similar vascular phenotype was observed when the *Ilk* gene was deleted using a previously published beta cell-specific *Ins1*(*Cre*) knock-in mouse[198] (Supplementary

Figure 3). Further, after transplantation of ILK cKO and control islets into the anterior eye chamber of mice, a dense intra-islet vascular network was found in control islets 28 days post transplantation, whereas the intra-islet blood vessel density was reduced in ILK cKO islets (Supplementary Figure 4a). To further describe the glucose intolerance and delayed insulin release observed in ILK cKO mice, we investigated whether the islet capillaries were perfused. After injection of a fluorescein isothiocyanate (FITC)-labelled tomato lectin into the tail vein of mice, all analyzed islet vessels were coated with the fluorescent lectin (Supplementary Figure 4b), indicating that the blood vessels in ILK cKO islets were perfused despite their altered localization.

5.2.2.3 Postnatal onset of vascular phenotype in ILK cKO mice

To gain more insight into how ILK in islet endocrine cells affects the intra-islet vasculature, we analyzed the age at which changes in the islet vasculature were first detected (Figure 7f). We noted that the mRNA for ILK was reduced in islets 7 days after birth, but more strongly reduced 14 days after birth (Supplementary Figure 1g). Thus, we quantified islet vascular endothelial cells of newborn mice at 1, 7 and 14 days after birth (P1, P7 and P14, respectively). Islets in P1 and P7 ILK cKO mice appeared to be normal in their blood capillary distribution (Figure 7f-i). In contrast, P14 mice displayed an islet vascular phenotype similar to the one observed in adult ILK cKO mice with depleted intra-islet, elevated peri-islet and unchanged total islet endothelial cell counts (Figure 7f-i), showing that the vascular phenotype develops between P7 and P14.

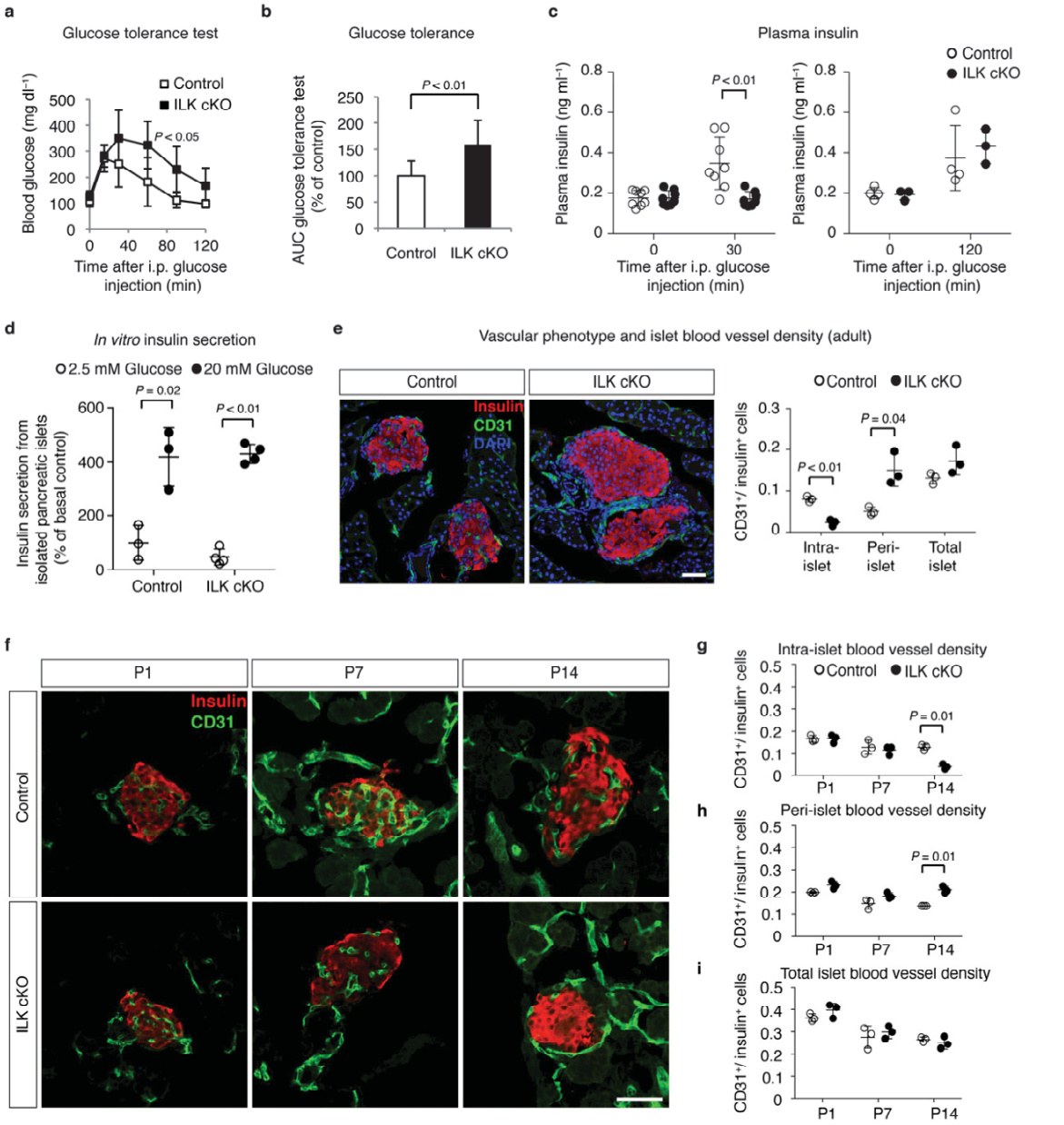

Figure 7: ***ILK in pancreatic islets is required for a normal localization of their vasculature.*** (**a**) Blood glucose concentrations during a glucose tolerance test in male ILK cKO mice (filled squares) and heterozygous littermate controls (unfilled squares) at the age of 7 weeks. Glucose (1 g kg^{-1} body weight) was injected i.p. at 0 min. *N* = 7-8 mice per experimental group. (**b**) Area under curve of data shown in **a**. (**c**) Plasma insulin concentrations in male ILK cKO and control mice (10-weeks-old). Glucose (1 g kg^{-1} body weight) was injected i.p. at 0 min. *N* = 8 mice per experimental group for 0 and 30 min (left panel), and *N* = 3-4 mice per group for 0 and 120 min (right panel). (**d**) Insulin secretion from isolated pancreatic islets of ILK cKO and control mice at 2.5 mM (white dots) or 20 mM (black dots) glucose. Secreted insulin is normalized to total insulin levels. *N* = 3-4 islet batches each. (**e**) Laser scanning microscopy (LSM) images of immunofluorescence staining for insulin (a marker for pancreatic beta cells) and CD31 (a marker for blood vessels) of pancreatic sections from 12-weeks-old control and ILK cKO mice. Quantification of intra-islet, peri-islet and total islet blood vessel densities in ILK cKO and control mice. N = 3 animals per experimental group, 8-10 islets were analyzed per animal. (**f**) LSM images of immunofluorescence staining for insulin and CD31 in pancreatic sections from 1 day (P1), 7 days (P7) and 14 days (P14) old control and ILK cKO mice. (**g**–**i**) Quantification of (**g**) the intra-islet vascular density, (**h**) the peri-islet vascular density and (**i**) the total islet vascular density, each relative to the insulin þ pancreatic beta cell number. *N* = 3 animals per experimental group with 28-39 (P1), 53-114 (P7) and 47-77 (P14) islets analyzed per animal. Data are shown as mean values ± s.d., **P* < 0.05 in an unpaired, two-sided Student's t-test with (**a**) Holm-Bonferroni correction. Scale bars, 50 µm (**e**, **f**).

5.2.2.4 Normal VEGF-A secretion from ILK cKO islets

Next, we investigated the mechanism by which ILK in endocrine, non-endothelial pancreatic cells affected islet vascularization. ILK has been shown to influence gene transcription, as well as cell proliferation, adhesion and motility, depending on the cell and tissue type in which it is expressed[132]. Thus, a number of possible scenarios could explain the novel vascular phenotype observed in the pancreatic islets upon *Ilk* deletion. As formation and maintenance of the islet vasculature strictly depends on VEGF-A[91, 92, 106, 199], we wondered whether ILK promotes islet vascularization by maintaining VEGF-A expression. Interestingly, prior studies using a few murine models of cancer demonstrated that inhibition of ILK decreased hypoxia-induced *Vegfa* gene transcription[200, 201]. We, therefore, quantified *Vegfa* mRNA levels in control and ILK cKO islets (Figure 8a). However, we did not observe lower expression of *Vegfa* that could explain the reduced blood vessel density in islets upon *Ilk* deletion (Figure 8a). Likewise, we did not detect any reduction in VEGF-A secretion from isolated ILK cKO islets (Figure 8b). Consistent with these results, ILK cKO islets did not resemble islets lacking VEGF-A, which are generally depleted of both intra-islet and peri-islet blood vessels[91, 92, 106, 199]. Further, immunohistochemical staining of pancreases in the adult and at P10, the time at which the vascular phenotype starts to develop, revealed no obvious changes in the localization of VEGF-A within the islets (Supplementary Figure 5). The data, therefore, suggest that in pancreatic islets ILK does not support vascular density by increasing expression, changing location or secretion of VEGF-A.

Apart from VEGF-A, many other pro- and anti-angiogenic growth factors are known, making it possible that ILK depletion affects another factor. For example, some, but not all studies reported that angiopoietins have a role in islet vascularization[202-204]. We thus quantified the mRNA levels of Angiopoietin-1 and Angiopoietin-2, but did not detect any difference between control and ILK cKO islets either (Supplementary Figure 6a, b). Similarly, the expression of the anti-angiogenic isoforms of *Vegfa* were not different (Supplementary Figure 6c)[205]. Since most pro- and anti-angiogenic factors affect endothelial cell survival, proliferation and morphology[91, 92, 190, 191], we next analyzed these parameters in control versus ILK cKO islets. Vascular endothelial cell proliferation in ILK cKO islets was found to be only slightly and non-significantly reduced, and this tendency was observed for both intra- and peri-islet endothelial cells (Figure 8c), thus being unable to explain the inverse change of endothelial cell number in islet core and periphery. Moreover, apoptotic endothelial cells were not detected in the islets of ILK cKO mice, neither at P7 nor at P10 (Supplementary Table 1), indicating that increased endothelial cell death is not responsible for the lack of intra-islet capillaries. Further, the ultrastructure of intra-islet capillaries, including the presence of fenestrations and vascular basement membrane, was investigated at P7 and P14 and found to be largely unchanged (Figure 8d). In P10 and adult ILK cKO islets, blood vessels stained

positive for the vascular basement membrane proteins laminin and fibronectin (Figure 8e, f; Supplementary Figure 7), and were covered with NG2-positive pericytes (Supplementary Figure 8). In addition, the staining of these basement membrane proteins and NG2 overlapped with the CD31 staining of endothelial cells (Figure 8e, f; Supplementary Figures 7 and 8). Based on these results, it seemed unlikely that mainly alterations in pro- or anti-angiogenic growth factor expression and secretion accounted for the striking vascular phenotype observed.

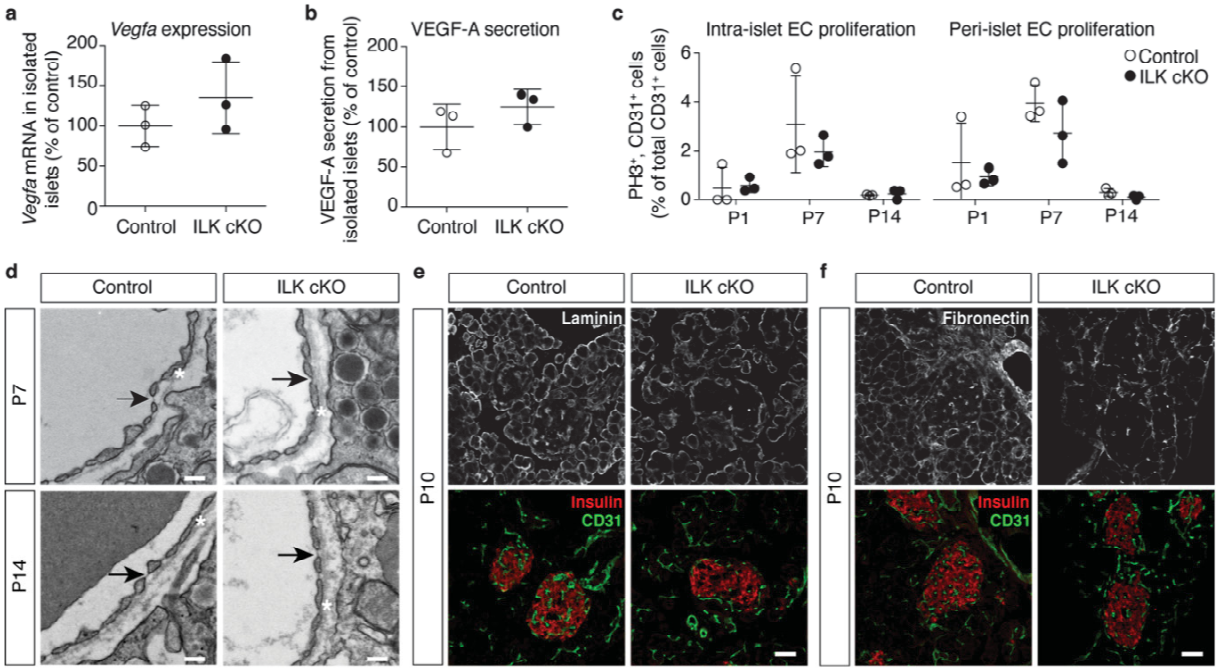

Figure 8: ***ILK in islets is required for neither endothelial cell proliferation nor survival.*** (**a**) Quantification of relative Vegfa mRNA levels in control versus ILK cKO islets. *N* = 3 animals per experimental group. (**b**) Quantification of VEGF-A protein secreted from control versus ILK cKO islets. *N* = 3 islet batches for each experimental condition. (**c**) Quantification of proliferating intra-islet vascular endothelial cells (left) and peri-islet endothelial cells (right). $CD3^+$, phospho-histone 3 $(PH3)^+$ cells are shown as percentages of the total number of intra-islet and peri-islet $CD31^+$ cells, respectively, in islets of pancreatic sections from mice at the age of 1, 7 and 14 days. *N* = 3 animals per experimental group. A total number of 167–337 (P1), 314–688 (P7) and 113–659 (P14) $CD31^+$ intra-islet endothelial cells and a total number of 159–371 (P1), 193–607 (P7) and 441–628 (P14) $CD31^+$ peri-islet endothelial cells per animal were analyzed. (**d**) Transmission electron microscopy images of capillaries in a control and an ILK cKO islet. Arrows point to the fenestrations in the blood vessel wall, which are typical of islet capillaries and require VEGF-A signaling, and asterisks indicate the location of basement membrane surrounding the islet capillary. (**e**, **f**) LSM images of immunofluorescence staining for laminin or fibronectin (white), insulin (red) and CD31 (green) in pancreatic sections from 10-day-old control and ILK cKO mice. Data are shown as mean values ± s.d., **P* < 0.05 in an unpaired, two-sided Student's t-test. Scale bars, 200 nm (**d**); 50 µm (**e**, **f**).

5.2.2.5 ILK cKO mice show no change in beta cell proliferation

Another possible mechanism to explain the phenotype could reside in increased endocrine cell proliferation upon *Ilk* deletion, as the deletion of *Ilk* was recently reported to increase hepatocyte proliferation[206]. We thus asked whether a 'dilution' of vascular endothelial cells, caused by an increased endocrine pancreatic cell proliferation, could account for the reduced intra-islet vascular density observed upon *Ilk* deletion. However, analysis of the average number of beta cells per islet did not reveal any difference between islets from ILK cKO animals versus control littermates (Supplementary Figure 9a). Similarly, neither the adult beta cell mass nor the proliferation rate of beta cells in the newborn pancreas changed upon *Ilk* deletion (Supplementary Figure 9b, c). Therefore, the vascular phenotype cannot be explained with an increased endocrine to endothelial cell number within the pancreatic islets.

5.2.2.6 Failure of ILK cKO islets to adhere to basement membrane

Searching for a reason behind the observed vascular phenotype, we considered its postnatal manifestation. During mammalian embryonic development, endocrine cells derive from pancreatic epithelium and vascular endothelial cells aggregate to form highly vascularized islet cell clusters[11]. After birth, these islet cell clusters expand along with their vasculature, undergo morphogenetic changes, and mature into glucose-responsive, vascularized pancreatic islets[207]. While islet vascularization appeared to be normal in the islets of newborn mice, the observed vascular phenotype is established during postnatal islet growth. The separation of endocrine pancreatic cells and vascular endothelial cells during that time reminded us of cell sorting events, such as the segregation of cell lineages during zebrafish gastrulation or pattern formation during embryonic development[208-210]. A prominent explanation of these cell sorting events is the modified Steinberg's differential adhesion hypothesis, proposing that different tissues act like liquids whose different degrees of surface adhesion cause them to either adhere or separate from each other[211, 212]. Since several studies showed that ILK promotes cell–cell and cell–matrix adhesion during developmental processes and pathogenesis[137, 152, 213-216], we hypothesized that during postnatal growth, ILK in endocrine pancreatic cells facilitates their adhesion to blood vessels to prevent the vascular endothelium from segregating from the pancreatic islet.

Since blood vessels are surrounded by a basement membrane mainly deposited by vascular endothelial cells, we first studied whether ILK depletion in endocrine pancreatic cells reduces their adhesion to the endothelial basement membrane. This hypothesis implies that blood vessels and their vascular basement membrane separate from the islet core simultaneously, leaving behind no 'empty sleeves' characteristic of blood vessel regression usually observed upon deprivation of angiogenic growth factors[106]. To our knowledge, the latter phenotype has not yet been described during vascular regression, be it from an organ or a

tumour[106, 217]. To study this scenario, pancreatic sections were stained for CD31 and collagen IV (a component of the vascular basement membrane). As with vascular endothelial cells, there was a significant reduction of collagen IV in ILK cKO islets versus control islets (Figure 9a). Notably, no 'empty sleeves' of vascular basement membrane were observed[106, 217]; that is, no basement membrane was found in the islet that did not co-localize with an endothelial cell (Figure 9a). The latter observation also holds true for pancreatic islets at P10 where the vascular phenotype just starts to establish, as seen in four images taken from pancreatic islets at P10 and stained for CD31, collagen IV and insulin (Fig. 3b–d). Compared with control islets, ILK cKO islets presented an ~40% reduction of the blood vessel and collagen IV area at P10 with no difference observed between the CD31 and collagen IV areas in ILK cKO islets (Figure 9d). Therefore, ILK might be required to provide endocrine pancreatic cells with sufficient adhesive strength to prevent the vasculature with its basement membrane from separating out of the islet.

To directly test whether ILK-depleted islets differed from control islets in their adhesion strength, islets were plated on a reconstituted basement membrane (that is, growth factor-deprived matrigel) as well as two basement membrane components (that is, collagen IV and fibronectin). After showing that ILK-depleted islets did not significantly differ from control islets in their cell survival upon cultivation (Figure 9e), islets were plated and incubated for 7 days (Figure 9f). Whereas the majority of control islets adhered to the basement membrane components, most ILK cKO islets failed to do so (Figure 9f, g; Supplementary Movies 1 and 2), supporting the notion that pancreatic islet cells fail to adhere to the basement membrane of the blood vasculature as a possible reason for the segregation of islets and blood vessels.

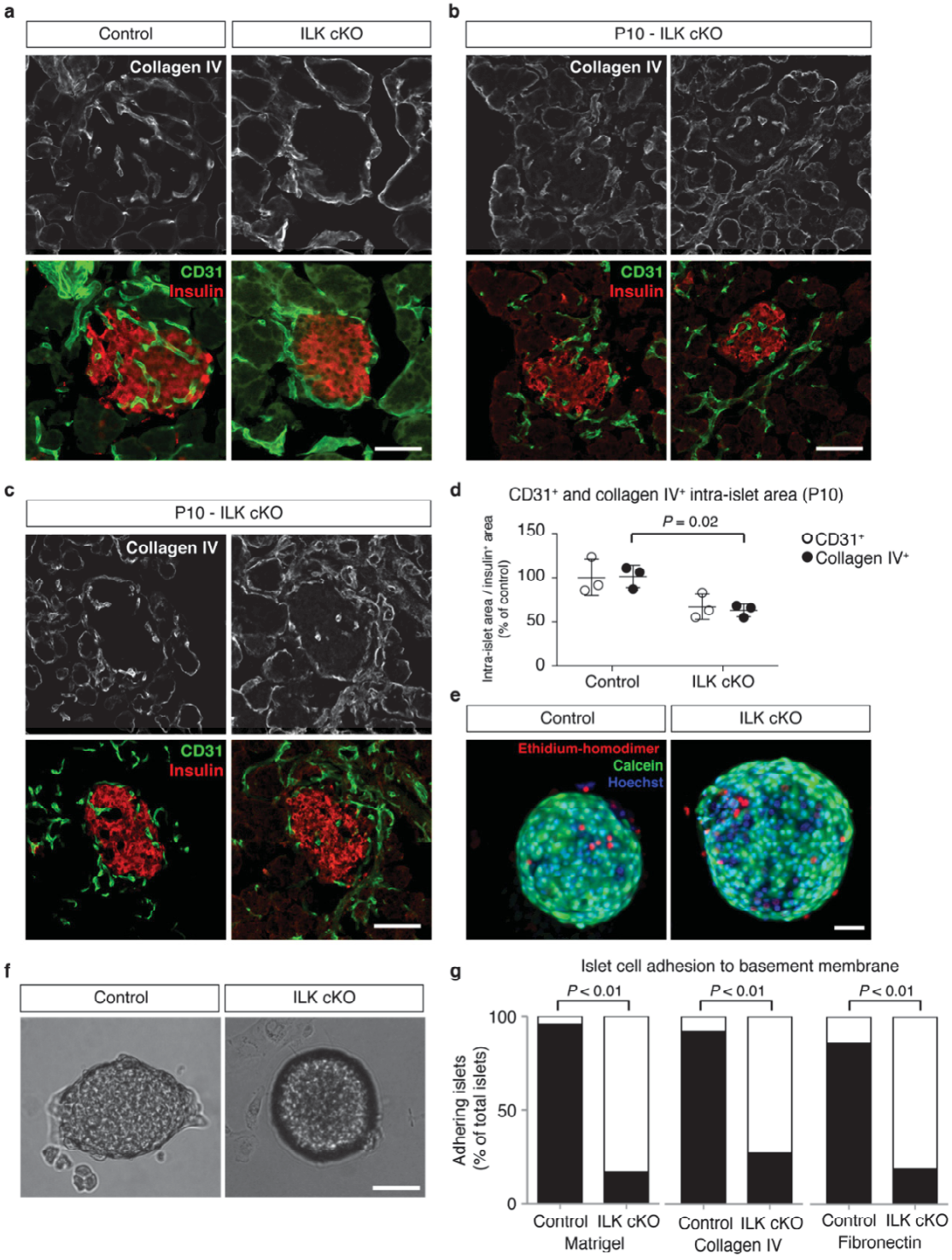

Figure 9: ***Reduced endocrine pancreatic cell adhesion to basement membrane components.*** (**a**-**c**) LSM images of immunofluorescence staining for CD31 (green), insulin (red) and collagen IV (a basement membrane protein shown in white) of pancreatic sections from 3-weeks control and ILK cKO mice (**a**) and 10-days-old ILK cKO mice (P10) (**b**,**c**). (**d**) Quantification of the intra-islet CD31 and collagen IV positive areas within control and ILK cKO islets of 10-days-old mice. *N* = 3 animals per experimental group. (**e**) Live cell imaging of a representative control and ILK cKO islet cultured for 7 days. Living cells were stained with calcein (green), dead cells with ethidium homodimer-1 (red), and all cell nuclei with Hoechst (blue). (**f**) Representative control and ILK cKO islets 7 days after plating on fibronectin. (**g**) Summary of control and ILK cKO islets adhering to matrigel, collagen IV and fibronectin. *N* = 25 control and 35 ILK cKO islets for matrigel, *N* = 48 control and 41 ILK cKO islets for collagen IV, and *N* = 22 control and 16 ILK cKO islets for fibronectin. Data are shown as mean values ± s.d., **P* < 0.05 in a two-way ANOVA followed by Tukey's multiple comparison test (**d**), and in a Fisher's exact test (**g**). Scale bars, 50 µm.

5.2.2.7 ILK cKO cells poorly adhere to endothelial cells

Next, we used an atomic force microscope (AFM) to perform single-cell force spectroscopy (SCFS) (Figure 10). This technique allows the measurement of adhesive forces between two single cells or tissues, as well as a single cell or tissue and a substrate (Figure 10)[218]. Briefly, SCFS uses a cantilever on which the cell or tissue probe is immobilized and then brought into contact with an adherent cell or a substrate. Adhesive forces are measured by the retraction of the cantilever after a pre-defined contact time in a range of several seconds or minutes. The adhesion strength is measured by the retraction-induced deflection of the cantilever (Figure 10a ,b)[218-220].

First, we quantified the adhesive forces between vascular endothelial cells and whole pancreatic islets (Figure 10b), with either control or ILK cKO endocrine pancreatic cells (Figure 10c). For this experiment, we used Ms1 cells, which are immortalized pancreatic islet microvascular endothelial cells that produce vascular basement membrane components, including collagen IV (ref. [221]). Notably, a lower adhesion strength was observed between ILK cKO pancreatic islets and Ms1 endothelial cells compared with control islets and Ms1 cells (Figure 10c, d), in particular at a contact time of 20 s. The latter finding indicates a defective time-dependent strengthening of the adhesion between the pancreatic islets and vascular endothelial cells when ILK is absent from the endocrine pancreatic cells.

Second, since islets consist of different cell types besides endocrine pancreatic cells, including those in which *Ilk* was not deleted using the *Pdx1* promoter (such as fibroblasts or Schwann-like cells), we next tested whether similar or even stronger effects could be observed by replacing the islets with immortalized mouse pancreatic beta cells (that is, MIN6 cells)[222] in which we silenced the *Ilk* transcripts using short interfering RNA (siRNA) (Figure 10e; Supplementary Figure 10a). Consistent with our observations in whole pancreatic islets, we observed a time-dependent difference in the adhesion strength between *Ilk*-silenced MIN6 epithelial cells and Ms1 endothelial cells (Figure 10e, f). That is, silencing *Ilk* reduced adhesion strength between pancreatic beta cell and endothelial cell lines. Similar results were reproduced when control- and *Ilk*-silenced MIN6 cells were separated from matrigel and collagen IV (Supplementary Figure 10b, c). As a positive control, the gene for β1 integrin (*Itgb1*) was silenced in MIN6 cells (Supplementary Figure 11a), and this also reduced the adhesion of MIN6 cells to Ms1 endothelial cells (Supplementary Figure 11b).

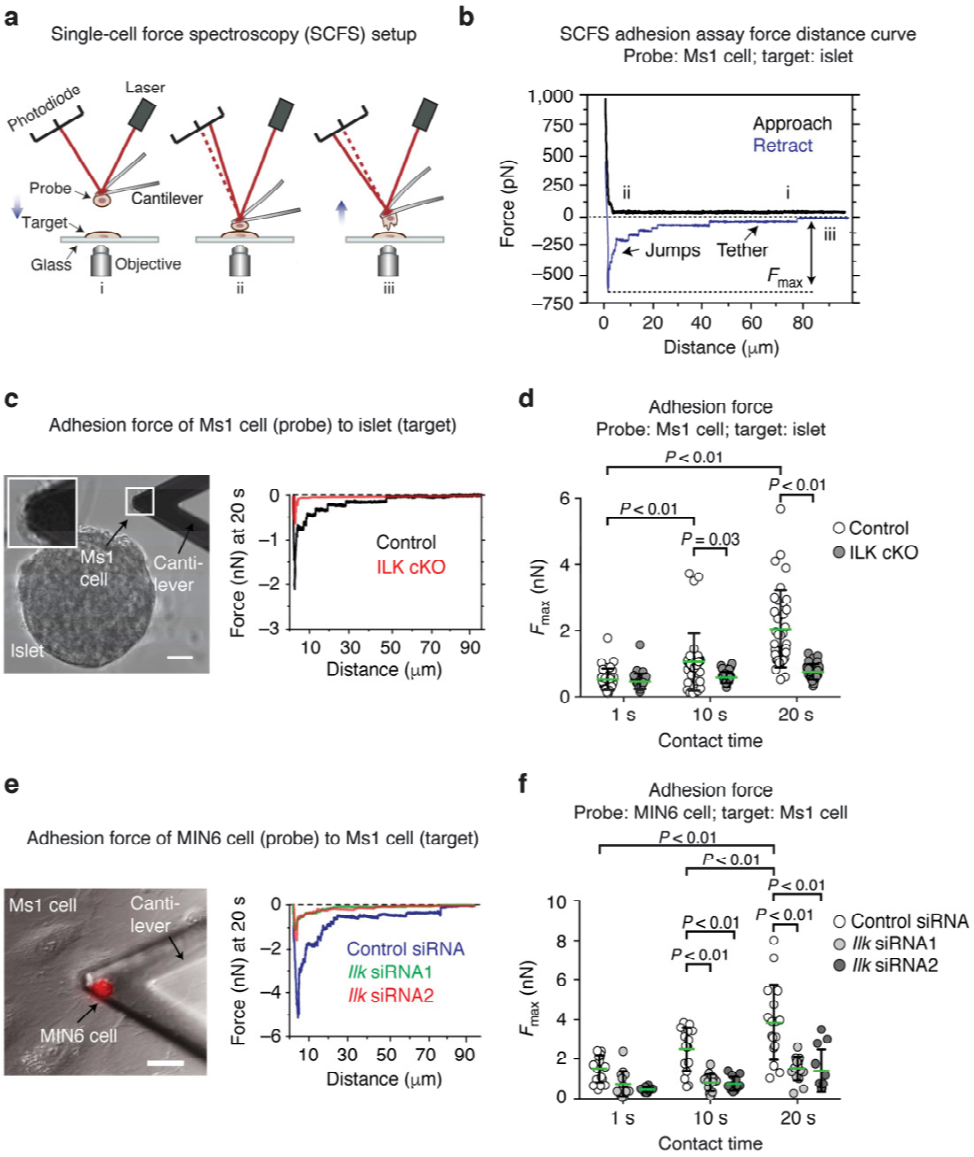

Figure 10: ***Endocrine pancreatic cells require ILK for adhering to vascular endothelial cells.*** (**a**) Outline of a single-cell force spectroscopy (SCFS) experiment. A single cell or islet 'probe' immobilized on an atomic force microscopy (AFM) cantilever is approached into contact with a 'target' cell or islet (i). After a predefined contact time (ii), the probe was retracted at 5 μm s^{-1}, and adhesive forces were detected recording the cantilever deflection over the distance travelled by the cantilever (iii). (**b**) The force-distance curve records the maximum adhesion force (F_{max}) between the probe (Ms1 endothelial cells) and target (pancreatic islets). (**c**) Representative image and adhesion force curves between Ms1 vascular endothelial cells (probe; see the inset in the image) and control (black) versus ILK cKO (red) islets. (**d**) Adhesion forces between Ms1 cells (probe) and mouse pancreatic islets (target). *N* = 36 different Ms1 cells versus 36 different control pancreatic islets and 34 different Ms1 cells versus 34 different ILK cKO pancreatic islets were tested. The green lines indicate average values. (**e**) Representative image and adhesion force curves between MIN6 cells (probe; a MIN6 cell stained in red) and Ms1 microvascular endothelial cells (target). (**f**) Adhesion forces measured between MIN6 cells (probes), treated with either control or two *Ilk* siRNAs, and Ms1 endothelial cells as targets. *N* = 12–17 MIN6 cells versus N = 12-17 different Ms1 cells were tested per experimental condition (contact time and siRNA treatment). The green lines indicate average values. Data are shown as mean values ± s.d., **P* < 0.05 in a two-way ANOVA followed by Tukey's multiple comparison test. Scale bars, 15 μm (**c**,**e**).

5.2.2.8 High cortex tension in ILK cKO pancreatic islet cells

Our findings suggest that the segregation between ILK-depleted islets and their blood vasculature was due to defects in endocrine pancreatic cell adhesion to blood vessels. However, we are aware that Steinberg's hypothesis was modified soon after its release[223], since the binding energy of adhesion molecules is not sufficient to account for cell sorting events[224-228]. Recent experimental and theoretical studies have supported the hypothesis that differential cell cortex tension along with differential cell adhesion drive the segregation of cell populations[209, 229-231]. In different experimental set-ups, an elevated cortical actomyosin contraction has been shown to increase the cell cortex tension[232-234]. Since ILK has been reported to suppress actomyosin-mediated cell contractility[132, 152, 215], we asked whether ILK might reduce cortex tension in pancreatic endocrine cells, thus contributing to a better adhesion of these epithelial cells to the vascular endothelial cells.

Since non-muscle myosin II isoforms are expressed in endocrine pancreatic cells[235], and since, to our knowledge, the role of ILK in cell cortex tension has not yet been studied, we measured cortical tension in control versus ILK-silenced islet cells. To this end, we deformed the surface of dissociated pancreatic endocrine cells with a colloidal force probe and recorded force-indentation curves required for deformation (Figure 11a, b)[209]. On average, we recorded a twofold increase in cortex tension in the ILK cKO pancreatic islet cells compared with control cells (Figure 11c). Consistent with this finding, a significantly higher cell cortex tension was also observed in ILK-depleted (but not β1 integrin-depleted) MIN6 cells versus control-treated cells (Figure 11d; Supplementary Figure 11c).

To test whether the elevated cortex tension observed upon ILK depletion required actomyosin contraction, we treated control- and ILK-depleted pancreatic islet and MIN6 cells with blebbistatin, a widely used inhibitor of myosin II[209, 236]. We also applied Y27632, a frequently applied inhibitor of Rho-associated protein kinase (ROCK)[237], which was previously shown to be downstream of ILK[152, 215]. The levels of cortex tension were reduced by both treatments, and no longer significantly differed between control and ILK-depleted islet cells (Figure 11c, d), suggesting that actomyosin contraction significantly contributed to the increased cell surface tension observed in ILK-depleted endocrine pancreatic cells. Furthermore, phalloidin staining of control pancreatic islets cultured on fibronectin revealed a reorganization of their cortical actin cytoskeleton towards the basement membrane (Supplementary Figure 12a). In stark contrast, this kind of reorganization was not observed in ILK cKO pancreatic islets (Supplementary Figure 12a; Supplementary Movies 3 and 4), consistent with the observed increase in actomyosin-mediated cortex tension, which has been reported to make cells more rigid and less compliant[238]. To directly test whether the increased actomyosin contraction in ILK-depleted endocrine pancreatic cells was required to reduce their adhesion to vascular endothelial cells, we dissociated control and ILK cKO pancreatic islets,

treated them with blebbistatin or Y27632 and performed SCFS (Supplementary Figure 12b). Notably, upon blebbistatin or Y27632 treatment, similar forces were needed to separate ILK cKO pancreatic islet cells and control islet cells from Ms1 cells, showing that lowering the actomyosin contraction rescued the adhesion of ILK-depleted endocrine pancreatic cells to vascular endothelial cells (Supplementary Figure 12b). Similar results were obtained when MIN6 cells were treated with two different ROCK inhibitors (Supplementary Figure 12c).

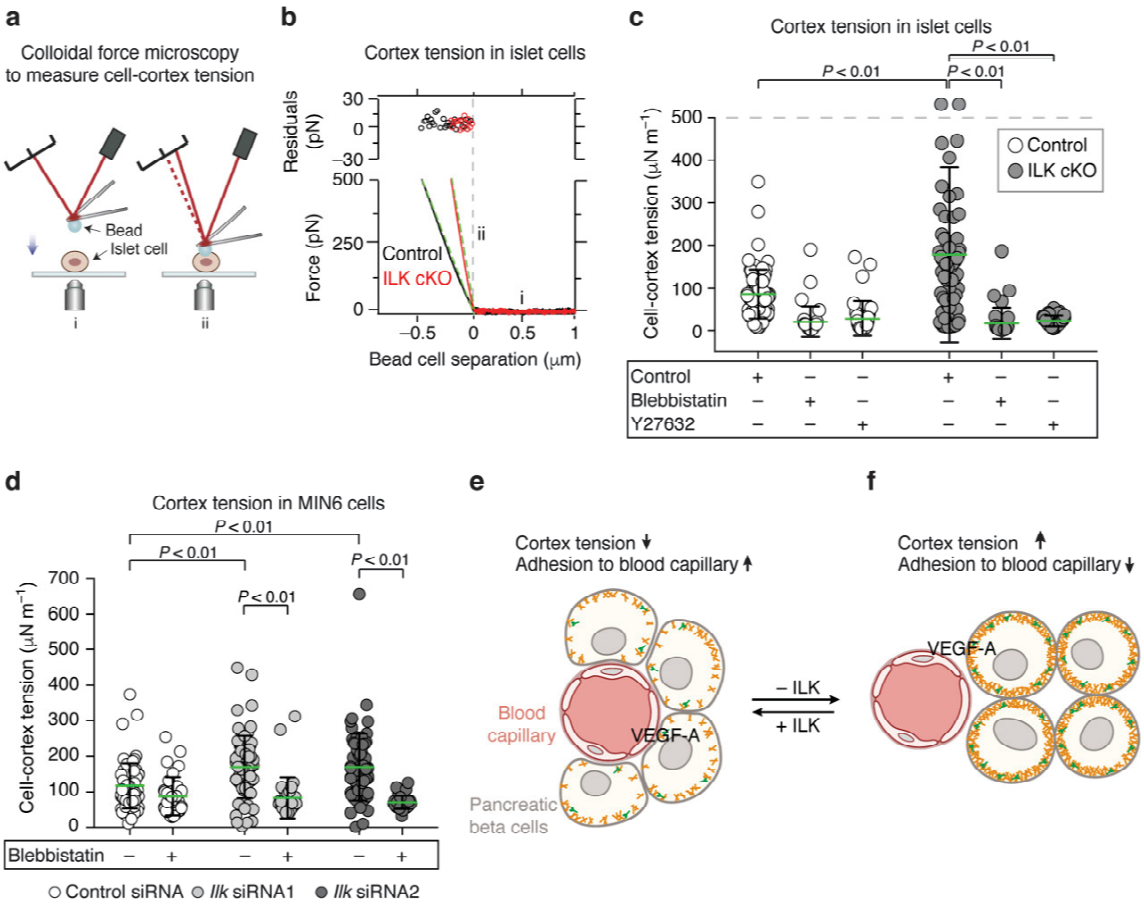

Figure 11: ***ILK regulates cortex tension via actomyosin in endocrine pancreatic cells.*** (**a**) Scheme to illustrate the principle of cortex tension experiment. A passivated bead attached to a tipless AFM cantilever is moved towards the endocrine pancreatic cell surface at 1 μm s^{-1} (i) and the surface is deformed by the bead (ii). (**b**) Representative force curves used for measuring cell cortex tension in control versus ILK cKO pancreatic islet cells. Cells are shown and fitted to a linear model to extract the cell cortex tension. The top panel shows the residuals of the fit. (**c**) Cortex tension in control and ILK cKO islet cells in the presence or absence of blebbistatin (a myosin II inhibitor) or Y27632 (a ROCK inhibitor). *N* = 35-74 islet cells derived from *N* = 5-7 islets were tested for each condition. Note that two values with 921 and 1509 were above 500 μN m^{-1} and are depicted above the grey line. The green lines indicate average values. (**d**) Cortex tension in MIN6 cells treated with either a control or two *Ilk* siRNAs, with and without blebbistatin treatment before the measurement. *N* = 35-68 cells were tested per experimental condition. (**e**, **f**) Schematic overview of pancreatic beta cells and a blood capillary in a pancreatic islet. In a control background (**e**) pancreatic beta cells surround the blood capillary. The cortex is composed of F-actin filaments (orange) and non-muscular myosin II (green). *Ilk*-deficient beta cells (**f**) display an elevated cortex tension due to an enhanced ROCK-dependent actomyosin contraction. As a result of their increased cell cortex tension and decreased cell adhesion, the endocrine cells segregate from vascular endothelial cells, and the pancreatic islet becomes avascular despite unchanged levels of VEGF-A expression and secretion. Data are shown as mean values ± s.d., **P* > 0.05 in a two-way ANOVA followed by Tukey's multiple comparison test. Due to deviations from normality two sensitivity analyses (a quantile regression model for the median and robust regression model) were performed following the idea of Huber's M-estimation. Results were essentially unchanged in comparison to the parametric models.

5.2.3 Discussion

Our results support the hypothesis that limiting the contractile forces of the cell cortex is an integral part of epithelial cell adhesion to blood capillaries. Mechanistically, we propose that ILK reduces these forces in endocrine pancreatic cells by inhibiting non-muscle myosin II, via inhibition of ROCK, to facilitate their adhesion to blood vessels and thus enable pancreatic islet vascularization (Figure 11e). Notably, previous studies have shown that ILK regulates myosin II via various molecular mechanisms, including RhoA/ROCK and calcium regulatory protein sarcoplasmic/endoplasmic reticulum Ca^{2+} ATPase isoform-2a (SERCA-2a) and phospholamban[152, 239]. While our study does not exclude a role for soluble angiogenic factors in ILK cKO islets (Figure 11e), our observations strongly favor the interpretation that the altered biomechanical properties of the endocrine tissue prompted the observed vascular phenotype (Figure 11f). As shown, vascular endothelial cell number, proliferation and apoptosis are unchanged in ILK cKO pancreatic islets, contrary to what would be predicted during either upregulation or downregulation of growth factor receptor signaling; likewise, the unchanged expression and secretion of VEGF-A, the presence of endothelial fenestration and vascular basement membrane, and absence of 'empty sleeves' of vascular basement membrane oppose the established phenotypic response to changes in angiogenic factors[106, 240, 241] (Figure 11e, f).

To date, from embryonic development to tumorigenesis, studies on tissue neovascularization have largely focused on the cellular and molecular components of the vasculature and its growth factors. However, our results motivate future pro- and antiangiogenic studies to therapeutically target the epithelial cell mechanics of a tissue. For further consideration, after development, the biomechanical stiffness of several tissues inversely correlates with their microvascular densities (for example, compare brain and skeletal muscle)[242]; similarly, the metastatic potential of certain human cancer cells inversely correlates with both their mechanical stiffness and actomyosin contraction[238, 243]. By stepping away from a pure endothelial-centric perspective, future studies might leverage the biomechanical properties of growing or hypertrophic tissues to inhibit or promote vascularization.

5.2.4 Methods

5.2.4.1 Mouse models

Ilk$^{loxP/loxP}$, *Ins1*(*Cre*) knock-in, and *Pdx1-Cre* mice were previously described[137, 198, 244]. *Ilk*$^{loxP/loxP}$ mice were crossed with *Pdx1-Cre* mice to obtain *Pdx1-Cre* x *Ilk*$^{loxP/wt}$ (control) and *Pdx1-Cre* x *Ilk*$^{loxP/loxP}$ (ILK cKO) mice on C57BL/6 background. Alternatively, they were crossed with *Ins1(Cre)* knock-in mice to obtain beta cell specific ILK cKO mice. For beta cell mass analysis *Cre*-negative x *Ilk*$^{loxP/loxP}$ mice were used as control. All experiments were performed with either 1-day-old, 7-day-old, 14-day-old male/female mice or adult (8–20-weeks-old) male mice. All mice were taken from the local animal facility (Zentrale Einrichtung für Tierforschung und Tierschutzaufgaben, Medical Research School Düsseldorf), where they were kept in individual cages in a room controlled for temperature (22 °C), humidity (55%) and lighting (lights on from 6:00 hours to 18:00 hours.). Mice were fed with standard laboratory chow and water *ad libitum*. All animal experiments were approved by the local Animal Ethics Committee of the Landesamt für Natur, Umwelt und Verbraucherschutz Nordrhein-Westfalen (LANUV North-Rhine-Westphalia, Germany).

5.2.4.2 Glucose tolerance test and plasma insulin concentrations

Glucose tolerance tests were performed on male mice after overnight fasting (16 h). Glucose was intraperitoneally (i.p.) injected at a concentration of 1 mg g^{-1} body weight, and blood glucose concentrations were measured before and 15, 30, 60, 90 and 120 min after glucose administration. Measurements were taken twice at each point of time using a Monometer Futura Glucometer (MedNet GmbH). Plasma insulin concentrations were measured before and 30 or 120 min after glucose injections using an ultra-sensitive rat insulin ELISA (Crystal Chem) in combination with an Infinite M200 NanoQuant reader (Tecan). No method of randomization was used. However, the animals of each group were chosen and placed in random order by the animal house staff. Investigators were not blinded.

5.2.4.3 Insulin tolerance test

Insulin tolerance tests were performed on male mice after fasting (6 h). For testing insulin tolerance, 0.75 IU insulin (Berlinsulin H Normal, Berlin Chemie AG) was i.p. injected per kg body weight. Glucose concentrations were measured before and 15, 30, 60 and 90 min after insulin injection. No method of randomization was used. However, the animals of each group were chosen and placed in random order by the animal house staff. Investigators were not blinded.

5.2.4.4 Isolation of mouse pancreatic islets

Isolation of islets from control and ILK cKO mice was performed according to a previously described protocol[245]. Briefly, Liberase TL Research Grade (Roche) was injected into P7, P14 or adult (8–20-week-old) mouse pancreata via the pancreatic duct. Pancreata were enzymatically digested for 17.5 min, and the reaction was stopped with DMEM (1 g l^{-1} glucose) (PAA Laboratories) supplemented with 15% FBS (Gibco, Life Technologies). After washing and filtering, the islets were separated from the exocrine tissue by gradient centrifugation and collected from the interphase between Histopaque-1077 (Sigma) and DMEM (1 g l^{-1} glucose). The adult islets were washed three times with DMEM supplemented with 15% (v/v) FBS, and cultured in CMRL medium containing 15% (v/v) FBS, 0.15% NaHCO3, 100 U ml^{-1} penicillin, 100 mg ml^{-1} streptomycin, 0.05 mM 2-mercaptoethanol (Gibco, Life Technologies) and 11.5 mM glucose (Sigma-Aldrich).

5.2.4.5 Insulin secretion from mouse pancreatic islets

To determine insulin secretion, pancreatic islets were starved for 1 h in Krebs Ringer HEPES (KRH) buffer (15 mM HEPES, 5 mM KCl, 120 mM NaCl, 2 mM $CaCl_2$, 2 mM $MgCl_2$, 24 mM $NaHCO_3$ and 1 mg ml^{-1} bovine serum albumin) supplemented with either 2 or 2.5 mM glucose. The same islets were first incubated with fresh KRH buffer supplemented with 2 or 2.5 mM glucose (low glucose) for 1 h, followed by a 1 h incubation with KRH buffer supplemented with 5, 10 or 20 mM glucose (high glucose). Subsequently, the islets were lysed in RIPA buffer (50 mM Tris-HCl (pH 7.4), 150 mM NaCl, 1 mM EDTA, 1 mM Na_3VO_4, 1 mM NaF, 0.25% Na-deoxycholate, 1% IGEPAL) to measure total insulin concentrations. Secreted and total insulin were measured using an ultrasensitive rat insulin ELISA (Crystal Chem) in combination with an Infinite M200 NanoQuant reader (Tecan). Secreted insulin was normalized to total insulin levels and presented as a percentage of insulin secretion at either 2.5 or 5 mM glucose.

For measurement of islet insulin content, total islet insulin content was normalized to total protein content which was measured by the bicinchoninic acid method (Thermo Scientific).

5.2.4.6 Immunostaining and imaging

The whole pancreas was removed from mice, fixed in 4% paraformaldehyde and cryopreserved in 30% sucrose, embedded in Tissue-Tek optimum cutting temperature medium (Sakura). Twelve micrometer thick cryosections were made using a Microm HM560 Cryostat (Thermo Fisher). The following antibodies were used: polyclonal guinea pig anti-insulin 50 mg ml^{-1} (A0564, Dako), polyclonal rat anti-CD31 0.31 mg ml^{-1} (550274, BD Pharmingen), polyclonal rabbit anti-PH3 5 mg ml^{-1} (06-570, Millipore), monoclonal rabbit anti-cleaved

caspase-3 1:200 (9664, Cell Signaling Technology), polyclonal rabbit anti-collagen IV 5 mg ml^{-1} (AB 756 P, Millipore), polyclonal rabbit anti-laminin 2.5 mg ml^{-1} (L9393, Sigma), polyclonal rabbit anti-fibronectin 5 mg ml^{-1} (AB2033, Millipore), polyclonal goat anti-VEGF 10 mg ml^{-1} (AF-493-SP, R&D), normal goat IgG 10 mg ml^{-1} (sc-2028, Santa Cruz), polyclonal rabbit anti-NG2 5 mg ml^{-1} (AB 5320, Millipore), donkey anti-guinea pig conjugated with Cy3 7.5 mg ml^{-1} (706-165-148, Jackson ImmunoResearch), donkey anti-rat conjugated with Alexa Fluor 488 10 mg ml^{-1} (A21208, Life Technologies), donkey anti-rat conjugated with Cy5 7.5 mg ml^{-1} (712-175-153, Jackson ImmunoResearch) and donkey anti- rabbit conjugated with Cy5 mg ml^{-1} (711-175-152, Jackson ImmunoResearch). Cell nuclei were stained using 4,6-diamidino-2-phenylindole (DAPI). Images were taken using laser scanning microscopy (LSM 710) coupled to an Axio Observer.Z1 microscope and the Zen 2010 software (Carl Zeiss MicroImaging GmbH). For blood vessel density analyses in adult mice, 8–10 islets from at least three different pancreatic sections were picked per animal. $Insulin^+$ and $CD31^+$ cells were counted with the help of Fiji (ImageJ) image analysis software[189]. The numbers of intra-islet and peri-islet $CD31^+$ cells were normalized to the numbers of $insulin^+$ cells per islet. For blood vessel densities in 1, 7 and 14 (P1, P7, P14) days old mice, pancreatic sections were taken in defined distances of 300 mm (P1, P7) or 600 mm (P14) resulting in at least four sections on one slide and representing 4% (P1, P7) or 2% (P14) of the dorsal and ventral pancreas. From these sections, the total number of islets (28–114 islets per animal, clusters of 10 or more $insulin^+$ cells were considered as islets) was analyzed for blood vessel densities, endothelial cell proliferation, beta cell proliferation and average beta cell numbers. $Insulin^+$, $CD31^+$ and $PH3^+$ cells were counted with the help of Fiji image analyses software. $CD31^+$ cells were normalized to $insulin^+$ cells in islets (blood vessel densities), $PH3^+$, $CD31^+$ cells were normalized to the total numbers of intra- or peri-islet $CD31^+$ cells (endothelial cell proliferation), and $PH3^+$, $insulin^+$ cells were normalized to the total numbers of $insulin^+$ cells (beta cell proliferation). For analyzing endothelial cell apoptosis, the total number of islets of approximately four sections per pancreas was analyzed for cleaved $caspase\text{-}3^+$, $CD31^+$ cells. For intra-islet collagen IV area analyses, 8–10 islets from at least three different sections were analyzed per animal. $Insulin^+$ area was determined manually, $CD31^+$ and collagen IV^+ area were determined based on a threshold method using Fiji image analyses software. The $CD31^+$ and collagen IV^+ area was normalized to the $insulin^+$ area.

For the analysis of beta cell mass, the insulin positive area was determined by applying Li thresholding using Fiji image analysis software. Total pancreatic area was determined manually on the basis of DAPI staining. Total beta cell mass was calculated by the multiplication of the pancreas weight with the ratio of insulin to total pancreatic area. For image analyses, investigators were blinded to treatments and genotypes.

5.2.4.7 Islet adhesion to matrices

Fourteen millimeter microwells of glass bottom culture dishes (MatTek Corporation) were either incubated with growth factor-deprived matrigel, fibronectin or collagen IV (all BD Bioscience) at a concentration of 5 mg cm^{-2} (fibronectin and collagen IV), or at a 1:100 dilution in a total volume of 200 ml (matrigel). Glass bottom dishes were incubated for at least 1 h at 4 °C and washed several times before control and ILK cKO islets were plated in their normal culture medium. The islets were cultured for 7 days before attachment and spreading was assessed. Subsequently, islets were fixed in 4% paraformaldehyde for 1 day at 4 °C and stained for F-actin using phalloidin, fluorescently labelled with Alexa Fluor 488 (Invitrogen, A12379) at a 1:50 dilution.

5.2.4.8 Cell viability in control and ILK cKO islets

Cell viability was determined using the LIVE-DEAD Viability-Cytotoxicity Kit (Life Technologies). Control and ILK cKO islets were isolated and cultured in CMRL islet medium as described above. After 2 days of culture, whole islets were stained with 2 mM calcein, 4 mM ethidium homodimer-1 and Hoechst (1:1000) in KRH buffer containing 2 mM glucose as described above. The islets were incubated for 30 min in the dark at 5% CO_2 and 37 °C in a humidified chamber. Using an LSM 710 coupled to an Axio Observer.Z1 microscope (Carl Zeiss MicroImaging GmbH) equipped with a Plan-Apochromat 20 x /0.8 objective, LSM images were acquired as maximum intensity projections.

5.2.4.9 Cell culture

The immortalized mouse cell line MIN6 shows many characteristics of differentiated beta cells, like insulin production and insulin secretion upon glucose stimulation[222]. MIN6 cells were cultured at 5% CO_2 and 37 °C in a humidified chamber in DMEM supplemented with sodium pyruvate, glutamine and 4.5 g l^{-1}glucose (Gibco, Life Technologies), containing 15% heat-inactivated FBS, 0.34% sodium bicarbonate, 100 U ml^{-1} penicillin, 100 mg ml^{-1} streptomycin and 50 mM 2-mercaptoethanol (Gibco, Life Technologies). They were split when a confluency of 80–90% was reached and used for experiments at passages 20–45.

Ms1 cells were cultured at 5% CO_2 and 37 °C in a humidified chamber in DMEM supplemented with 1 g l^{-1} glucose (American Type Culture Collection), 5% FBS, 100 U ml^{-1} penicillin and 100 mg ml^{-1} streptomycin. They were split at 80–90% confluency and used for experiments at passages 4–48. All cell lines were regularly tested for mycoplasma infection using Mycoplasmacheck (GATC Biotech AG).

5.2.4.10 siRNA transfection

For each siRNA transfection, a confluent T75 flask (Sarstedt) of MIN6 cells was electroporated using an Amaxa biosystems nucleofector II and an Amaxa cell line nucleofection kit (Lonza, VCA-1003). For *Ilk* knockdown, two different stealth siRNAs (ILKMSS205468, ILKRSS301330, Invitrogen) directed against two different regions of the *Ilk* mRNA were used at a final concentration of 800 nM for knockdown experiments. A stealth siRNA negative control medium-GC was used as negative control. For *Itgb1* knockdown, two different siRNAs (5´-CCACAGAAGUUUACAUUAA-3´ sense, 5´-UUAAUGUAAACUUCUGUGG-3´ antisense; 5´-CGGAUUUGAUGAAUGAAAU-3´ sense, 5´-AUUUCAUUCAUCA AAUCCG-3´ antisense, Eurogentec) directed against two different regions of the *Itgb1* mRNA were used at a final concentration of 800 nM for knockdown experiments. An siRNA with equivalent GC content was used as control. The knockdown efficiency was confirmed 72 h post transfection using real-time reverse transcription (RT)–PCR, and experiments were performed at that time point.

5.2.4.11 Adhesion measurements

Cell adhesion measurements were conducted with an AFM (CellHesion II, JPK Instruments) mounted on an inverted fluorescence microscope (Zeiss Axiovert 200, equipped with 20 x objective) used in closed height feedback mode[218]. Differential interference contrast imaging was used to monitor cellular morphology, and fluorescence imaging used to select cells transfected with siRNA constructs during adhesion measurements. Each tipless AFM cantilever (NPO-010, Bruker) was calibrated three times using the thermal noise to eliminate errors. Spring constants were within 10% of the nominal value (~60 mN m^{-1}). Plasma-activated cantilevers were incubated with 2.5 mg ml^{-1} Concanavalin A (ConA, Sigma) overnight at 4 °C and carefully rinsed in phosphate buffered saline (PBS) before use. All ‘probe’ cells were washed with PBS, detached using 1% (vol) ethylenediaminetetraacetic acid (EDTA, Sigma), and placed into glass bottomed 35 mm diameter petri dishes (WPI Inc.) in the appropriate medium to be picked for SCFS experiments. All SCFS measurements were carried out at 37 °C using the JPK petri dish heater (JPK, Germany) and in 5% CO_2 in air. The gas was first humidified to at least 95% of humidity using a sense silicone membrane (Permselect, Michigan, USA). The humidity level was monitored using a sensor (sensirion, Switzerland). The humidified gas was perfused on the top of the petri dish using the JPK perfusion system (JPK, Germany). The ConA-coated cantilever was gently pressed onto a cell applying a force of ~2 nN for ~3 s. After this, the cantilever was lifted for 2 – 10 min to allow the cell to attach firmly to the cantilever. This ‘probe-cell’ was then moved above a ‘target-cell’ or an extracellular matrix (ECM) protein covalently attached to the substrate. Cell adhesion experiments between probe-cell and functionalized surface or target-cell were performed applying a contact force of ~1 nN, contact times ranging from 1 – 20 s, and ~5 µm s^{-1} approach and retract velocities. The

contact time was varied randomly for a given cell – substrate or cell – cell couple to prevent systematic bias or history effects. Each force – distance (F – D) curve characterizing the adhesion between probe and target was repeated depending on the contact time: 1 s contact time, 5 repetitions; 10 s contact time, 3 repetitions, 20 s being measured twice and 5 min being measured once. A resting time of 30 s was given between recording each force–distance curve. Each probe–cell was used to test several target–cells and different regions within functionalized surfaces with ECM proteins. One force–distance curve was taken with any given probe–cell. Cells were observed continuously during the SCFS experiment to judge whether they were intact and stably associated with the cantilever/substrate. force-distance curves were analyzed using JPK analysis software to extract maximum adhesion force and cell deformation during cell – cell and cell – substrate contact. force–distance curves were pooled and statistically processed as described (see Statistical Analysis).

To alter cell adhesion, cells were treated with 50 mM blebbistatin (Merck Millipore, 203389), 50 mM Y27632 (Merck Millipore, 688001) or 10 mM H1152 (Merck Millipore, 555552) with the exception of islet cells, which were treated with 55 mM blebbistatin or 55 mM Y27632, respectively.

5.2.4.12 Functionalized surfaces

Round glass coverslip of a diameter of 4 mm were coated by electron beam thermal evaporation with a 5 nm thick aluminum layer followed by a 10 nm thick gold layer. Gold coated surface were cleaned with ethanol, dried using a gentle flow of N_2 and cleaned by ultraviolet-ozone for 20 min. Surfaces were then immersed for 14 h in 1 mM of 16-mercaptohexadecanoic acid (5%) and 11-mercapto-1-undecanol (95%) and rinsed in ethanol. The self-assembled monolayers were immersed for 30 min into a 170 mM N-hydroxysuccinimide (NHS, Sigma) and 260 mM 1-ethyl-3-(3-dimethylaminopropyl)-carbodiimide (EDC, Sigma) and rinsed with water. The activated surfaces were then incubated with 200 mg ml^{-1} of ECM (for example, Fibronectin) in PBS for 1 h at 37 °C and rinsed with PBS. Glass coated substrates were then transferred to a petri dish and fixed using a small piece of adhesive tape.

5.2.4.13 Cell-cortex tension measurements

Cortex tension measurements with colloidal force microscopy were carried out as described previously[209]. Briefly, an AFM cantilever was modified with a 5 mm diameter glass bead (Kisker) and coated with heated-inactivated FCS (Invitrogen) to prevent unspecific binding to the target-cell during contact measurement. The colloidal force probe was brought into contact with the cell with a 500 pN contact force at 1 mm s^{-1}. A fit to the cortical shell liquid core model between 125 and 250 pN yielded cortex tension. To alter cortex tension, cells were treated

with 50 mM blebbistatin (Merck Millipore, 203389) or 50 mM Y27632 (Merck Millipore, 688001) with the exception of islet cells, which were treated with 55 mM blebbistatin.

5.2.4.14 RNA isolation and real-time RT-PCR

Total RNA was extracted from MIN6 cells and isolated mouse pancreatic islets using peqGold Trifast (Peqlab). In all, 0.2 mg (islets) or 0.4 mg (MIN6 cells) of purified RNA was reverse transcribed into complementary DNA using Superscript II reverse transcriptase (Invitrogen) with random primers according to the protocol provided by the manufacturer. Real-time RT-PCR was performed using an Mx3000P and the 2 x Brilliant III SYBR Green QPCR Master Mix (Agilent Technologies). Each sample was run in triplicate and analyzed according to the threshold cycle (Ct) method. For normalization, primer sequences complementary to complementary DNA sequences of a-tubulin or Hypoxanthine-guanine-phosphoribosyltransferase (Hprt) were used. Primer sequences are summarized Supplementary Table 2.

5.2.4.15 Western Blot

Pancreatic islets were isolated from control and ILK cKO mice and incubated over night in CMRL medium. On the following day 90 islets were picked in 500 µl CMRL medium and collected by centrifugation at 1000g for 5 min. The islet pellet was lysed in 50 µl ice-cold RIPA buffer supplemented with protease inhibitor (Roche) and phosphatase inhibitor (Roche) and lysis was facilitated using a cell disruptor (Scientific Industries) for 5 min. Finally, the lysate was centrifuged at 15,000g for 10 min and the supernatant was stored at -80 °C.

Islet lysates were run on Mini-PROTEAN TGX Precast Gels (Bio-Rad Laboratories). Gel electrophoresis was performed with the Mini-PROTEAN Tetra Cell system in combination with the Power Pac Basic power supply (Bio-Rad Laboratories). The proteins were blotted with Trans-Blot Turbo Transfer Packs using the Trans-Blot Turbo Transfer System (Bio-Rad Laboratories). The membranes were cut according to the molecular weight of the examined proteins and pieces individually blocked in a blocking solution with 0.5% Tween 20/PBS and 5% BSA for 1 h. Membranes were incubated over night in blocking buffer with primary antibodies rabbit anti-ILK (1:500, 3862 s, Cell Signaling Technologies) or rabbit anti-GAPDH (1:1000, ab9485, Abcam) at 4 °C. Secondary antibodies (donkey anti-rabbit conjugated with horseradish peroxidase) were applied for 1 h at room temperature. Membranes were developed with the Clarity Western ECL substrate (Bio-Rad Laboratories) and imaged with the ChemiDoc XRS Imaging System (Bio-Rad Laboratories).

5.2.4.16 Pimonidazole injection

To monitor hypoxia in the islets, mice were injected with 60 mg kg^{-1} Pimonidazole (Hypoxyprobe Green Kit, Hypoxyprobe, Inc., Burlingston). Pancreas and liver were subsequently embedded in OTC and shock frozen. Staining was performed on 12 µm sections that were fixed in acetone at room temperature for min, subsequently washed in PBS 0.2% Tween and blocked in 2% BSA, 5% donkey serum in 0.2% Tween in PBS for 1 h. Sections were stained with HP-FITC-MAb (detects pimonidazole adducts) over night at 4 °C followed by DAPI nuclear counterstaining. For quantification, islets were imaged using an LSM 710 (Zeiss) and images captured with equal exposure times. Intensities of green fluorescence were quantified using Fiji.

5.2.4.17 VEGF-A secretions assay

Pancreatic islets were isolated from control and ILK cKO mice and incubated overnight in CMRL medium. On the following day 20 islets were transferred into a single well of a 24-well plate and incubated in 800 µl CMRL medium. After 24 h 500 µl medium were collected and centrifuged at 2000 r.p.m. for 10 min. One hundred microlitres supernatant (50 µl duplicates) were used to measure secreted VEGF with the mouse VEGF Quantikine ELISA Kit following the manufacturer's instructions (MMV00, R&D Systems). Subsequently, the islets were lysed in RIPA buffer (50 mM Tris-HCl (pH 7.4), 150 mM NaCl, 1 mM EDTA, 1 mM Na_3VO_4, 1 mM NaF, 0.25% Na-deoxycholate, 1% IGEPAL) to measure total protein concentrations using a BCA assay. Secreted VEGF was normalized to total protein levels and presented as a percentage of VEGF secreted from control islets.

5.2.4.18 Injection of fluorescent tomato lectin

FITC-conjugated lectin from *Lycopersicon esculentum* (tomato lectin) (Sigma) was intravenously (i.v.) injected into the tail vein of a control and an ILK cKO mouse. Five minutes after injection, mice were killed and whole pancreata were isolated and processed for immunostaining as described above.

5.2.4.19 Islet transplantation into the anterior eye chamber

Transplantation of isolated islets into the anterior eye chamber of NOD-Scid immunodeficient mice followed by *in vivo* imaging was performed as previously published[246, 247]. Briefly, 20-30 handpicked overnight-cultured islets were transplanted into the anterior chamber of the anesthetized 7- to 13-week-old male NOD.CB17-Prkdc scid/J recipient mice using a custom made beveled glass cannula. Longitudinal *in vivo* imaging of transplanted islets was performed at indicated post-transplant days using an upright laser-scanning microscope (LSM780 NLO; Zeiss, Germany). The volume of transplanted islets was assessed by detection of 633 nm laser

backscatter. Vessels were visualized by injecting 0.25 mg 500-kDa fluorescein-labelled dextran (Life Technologies) in 100 µl PBS into the tail vein. Fluorescein-labelled dextran was excited by two-photon laser at 910 nm and detected at 493 to 612 nm. Total islet volume and vessel volume were calculated using surface rendering (Imaris 7.6, Bitplane AG, Switzerland).

5.2.4.20 Electron microscopy

Pancreata were fixed for 2 h at room temperature by immersion in 2.5% glutaraldehyde in 0.19 M sodium cacodylate buffer at pH 7.4, postfixed in 1% reduced osmium tetroxide in aqua bidest for 60 min, and subsequently stained with 2% uranyl acetate in maleate buffer, pH 4.7. The specimens were dehydrated in graded ethanols and embedded in epoxy resin[248]. Ultrathin sections were picked up onto Formvarcarbon-coated grids, stained with lead citrate, and viewed in a transmission electron microscope (TEM 910; Zeiss Elektronenmikroskopie, Oberkochen, Germany).

5.2.4.21 Statistical analyses

Throughout the paper, quantifications are shown as means ± standard deviations (s.d.). Statistical significance was determined as indicated in the respective figure legends and differences were considered significant with a *P* value < 0.05. Normality was visually evaluated (dot plot and Q-Q plots) in addition to the Shapiro–Wilk-test using R and Graphpad Prism.

A two-sided, unpaired Student's t-test correcting for unequal variances was used for comparison between two groups. For comparisons of more than two groups, one-way ANOVA or two-way ANOVAs were performed. In addition, Dunnett's or Tukey's multiple comparison test were performed using GraphPad Prism (GraphPad Software). To validate the parametric ANOVA analysis in Figure 11, a two-way ANOVA with interaction using a quantile regression model for the median (SAS, PROC QUANTREG) and additionally using a robust regression model following the idea of Huber's M-estimation (SAS, PROC ROBUSTREG) was used. In all cases, statistical significance were considered with *P* value < 0.05. Most sample sizes were chosen based on data shown in previous publications.

5.2.5 Additional information

5.2.5.1 Supplementary Information

Supplementary Information accompanies this manuscript are presented in section 9.2 or at http://www.nature.com/naturecommunications

5.2.5.2 Data availability

All relevant data are included in the manuscript or its supplementary information and available from the authors upon request.

5.2.5.3 Acknowledgements

We are grateful to S. Jakob for technical support, A. Leinweber for animal care, and M. Kelly-Goss for proof-reading the manuscript, and Dr Miyazaki for providing us with MIN6 cells. The work was funded by the Competence Network Diabetes mellitus (KKNDm) and Federal Ministry for Research and Education (BMBF; 01GI1103A), the Emmy Noether program of the German Research Foundation (DFG), the German Center for Diabetes Research (DZD e.V.), the Anton-Betz-Stiftung der Rheinischen Post e.V. as well as the German Diabetes Center (DDZ), the Federal Ministry of Health, the Ministry for Innovation, Science and Research of North Rhine-Westphalia. R.S. and D.J.M. were supported by the Swiss National Science Foundation (SNF; grant 31003A_138063 to D.J.M.) and the European Molecular Biology Organization (EMBO) (ALTF 265-2013 to D.A.).

5.2.5.4 Competing financial interests

The authors declare no competing financial interests.

5.2.5.5 Authors and author details

M. Kragl[1,2,3]*, R. Schubert[4]*, H. Karsjens[1,2,3]*, S. Otter[1], B. Bartosinska[1,2,3], K. Jeruschke[2,5], J. Weiss[2,5], C. Chen[2,6,7], D. Alsteens[4], O. Kuss[2,8], S. Speier[2,6,7], D. Eberhard[1], D. Müller[4] & E. Lammert[1,2,3]

[1]Institute of Metabolic Physiology, Department of Biology, Heinrich Heine University, D-40225 Düsseldorf, Germany. [2]German Center for Diabetes Research (DZD e.V.), D-85764 München-Neuherberg, Germany. [3]Institute for Beta Cell Biology, German Diabetes Center, Leibniz Center for Diabetes Research at Heinrich Heine University, D-40225 Düsseldorf, Germany. [4]Eidgenössische Technische Hochschule Zürich, Department of Biosystems Science and Engineering, CH-4058 Basel, Switzerland. [5]Institute for Clinical Biochemistry and Pathobiochemistry, German Diabetes Center, Leibniz Center for Diabetes Research at Heinrich Heine University, D-40225 Düsseldorf, Germany. [6]Paul Langerhans Institute Dresden (PLID) of Helmholtz Center Munich at the University Clinic Carl Gustav Carus of Technische Universität Dresden, Helmholtz Zentrum München, D-85764 Neuherberg, Germany. [7]DFG-Center for Regenerative Therapies Dresden (CRTD), Faculty of Medicine, Technische Universität Dresden, D-01307 Dresden, Germany. [8]Institute for Biometrics and Epidemiology, German Diabetes Center, Leibniz Center for Diabetes Research at Heinrich Heine University, D-40225 Düsseldorf, Germany.
* These authors contributed equally to this work.

5.2.5.6 Author contribution

See section 5.2.6 “Personal contribution and general information”

5.2.5.7 Reprints and permission

Information is available online at http://npg.nature.com/reprintsandpermissions/

5.2.5.8 Publisher's note

Springer Nature remains neutral with regard to jurisdictional claims in published maps and institutional affiliations.

5.2.6 Personal contribution and general information

Personal contribution of Haiko Karsjens (**H.K.**) to the manuscript "The biomechanical properties of an epithelial tissue determine the location of its vasculature" published in Nature Communications in 2016. Contrary to the online version of this article, the numbering of the figures and citations was changed in order to achieve consistency within this thesis and *P*-values have been incorporated into the figures.

Name of the journal:	Nature Communication
Impact factor (2016):	12.12
Author position:	Third author, equal contribution to first authorship
Tasks:	Performance and analysis of experiments, planning of the project, preparation of figures, preparation and correction of the manuscript, preparation of supplementary and source data files, statistical analyses, coordination of collaborations.

Author`s contribution (as written in the manuscript):

M.K., D.E., **H.K.** and E.L. conceptually designed this study. M.K. and, to some extent D.E., **H.K.** and S.O. performed mouse *in vivo* experiments. M.K., **H.K.**, S.O., B.B. and D.E. isolated pancreatic islets and performed experiments on them, and conducted immunohistochemical staining and siRNA knockdown in MIN6 cells. R.S. designed, performed and evaluated AFM experiments with the help of D.A. and the supervision of D.J.M., C.C. performed islet transplantation experiments into the anterior eye chamber and *in vivo* imaging and was supervised by S.S., K.J. and J.W. performed electron microscopy. M.K., R.S., **H.K.**, D.E. and E.L. interpreted data. O.K. performed parts of the statistical analysis. M.K., **H.K.** and E.L. wrote the manuscript, and all authors read and commented on the final manuscript text.

Contribution in detail:

Haiko Karsjens performed the experiments for the following figures: Figure 8e, f; Figure 9b-e as well as supplementary (sup.) Figure 1b, g; sup. Figure 3; sup. Figure 5; sup. Figure 7; sup. Figure 8; sup. Figure 10a, sup. Figure 11a, sup. Figure 12a; sup. Table 1.

Haiko Karsjens contributed to the results leading to Figure 9g.

Haiko Karsjens was the leading coordinator for the collaboration resulting in figures: Figure 8d; sup. Figure 10b, c; sup. Figure 11b, c; sup. Figure 12b, c.

Haiko Karsjens and Martin Kragl were the leading coordinators for the collaboration resulting in: Figure 10; Figure 11.

In sum, Haiko Karsjens contributed to the work of this manuscript with approximately 30%.

5.3 Integrin-Linked kinase supports beta cell proliferation during insulin resistance

This paragraph contains unpublished experiments that continue the work presented in the previous paragraph (5.2) and are published in Kragl et al.[2]. The following results underline the role of ILK as well as the intra-islet vasculature for beta cell proliferation and insulin secretion during insulin resistance.

5.3.1 Background

Insulin resistance is characterized by chronic hyperglycemia and hyperinsulinemia and is a prominent risk factor for the development of Type 2 diabetes mellitus (T2D)[44]. In the beginning, beta cells can compensate the increased metabolic demands by increasing their insulin output, either by an increased synthesis and secretion of insulin and/or by expanding the functional beta cell mass[51, 52]. Several growth factors and hormones are known that promote beta cell proliferation during insulin resistance (e.g. adipokines)[62]. However, the exact mechanisms that induce beta cell proliferation are still unclear and require further investigation. Beta cells highly proliferate during fetal and newborn stages, and reach their maximum beta cell mass in early adulthood; from here, beta cells barely proliferate[249]. During development, beta cell proliferation is promoted by factors that are provided by the capillaries, which form the dense vascular network of pancreatic islets[95]. How the vascular network controls beta cell proliferation during beta cell compensation is not known yet and a better understanding of the mechanisms can lead to the identification of new therapeutic targets, which trigger beta cell proliferation and thus halt the progression from insulin resistance to T2D[250, 251].

To address the gaps of understanding, we investigated the role of the integrin-linked kinase (ILK) and the intra-islet vasculature in mice that experience acute insulin resistance. ILK is a key downstream adaptor protein of β1 integrin signaling and mediates several signaling pathways that control essential cellular functions like cytoskeletal dynamics or cell adhesions[132]. Depending on the tissue, ILK can either promote or inhibit cell proliferation[153, 206]. In the pancreatic epithelium, ILK has no impact on beta cell proliferation, but controls islet vascularization and first phase insulin secretion, as *Ilk* knockout mice display an avascular pancreatic islet core as well as a delayed insulin secretion[2]. Studies showed that the islet vasculature is crucial for normal beta cell function as well as insulin secretion and adapts to the increased metabolic demands during insulin resistance[91, 94, 110].

Here, we specifically deleted *Ilk* in beta cells in order to diminish blood vessels from the islet core, and treated these mice with the insulin receptor antagonist S961. S961 completely inhibits insulin action *in vitro* and *in vivo*, leading to acute hyperglycemia and insulin resistance in rodents[252]. We found that *Ilk* knockout mice treated with S961 experienced insulin

resistance, including chronic hyperglycemia and hyperinsulinemia. A beta cell-specific *Ilk* knockout led to fewer blood vessels in the islet core under standard as well as insulin resistance conditions. *Ilk*-deficient beta cells and/or the absence of the intra-islet vasculature caused lower blood plasma insulin concentrations during a glucose tolerance test (GTT) and a decreased beta cell proliferation during chronic hyperglycemia. The obtained results favor the idea that *Ilk* in beta cells determines the localization of islet vasculature and positively influences beta cell proliferation as well as insulin secretion during insulin resistance.

5.3.2 Results

5.3.2.1 Insulin antagonist S961 induces hyperglycemia and hyperinsulinemia *in vivo*

To gain more insights into the role of *Ilk* for beta cell biology and maintenance of glucose homeostasis, we induced acute metabolic stress in beta cell-specific *Ilk* knockout mice. Specifically, $Ins1^{Cre}; Ilk^{fl/fl}$ (referred to ILK bKO hereafter) and heterozygous $Ins1^{Cre}; Ilk^{fl/+}$ mice (referred to control hereafter) were challenged with the insulin receptor antagonist S961. Several studies showed that S961 induces the main characteristics of insulin resistance, namely hyperglycemia and hyperinsulinemia, in rodents[252, 253]. Either PBS or S961 (20nM) were loaded into osmotic Alzet pumps and afterwards subcutaneously implanted into six control (referred to as PBS-control or S961-control) and six ILK bKO (referred to as PBS-ILK bKO or S961-ILK bKO) mice, respectively (Figure 12a). Isolated islets of ILK bKO mice showed a 50% reduction of *Ilk* mRNA compared to control islets (Figure 12b). Correct pump insertion as well as positive action of S961 were verified by analysis of random blood glucose levels. Both, control and ILK bKO mice became hyperglycemic 24 hours after S961-filled pump implantation, and remained so for the next 14 days (Figure 12c, d). In contrast, mice with PBS-filled pumps showed no change in random blood glucose levels (Figure 12c, d). No difference in blood glucose levels or bodyweights between control and ILK bKO mice were observed (Figure 12c, d; Supplementary Figure 13).

Besides chronic hyperglycemia, elevated plasma insulin levels (hyperinsulinemia) are a prominent consequence of insulin resistance[51, 58]. Analysis of random plasma insulin levels revealed that S961-treated mice displayed around 20 times higher random plasma insulin concentrations compared to PBS-treated mice, complementing the characteristics of an insulin resistance phenotype (Figure 12e). Furthermore, S961-ILK bKO mice displayed slightly but non-significantly increased insulin concentrations compared to S961-controls (Figure 12e). Besides disturbed insulin secretion, also alterations in glucagon secretion of alpha cells during insulin resistance have been discribed[66]. We identified that plasma glucagon concentrations of S961-treated mice are slightly but non-significantly increased compared to PBS-treated mice (Figure 12f). No changes between the genotypes were observed (Figure 12f). These data suggest that S961 induced insulin resistance in both, control and in ILK bKO mice.

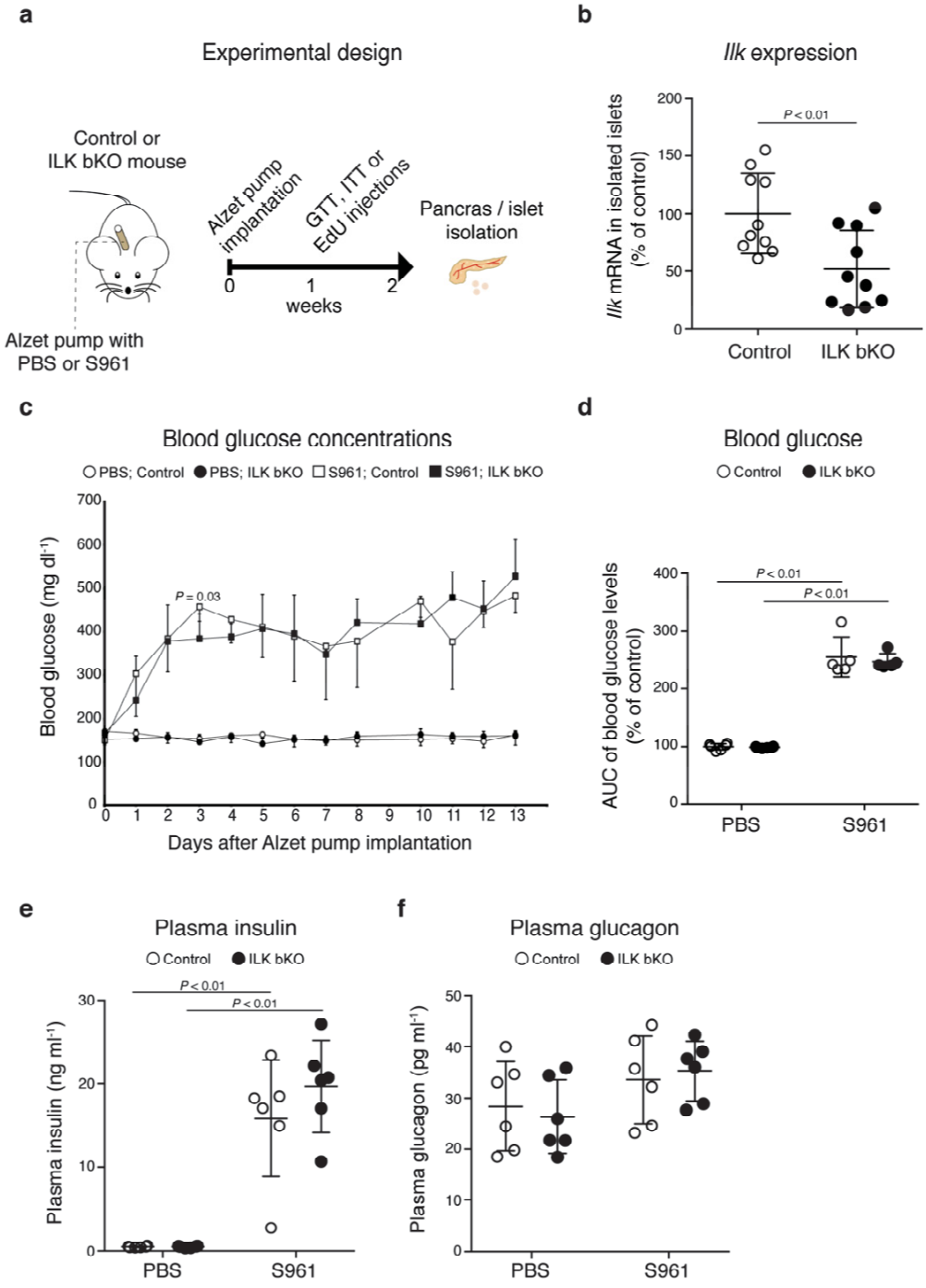

Figure 12: ***Experimental design and characterization of S961-treated mice.*** (**a**) Experimental design: Alzet pumps loaded with PBS or S961 (20 nM) were implanted in control and ILK bKO mice. Subsequently either a GTT and ITT or EdU injections were performed. After 14 days pancreatic islets or pancreas were isolated for further analysis. (**b**) Quantification of relative *Ilk* mRNA expression in control versus ILK bKO islets (n = 10 animals per experimental group). (**c**) Random blood glucose levels of control versus ILK bKO mice from 0 to 13 days after Alzet pump implantation ($n \geq 5$ mice per experimental group). (**d**) Area under the curve of data shown in **c**. (**e**, **f**) Random plasma insulin (**e**) or random plasma glucagon (**f**) concentrations of PBS-control, PBS-ILK bKO versus S961-control and S961-ILK bKO mice (n = 6 mice per experimental group). All values are shown as means ± SD; statistical significance (*P < 0.05) was determined by unpaired two-tailed Student's t-test (**b**, **c**) and by two-way ANOVA followed by Tukey's multiple comparisons test (**d**, **e**, **f**).

5.3.2.2 ILK bKO mice display reduction of intra-islet capillaries

Based on previous results obtained from Pdx1^{Cre}; *Ilk*$^{fl/fl}$ mice (see section 5.2) we investigated how the vasculature of pancreatic islets adapts in the setting of an insulin resistance together with a beta cell-specific *Ilk* knockout. Therefore, the endothelial cells (ECs) and beta cells of control and ILK bKO mice treated with either PBS or S961 were immunohistochemically labeled by the platelet endothelial cell adhesion molecule 1 (Pecam1/ CD31) and insulin, respectively. We observed that a beta cell-specific *Ilk* knockout caused a similar vascular phenotype like an *Ilk* knockout in the pancreatic epithelium (compare Figure 7e and 13a). Knockout of *Ilk* in both PBS- and S961-treated mice caused significant fewer intra-islet and by tendency more peri-islet ECs compared to their respective controls (Figure 13b, c). The total number of islet ECs was not changed regardless of the treatment or genotype (Figure 13d). Noteworthy, an insulin resistance condition did not lead to changes in the blood vessel localization within pancreatic islets (Figure 13a-d).

Since recent studies showed that insulin resistance and chronic hyperglycemia induce alterations of the islet vasculature, we analyzed the morphology of blood vessels in mice with S961-induced insulin resistance[110, 111]. In control mice, S961 treatment induced twice as big blood vessels compared to PBS treatment (Figure 13e). ILK bKO mice showed an increased blood vessel size after S961 treatment as well, but since already an *Ilk* knockout alone led to an increased blood vessel size, the difference between PBS- and S961-treated ILK bKO mice was not significant (Figure 13e). Furthermore, the blood vessel diameter of S961- compared to PBS-treated mice was increased by 10-20% (Figure 13f). Again, a beta cell-specific *Ilk* knockout alone led to a significant larger blood vessel diameter compared to control mice (Figure 13f). Interestingly, despite an increased average blood vessel area and blood vessel diameter in S961-treated mice, the blood vessel coverage was not changed compared to PBS-treated mice (Figure 13g). Just S961-ILK bKO mice showed by tendency a lower blood vessel coverage compared to S961-control and PBS-ILK bKO mice (Figure 13g).

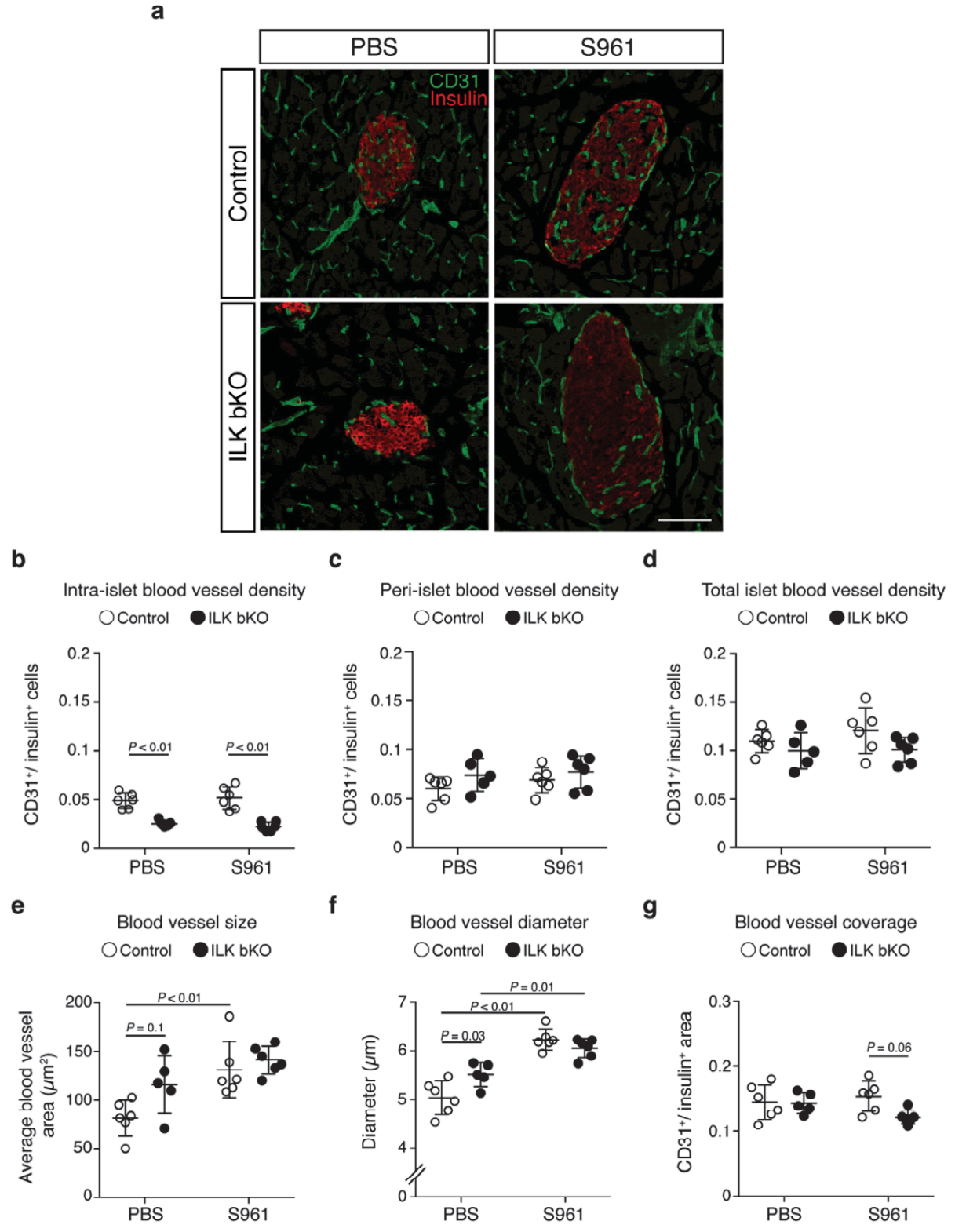

Figure 13: ***ILK in beta cells is required for the localization of the intra-islet vasculature; insulin resistance induces changes in vessel morphology.*** (**a**) Representative immunofluorescence images of pancreatic sections stained for insulin (red, pancreatic islets) and CD31 (green, blood vessels). (**b**-**d**) Quantification of in the intra-islet (**b**), peri-islet (**c**) or total islet (**d**) blood vessel density. (**e**-**g**) Quantification of blood vessel size (**e**)**,** blood vessel diameter (**f**) and blood vessel coverage (**g**)**.** *N* ≥ 5 mice per experimental group, 10 islets were analyzed per mice. All values are shown as means ± SD; statistical significance (**P* < 0.05) was determined by two-way ANOVA followed by Tukey's multiple comparisons test. Scale bar, 100 μm.

5.3.2.3 Reduced insulin secretion from ILK bKO mice during a glucose tolerance test

Next, we investigated if S961-treated mice, which show the main hallmarks of insulin resistance and loss of the intra islet vasculature, have the capability to clear glucose from the blood circulatory system. Interestingly, after overnight fasting S961-treated mice displayed massive lowered blood glucose levels: from around 400 mg dl^{-1} blood glucose to under 200 mg dl^{-1} (Figure 12c, 14a). Thereby, these mice are no longer classified as hyperglycemic or diabetic[254]. However, the fasting blood glucose levels of S961-treated mice were still twice as high as PBS-treated mice (Figure 14a). During an intraperitoneal glucose tolerance test, S961-treated mice showed significant impairment in the glucose disposal compared to PBS-treated mice (Figure 14a, b). No difference between control and ILK bKO mice was observed (Figure 14a,b).

Furthermore, we analyzed the insulin secretion of control and ILK bKO mice during a GTT. The plasma insulin concentrations rose simultaneously 30 minutes after intraperitoneal glucose injections in PBS-treated control and ILK bKO mice. In S961-treated mice, overnight fasting caused no change in insulin concentrations in control mice, but ILK bKO mice showed a clear decrease (compare Figure 12e and 14c). However, S961-treated mice still displayed 20-30 times higher fasting plasma insulin concentrations compared to PBS-treated mice. S961-treated mice showed no reaction after intraperitoneal glucose injections and maintained their elevated insulin levels. Interestingly, S961-ILK bKO mice showed constant and significant 2-3 times lower plasma insulin values compared to S961-control mice (Figure 14c, d).

To examine the difference of insulin concentrations during the GTT between S961-control and S961-ILK bKO mice, we subsequently isolated pancreatic islets and analyzed *in vitro* insulin secretion under low (2.5 mM) and high (20 mM) glucose conditions. Surprisingly, the differences observed *in vivo* were not reproduced *in vitro*. S961-treated control and ILK bKO islets showed a similar *in vitro* insulin secretion (Figure 14e).

Since insulin resistance is characterized by an insufficient response of mainly muscle, fat and liver cells to insulin, we next investigated how the S961-treated mice, which show hallmarks of insulin resistance, respond to insulin. PBS-treated mice displayed an expected reaction to an intraperitoneal insulin injection (Figure 14f). Blood glucose levels decreased 15 minutes after insulin injection and started to slowly rise again 60 minutes after insulin injection. S961-ILK bKO mice showed a mild response to an insulin injection. The glucose concentrations decrease slowly but steadily by around 20% over 90 minutes. In contrast, the S961-control mice showed no reaction after insulin injection, and maintained elevated insulin concentrations over 90 minutes, indicating that these mice were insulin resistant 13 days after Alzet pump implantation (Figure 14f, g).

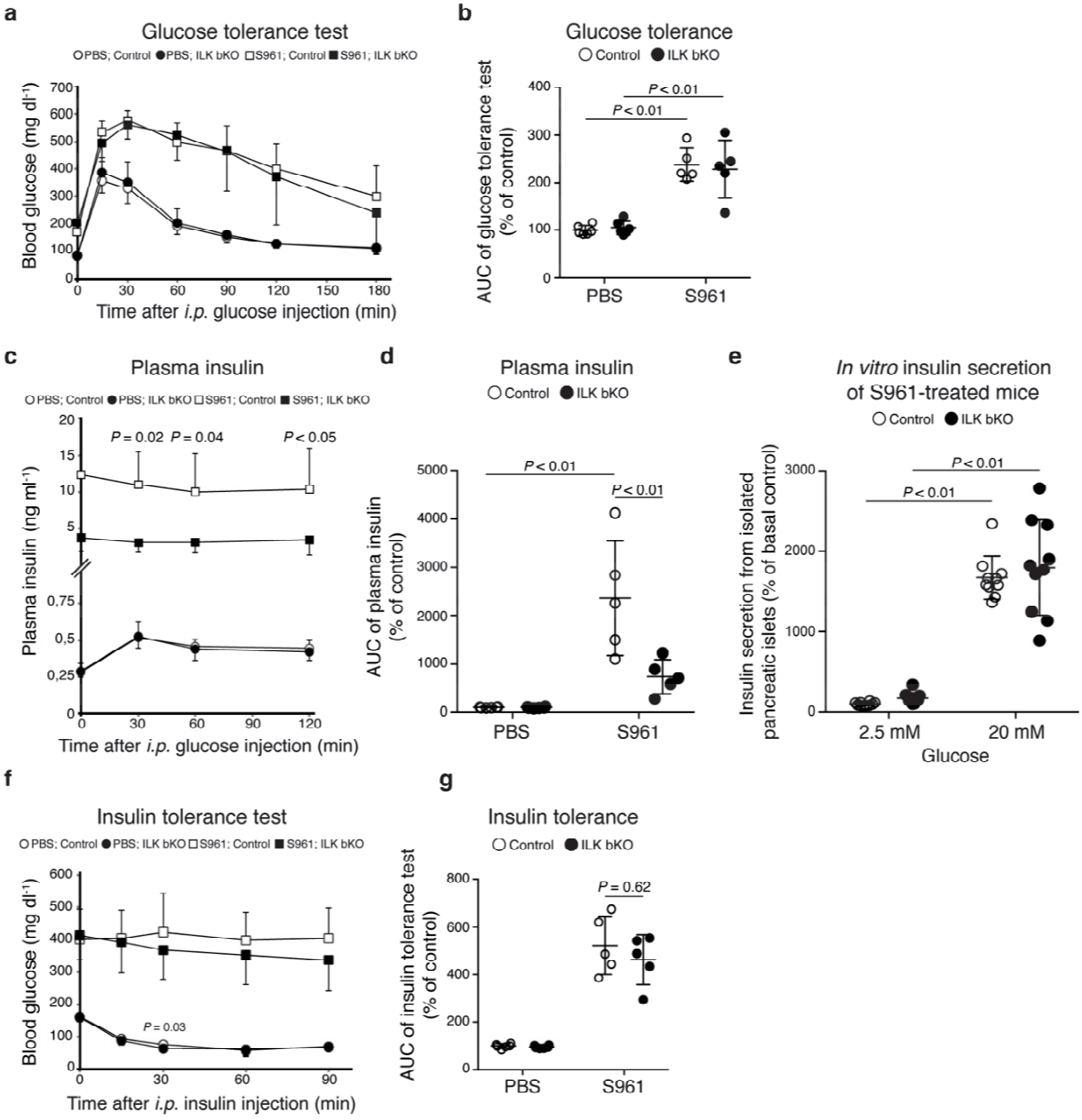

Figure 14: ***Ilk-deficient mice display lower plasma insulin concentrations during a glucose tolerance test.*** (**a**) Blood glucose concentrations of PBS-control, PBS-ILK bKO versus S961-control and S961-ILK bKO mice during an intraperitoneal glucose tolerance test ($n \geq 5$ mice per experimental group). (**b**) Area under curve of data shown in **a**. (**c**) Plasma insulin concentrations during a glucose tolerance test shown in **a**. (**d**) Area under the curve of data shown in **c**. (**e**) Glucose stimulated insulin secretion from isolated pancreatic islets of S961-control and S961-ILK bKO mice incubated at 2.5 mM and 20 mM glucose. Secreted insulin is normalized to total insulin levels ($n = 10$ islet batches per experimental group). (**f**) Blood glucose concentrations of PBS-control, PBS-ILK bKO versus S961-control and S961-ILK bKO mice during an insulin tolerance test ($n \geq 5$ mice per experimental group). (**g**) Area under the curve of data shown in **f**. All values are shown as means ± SD; statistical significance ($^*P < 0.05$) was determined by unpaired two-tailed Student's t-test (**a**, **c**, **f**) and by two-way ANOVA followed by Tukey's multiple comparisons test (**b**, **d**, **e**, **g**).

5.3.2.4 ILK supports beta cell proliferation during insulin resistance

Besides changes in islet vascular morphology, insulin resistance also causes adaptions in beta cell biology. To maintain normoglycemia, beta cells can increase their insulin output as well as their functional beta cell mass via proliferation[51-53, 255]. Here, we analyzed whether a S961 induced insulin resistance triggers beta cell proliferation, and investigated how ILK as well as the intra-islet vasculature influence beta cell proliferation. To visualize proliferating cells, we injected EdU (5-ethynyl-2'-deoxyuridine), a thymidine analog that incorporates into newly synthesized DNA, into control and ILK bKO mice (Figure 15a). As beta cells barely proliferate in the adult[249], almost no proliferating cells were observed in PBS-treated mice (Figure 15a, b). Contrary, S961-treated mice showed numerous EdU-positive nuclei. Analysis revealed that S961-treated mice showed significantly more proliferating cells compared to their respective PBS-treated controls. Interestingly, S961-ILK bKO mice showed significantly fewer proliferating cells compared to S961-control mice, indicating a potential role of ILK or intra-islet blood vessels for beta cell proliferation (Figure 15b).

To confirm this observation, we performed a PH3 (phosphorylated histone H3) staining and verified the results of the EdU staining (Figure 15c; Supplementary Figure 14). Again, PBS-treated mice showed almost no beta cell proliferation and S961-treated mice displayed several proliferating beta cells. Furthermore, S961-ILK bKO mice showed again fewer proliferating beta cells compared to S961-control mice. We also analyzed beta cell apoptosis to exclude that the missing intra-islet vasculature caused beta cell death. Cleaved caspase-3 (CC3) staining revealed that almost no apoptotic cells were present in all experimental groups (Figure 15d; Supplementary Figure 15).

5.3.2.5 Insulin resistance causes an increased islet size – irrespectively of ILK

Our findings suggest that the increased beta cell proliferation in S961-treated mice manifests in bigger pancreatic islet size. We found islets in S961-treated mice to be around twice as big compared to PBS-treated mice (Figure 15e). Interestingly, even though beta cells of S961-ILK bKO mice showed a significant lower proliferation rate compared to S961-control beta cells, no change in islet size between S961-treated mice was observed (Figure 15e).

We then investigated if an increased average beta cell size can explain the discrepancy between a reduced beta cell proliferation and at the same time a similar islet size of S961-ILK bKO compared to S961-control mice. We found that the average islet cell size was increased in S961-treated compared to PBS-treated mice but was not changed within S961-treated mice and could thus not explain the discrepancy (Figure 15f).

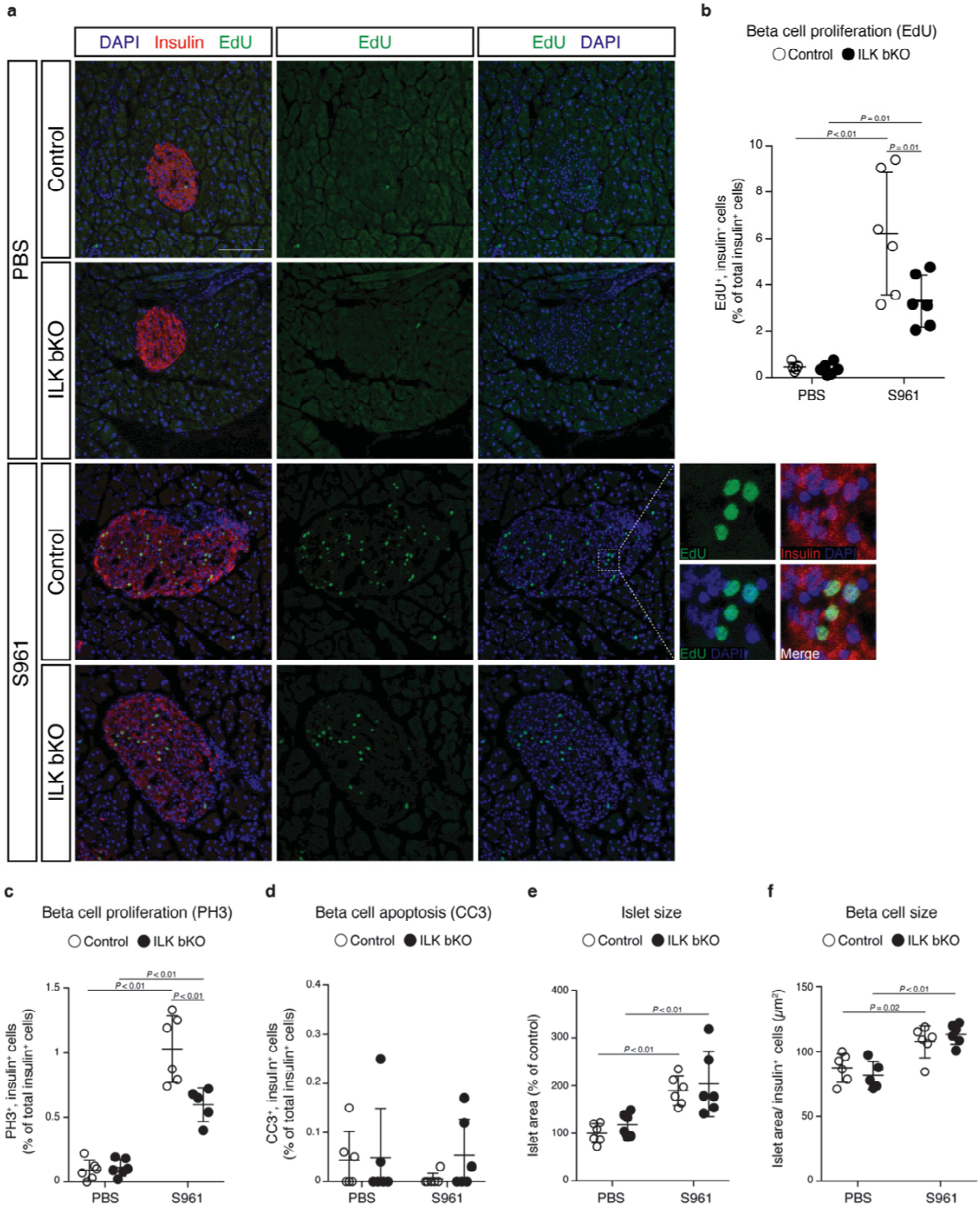

Figure 15: ***ILK in beta cells is supports beta cell proliferation during insulin resistance.*** (**a**) Representative laser scanning microscope images of pancreatic sections co-labelled with insulin (beta cells, red) and EdU (proliferating cells, green). (**b**-**f**) Quantification of proliferating (EdU-positive) beta cells (insulin-positive) (**b**), of proliferating (PH3-positive) beta cells (**c**), of apoptotic (Cleaved caspase-3 (CC3)-positive) beta cells (**d**), of islet size (insulin-positive area) (**e**)**,** and of the average beta cell size (ratio of islet area to number of insulin positive nuclei) (**f**). $N \geq 5$ mice per experimental group, 10 islets were analyzed per mice. All values are shown as means ± SD; statistical significance (*$P < 0.05$) was determined by two-way ANOVA followed by Tukey's multiple comparisons test. Significant outliers were detected by the extreme studentized deviate method (Grubbs' test) and excluded from the statistical analysis (**b**, **c**). Scale bar, 100 μm.

5.3.3 Discussion

The presented results provide more insights into the role of ILK in beta cells, especially during insulin resistance.

The insulin receptor antagonist S961 induced an insulin resistance condition, including chronic elevated blood glucose levels (hyperglycemia) as well as elevated plasma insulin concentrations (hyperinsulinemia) in control and in ILK bKO mice (Figure 12 c-e). S961 binds to the insulin receptor and completely inhibits insulin action, which in turn leads to hyperglycemia[253]. Since the beta cell-specific *Ilk* knockout did not affect the primary target cells of insulin action (liver, fat, muscle cells) our results were expected and are in line with the work of other groups, which challenged rodents with S961[252, 256].

Pancreatic islets with a beta cell-specific *Ilk* knockout displayed a hypovascularized islet core (Figure 13a, b). This observation is a phenocopy of the results obtained with a pancreatic epithelium specific *Ilk* knockout and favor the idea that an *Ilk* deletion in beta cells also led to an increased actomyosin-mediated cortex tension in beta cells and a reduced adhesion between beta cells and ECs that in turn resulted in the hypovascularized islet core (Figure 13a, 7e)[2]. However, the reduction of the intra-islet blood vessel density (28% and 50% reduction, respectively) as well as the accumulation of ECs in the islet periphery in mice with a beta cell specific *Ilk* knockout was not as distinct as compared to mice with a pancreatic epithelium specific *Ilk* knockout (Figure 13b,c & 7e). Furthermore, the knockdown efficiency in isolated pancreatic islets of ILK bKO (*Ins1*^{Cre}) mice was not as high as compared to ILK cKO (*Pdx1*^{Cre}) mice (50% and 75% respectively) (Figure 12b, Supplementary Figure 1a). These differences might be caused by the different promoters driving the Cre recombinase. The ILK bKO (*Ins1*^{Cre}) mice showed a beta cell specific *Ilk* deletion[198], while the ILK cKO (*Pdx1*^{Cre}) mice displayed an *Ilk* knockout in the pancreatic epithelium, which occurs slightly earlier in pancreas development and affects indeed primarily beta cells, but also acinar and other endocrine cells[244, 257, 258]. The reduced cell number affected by the beta cell specific *Ilk* knockout as well as the later developmental *Ilk* inactivation might be the reasons for the reduced knockout efficiency as well as the attenuated vascular phenotype observed in ILK bKO mice compared to ILK cKO mice. Noteworthy, a *Pdx1*^{Cre} and an *Ins1*^{Cre} promoter mediated *Vegf-a* knockout resulted in comparable differences of reduction of the intra-islet vasculature[104]. In contrast to the vascular consequences of an *Ilk* knockout in beta cells, chronic hyperglycemia and hyperinsulinemia induced by S961 treatment did not influence the localization of the islet vasculature (Figure 13a-d).

S961-treated mice displayed alterations in the blood vessel morphology, namely an increased average blood vessel size (+30-40%) as well as an increased blood vessel diameter (+20%) compared to PBS-treated mice (Figure 13e, f). These observations are in line with previous studies of different diabetic mouse models, which also observed enlarged blood

vessels in pancreatic islets[97, 110]. The exact mechanisms of vessel adaptions are still unknown but studies propose beta cell derived signals that either trigger nitric oxide-mediated vasodilation in ECs[110] or act on pericytes that in turn trigger dilation of the intra-islet capillaries[97]. Interestingly, we also observed that a beta cell specific *Ilk* knockout alone caused (besides changes in the intra-islet vessel localization) an increase in the average blood vessel size and a larger blood vessel diameter (Figure 13e, f). Whether ILK in beta cells is part of signaling pathways that regulate intra-islet blood vessel dilation has to be determined. Inactivation of *Ilk* signaling in ECs or disruption of the β1 integrin pathway in EC supporting mural cells leads to bigger capillaries in the retina and embryonic skin, respectively[259, 260]. These results suggest a regulatory role of ILK in other cell types for vessel dilation. Despite an increased vessel area and blood vessel diameter in S961-ILK bKO mice, these mice showed a reduced blood vessel coverage by tendency (Figure 13g). This observation is due to the lack of intra-islet blood vessels (Figure 13a). In contrast, no change of blood vessel coverage was observed in PBS-treated mice, since the *Ilk* knockout alone already triggered an increased vessel area and vessel diameter that neutralized the effect of the hypovascularized islet core (Figure 13e-g).

The insulin resistance phenotype of S961-treated mice caused a reduced glucose tolerance compared to PBS-treated mice (Figure 14a, b). This result is in line with previous studies, which show that the impairment of the insulin signaling pathway leads to a deterioration of insulin-mediated glucose uptake that in turn results in chronic hyperglycemia and hyperinsulinemia[252]. Noteworthy, contrary to our previous obtained results with pancreatic epithelium specific *Ilk* knockout mice[2], a beta cell specific *Ilk* knockout did not lead to significant differences in glucose tolerance (Figure 14a, b). This might be caused by the weaker vascular phenotype, the different promoter driving the Cre recombinase or the weaker knockout efficiency of ILK bKO mice compared to ILK cKO mice (Figure 13a, 7e). Additionally, not all but some studies with hypovascularized islet cores also observe only minimal impairment of glucose tolerance *in vivo,* suggesting that the few remaining blood vessels can compensate the lack of the intra-islet vasculature[104]. Interestingly, after overnight fasting and during a GTT S961-ILK bKO mice displayed significant lower plasma insulin concentrations compared to S961-control mice (Figure 14c, d). To our surprise, isolated control and ILK bKO islets from S961-treated mice showed no difference in insulin secretion under low and high glucose concentrations (Figure 14e). These observations provide evidence that *Ilk*-deficient beta cells were not functionally impaired but rather exhibited a delay to secrete insulin into the circulatory system or to perceive the glucose stimulus, which is caused by the reduced intra-islet EC density. Our results are in line with other studies that observed a delayed insulin secretion in hypovascularized islets as well[91, 261]. The missing intra-islet vasculature caused a greater distance between the insulin secreting beta cells and the islet capillaries. As a consequence,

not during normal physiological conditions, but during an insulin resistance condition, the missing intra-islet vasculature likely impaired the enhanced insulin secretion of ILK bKO mice during a GTT. Interestingly, S961-ILK bKO mice showed by tendency to a better insulin tolerance compared to S961-conrol mice (Figure 14f, g). This observation might be an explanation for the similar blood glucose levels of S961-treated mice, despite the significantly lower insulin concentrations of S961-ILK bKO during a GTT. Further experiments to investigate the insulin resistance in *Ilk* knockout mice in more detail have to be performed to support our hypothesis.

Several studies demonstrated that chronic hyperglycemia and insulin resistance promote beta cell proliferation in order to increase functional beta cell mass and thereby maintain glucose homeostasis[262-264]. However, the exact underlying mechanisms by which beta cell proliferation is induced remain unknown. Interestingly, our results showed that during S961-induced beta cell proliferation, a beta cell specific *Ilk* knockout led to a significantly lower proliferation rate (Figure 15a-c). Previous studies showed that the lack of an intra-islet vasculature does not influence adult beta cell proliferation, neither during standard conditions[2, 261] nor during a high-fat diet-induced insulin resistance condition[265]. Several studies demonstrated that the β1 integrin pathway can act as a positive as well as negative regulator of beta cell prolieration[127, 196]. In other tissues, ILK promotes proliferation via activation of the PI3K/Akt pathway[266], and also beta cell proliferation can be induced via the PI3K/Akt pathway[39]. As a key component of the β1 integrin signaling cascade *Ilk* might also promote beta cell proliferation via the PI3K/Akt pathway during insulin resistance. Surprisingly, the lower proliferation rate in S961-ILK bKO compared to S961-control mice did not result in smaller pancreatic islets (Figure 15e). This observation was not caused by bigger individual beta cells, which were increased (hypertrophy) in S961-treated mice but to the same extent between the control and ILK bKO mice (Figure 15f). Furthermore, *Ilk*-deficient beta cells and/or the absence of the intra-islet vasculature did not cause beta cell apoptosis, which could have explained the same islet size between S961-treated control and ILK bKO mice (Figure 15d).

Our results showed that already 14 days of chronic hyperglycemia and hyperinsulinemia induce microvascular changes in pancreatic islets as well as beta cell proliferation. Our findings indicate that ILK and the intra-islet vasculature have different roles during standard and insulin resistance conditions. We suggest that ILK promotes beta cell proliferation during beta cell compensation, but the exact mechanisms require further analysis. Furthermore, ILK and the intra-islet vasculature are likely needed for sufficient insulin release into the circulatory system of insulin resistant mice during a GTT. Noteworthy, we could not determine if the described effects are due to *Ilk* signaling in beta cells or due to its consequence, the missing intra-islet vasculature.

5.3.4 Methods

5.3.4.1 Mouse strains

For beta cell specific deletion of *Ilk*, *Ins1*^{Cre} knock-in[198] and *Ilk*$^{fl/fl}$ [137] mice were crossed on a C57BL/6 background. All experiments were performed with 9-10-week-old *Ins1*^{Cre}*; Ilk*$^{fl/+}$ (controls) and *Ins1*^{Cre}*; Ilk*$^{fl/fl}$ (ILK bKO) male mice. All mice were taken from the Oskar Minkowski Laboratory (DDZ, German Diabetes Center), where the mice were kept at a constant temperature of 22°C, humidity of 55% and a 12-hour light/dark cycle. Mice were fed with standard chow (Ssniff Spezialdiäten) and water *ad libitum*. All animal experiments were performed at the German Diabetes Center (DDZ Düsseldorf, Germany), are approved by the local Animal Ethics Committee of the Landesamt für Natur, Umwelt und Verbraucherschutz Nordrhein-Westfalen (LANUV North Rhine-Westphalia, Germany), and were conducted according to the German Animal Protection Laws.

5.3.4.2 Genotyping

The genotyping of *Ilk* knockout mice was performed with ear skin (leftover tissue after ear hole marking) or tail tips. All mice were genotyped three weeks after birth and used for breeding's or experiments. Additionally, to confirm the genotype, mice were shortly before as well as after the experiment genotyped again. Tissue samples (ear skin or tail tip) were lysed in 500µl lysis buffer for at least 1 hour or overnight at 55°C and 800 rpm.

1x lysis buffer	**For 100ml**
0.1 M Tris pH 8.0	10 ml 1M
0.2 M NaCl	4 ml 5M
5 mM EDTA	1 ml 0.5M
0.4% SDS	2 ml 20%
Before use, proteinase K was added to a final concentration of 0.2 mg/mL	

After tissue lysis, isopropanol and ethanol precipitation were performed to purify DNA samples. DNA was dissolved in 100 µl H_2O and frozen at -20°C or directly used for polymerase chain reaction (PCR) analysis. Following master mix was used for PCR:

Master mix component	***Ins1-Cre***	***Ilk-loxP***
GoTaq® G2 Master Mix (Promega, M7822)	10.0 µl	10.0 µl
Primer fwd (100 pmol/µl, Eurogentec)	0.5 µl	0.2 µl
Primer rev (100 pmol/µl, Eurogentec)	0.5 µl	0.2 µl
H_2O	8.0 µl	8.6 µl
Lysate	1 µl	1 µl

Following Primers (ordered by Eurogentec) were used:

Mouse line	Primer sequence (5'→ 3')		Product size
Cre-unspecific	fwd:	GCC TGC ATT ACC GGT CGA TGC AAC GA	700 bp
	rev:	GTG GCA GAT GGC GCG GCA ACA CCA TT	(Cre-positive)
Ilk-loxP	fwd:	GTC TTG CAA ACC CGT CTC TGC G	296 bp (wildtype)
	rev:	CAG AGG TGT CAG TGC TGG GAT G	370 bp (floxed)

PCRs were run on a Professional Trio Thermocycler (Biometra) using the following protocols:

Ilk-loxP				
Step	°C	Min:Sek	Go to	Loops
1	95.0	05:00	--	--
2	95.0	00:30	--	--
3	62.0	00:30	--	--
4	72.0	00:30	2	29
5	72.0	07:00	--	--
6	10.0	∞	--	--

Cre-unspecific				
Step	°C	Min:Sek	Go to	Loops
1	94.0	05:00	--	--
2	94.0	00:30	--	--
3	58.0	00:30	--	--
4	72.0	01:00	2	34
5	72.0	05:00	--	--
6	10.0	∞	--	--

Next, the samples and a 100 bp DNA ladder (New England Biolabs) were loaded on a 2% agarose gel (VWR) containing 5% SYBR® Safe DNA gel stain (Invitrogen). Gel electrophoresis was run at 120 V for around 30 minutes (PowerPac HC power supply, Biorad). Finally, gels were imaged at a ChemiDoc XRS System (Biorad) and genotypes of mice were recorded.

5.3.4.3 Alzet osmotic minipumps

Alzet osmotic minipumps (1002) were used to deliver the insulin receptor antagonist S961 into mice. Alzet pumps allow a continuous and controlled release of the previously loaded compound, leading to a permanent compound level in the blood. In this study, the Alzet pump model 1002 was used, releasing 0.25 µl/ hour compound. The pump was implanted for 14 days and either EdU injections or a glucose tolerance test (GTT) followed by an insulin tolerance test (ITT) were performed during this time (Figure 16). The mice were monitored daily including measurement of blood glucose levels. Therefore, a small cut at the end of the tail was made and a single drop of blood was analyzed using a glucometer (CONTOUR® XT, Bayer). At certain days additional blood was taken (20 µl) for insulin or glucagon determination (Figure 16). After 14 days the mice were sacrificed, and the pancreas or pancreatic islets were isolated for further analysis.

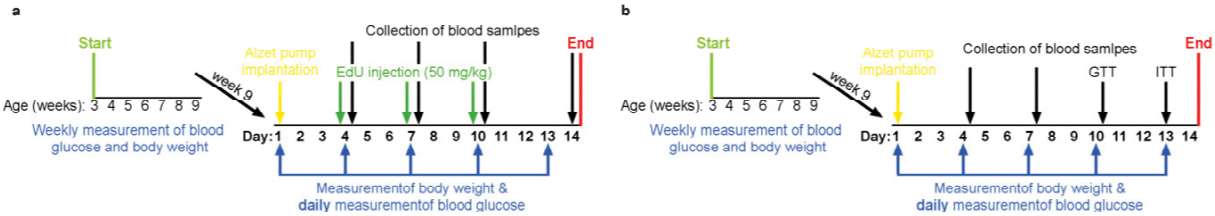

Figure 16: ***Experimental setup.*** (**a**, **b**) Alzet pumps were implanted in 9-10-week-old *Ins1*^{Cre}*; Ilk*$^{fl/fl}$ and *Ins1*^{Cre}*; Ilk*$^{fl/+}$ mice. After Alzet pump implantation, either EdU injections (**a**) or a glucose tolerance test and an insulin tolerance test (**b**) were performed. Pancreata (**a**) or pancreatic islets (**b**) were isolated 14 days after Alzet pump implantation and further analyzed.

5.3.4.4 Alzet pump priming

Alzet minipumps (1002) were loaded with PBS (Gibco) or 20 nM S961 (solved in PBS) following the manufacturer's instructions. S961 was a kind gift from L. Schäffer (Novo Nordisk). All pumps were filled with more than 90% of the specified reservoir volume, which was confirmed by calculating the difference between the weights of the empty and filled pump. Subsequently, pumps were placed in Eppendorf tubes, filled with PBS and stored overnight at in a humidified 37°C and 5% CO_2 incubator. This “priming” ensured a direct release of PBS/S961 after pump implantation, skipping the start-up gradient, where the pump soaks up fluid and comes to temperature

5.3.4.5 Alzet pump implantation

Alzet minipumps were implanted subcutaneously in 9-10-week-old male control or ILK bKO mice. First, the mouse is anesthetized with Isoflurane (3 Vol.% Isoflurane with 40 Vol.% oxygen enriched surrounding air) in an anesthesia chamber. As soon as the anesthesia was sufficient the mouse was transferred to a heated operation desk (37°C) to ensure a constant body temperature. Anesthesia was continued via a respiratory mask (2.0 Vol.% isoflurane with 40 Vol.% oxygen enriched surrounding air). The skin was shaved, disinfected and a suitable incision was made at the mid-scapular line. A hemostat was inserted into the incision and by gently opening and closing the jaws, a subcutaneous pocket was formed. The filled pump was carefully inserted into the pocket. Subsequently, the wound was closed with wound clips, disinfected and Rimadyl (1 mg/kg bodyweight, Zoetis, PZN: 110208) was injected subcutaneously. The mice were placed under an infrared lamp to recover from the operation. Following the operation, mice were kept in single cages and wound healing as well as wellbeing were controlled daily. Rimadyl was subcutaneously injected for 3 consecutive days.

5.3.4.6 Glucose tolerance test

A glucose tolerance test was performed 10 days after Alzet pump implantation (Figure 16b). Mice were fasted overnight (16 hours) by transferring mice into clean cages without food but

unlimited access to drinking water. On the following day, mice were weighed, a blood sample was collected (20 µl) and blood glucose concentration were measured with a glucometer (CONTOUR® XT, Bayer) as described in 5.3.4.3. Subsequently, glucose (2 mg/ g bodyweight) was injected intraperitoneally. Glucose levels were measured 15, 30, 60, 90, 120 and 180 minutes after glucose injection. Blood samples (20 µl, for insulin ELISA) were taken at 30, 60 and 120 minutes after glucose injection. Upon completion, food was provided, and wellbeing of mice was ensured. The order of the mice regarding genotype (control or ILK bKO) or Alzet pump (PBS or S961) was randomized.

5.3.4.7 Insulin tolerance test

An insulin tolerance test was performed 13 days after Alzet pump implantation (Figure 16b). Prior, mice were transferred into clean cages without food but unlimited access to drinking water and fasted for 4 hours. Next, mice were weight and blood glucose levels were measured with a glucometer (CONTOUR® XT, Bayer) as described in 5.3.4.3. Subsequently, mice were injected intraperitoneally with an insulin solution (0.75 U/kg bodyweight in PBS) and glucose levels were measured 15, 30, 60 and 90 minutes after insulin injection. After 90 minutes mice were fed and wellbeing was assured. The order of the mice regarding genotype (control or ILK bKO) or Alzet pump (PBS or S961) was randomized.

5.3.4.8 EdU injections

To detect cell proliferation, 5-ethynyl-2'-deoxyuridine (EdU, Sigma) was used. EdU, a nucleoside analog to thymidine, integrates into the genome during DNA synthesis. Mice received three intraperitoneal EdU (50 mg/kg bodyweight) injections (4, 7, 10 days after Alzet pump implantation) (Figure 16a). 14 days after Alzet pump implantation mice were killed by cervical dislocation, the pancreas was isolated and cryostat sections were produced (see 5.3.4.9). Pancreatic sections were stained according to the manufacturer's instructions using the Click-iT® copper-catalyzed covalent reaction between an Azide (fluorophore, 6-FAM Azide) and an alkyne (EdU) (see 5.3.4.15).

5.3.4.9 Isolation of pancreas and cryosectioning

To create sections of the pancreas for immunostaining, the pancreas was isolated. Therefore, the mouse was killed via cervical dislocation and an incision was made to expose the intestine and the liver. The intestines were cautiously pulled out. Beginning at the spleen, the pancreas was gently plucked off along the stomach, following the duodenum and intestines. The isolated pancreas was weighed and directly transferred into in 4% paraformaldehyde in PBS and fixed for two hours at 4 °C. Following fixation, equilibration with increasing sucrose concentrations (7,5%, 15%, 30%; Carl Roth) was performed. The pancreas was embedded in Tissue-Tek®

optimum cutting temperature (O.C.T.) medium (Sakura) and frozen at -20°C. A Microm HM560 Cryostat (ThermoFischer) and MX35 premier microtome blades (ThermoFisher Scientific) were used to obtain 12 µm sick tissue sections that were collected on SuperFrost slides (ThermoFisher Scientific). Slides were stored at -20°C before processing first EdU chemistry and then immunostaining (see 5.3.4.15 & 5.3.4.16).

5.3.4.10 Isolation of mouse pancreatic islets

The isolation of mouse pancreatic islets was performed according to the protocol that was previously described in Yesil et al.[245]. Briefly, the mouse was killed via cervical dislocation, the intestines were exposed and the vaterpapille was sealed with a clamp. Next, 3 ml Liberase TL Research Grade (Roche) was injected into the pancreatic duct. Subsequently, the pancreas was isolated as described before (5.3.4.9) and stored on ice. Pancreata were enzymatically digested for exactly 17.5 minutes in a 37°C water bath. The reaction was stopped with DMEM GlutaMAX™ medium (1 g/l glucose) supplemented with 15% FBS (Gibco). After washing and filter steps, a gradient centrifugation (at 1,200 rpm for 25 minutes) with DMEM GlutaMAX™ medium (1 g/l glucose) and Histopaque-1077 (Sigma-Aldrich) was performed. Pancreatic islets accumulated in the interphase and were transferred in a petri dish with CMRL 1066 (containing heat-inactivated FBS 15%, penicillin 100 U/ml, streptomycin 100 µg/ml, NaHCO3 0.15%, 2-mercaptoethanol 0.05 mM, glucose 10 mM) medium. Islets were washed twice to free from exocrine tissue and were subsequently stored in CMRL 1066 medium in a humidified 37°C and 5% CO_2 incubator. Functional experiments were performed the next day.

5.3.4.11 Insulin secretion from mouse pancreatic islets

In vitro insulin secretion of pancreatic islets was performed as described before in Kragl et al.[2]. Pancreatic islets were isolated the day before as described above (see 5.3.4.10). On the following day, eight similar looking islets that were round, not frayed and same sized were picked and transferred into a round bottom well of a 96-well plate. The islets were starved for 1 hour in Krebs Ringer HEPPES (KRH) buffer (15 mM HEPES, 5 mM KCl, 120 mM NaCl, 24mM $NaHCO_3$, 2 mM $Cacl_2$, 0.01 mM glycine, 1 mg/ml BSA) supplemented with 2 mM glucose in a humidified 37°C and 5% CO_2 incubator. For low and high glucose stimulation, the same islets were incubated 1 hour in fresh KRH buffer supplemented with 2 mM glucose (low glucose), followed by an 1-hour incubation with fresh KRH buffer supplemented with 25 mM glucose (high glucose). All incubation steps during insulin secretion assays were performed at 37 °C and 5% CO_2. Supernatants were collected after each incubation step to determine the basal and glucose stimulated insulin secretion of isolated islets. Subsequently, islets were lysed in 250 µl RIPA buffer (50 mM Tris-HCl pH 7.4, 150 mM NaCl, 1% IGEPAL, 0.25% Na-deoxycholate, 1x Roche complete mini protease inhibitor cocktail) to measure insulin

content. Insulin secretion was measured using the ultrasensitive rat insulin ELISA (Crystal Chem) in combination with an Infinite M200 NanoQuant reader (Tecan) and normalized to total insulin content (see 5.3.4.12).

5.3.4.12 Insulin ELISA

Insulin secretion was determined either from blood samples or from supernatant of isolated pancreatic islets. Blood samples were collected during blood glucose measurements at a random time point or during the glucose tolerance test at 0, 30, 60 and 120 minutes after glucose injection. Blood was collected in tubes containing ethylenediaminetetraacetic acid (EDTA) as anticoagulant and plasma fraction was separated via centrifugation for 5 min at 2000 rpm at 4 °C. Samples were stored at -80°C. Generation of samples from isolated islets is described above (5.3.4.11). Insulin values were measured with the ultrasensitive rat insulin ELISA (Crystal Chem, 90060). The protocol was performed following the manufacturer's instructions. Values obtained from isolated islets were normalized to total insulin content.

5.3.4.13 Glucagon ELISA

To determine glucagon secretion of pancreatic islets, blood samples were obtained after a short fasting period (4 hours). Blood was collected in EDTA coated tubes and plasma was separated by centrifugation. Glucagon ELISA (Mercodia, 10-1281-01) including commercial internal quality controls (low, medium, high glucagon) (Mercodia, 10-1286-01) was performed according the manufacturer's protocol. Optical density was read at NanoQuant Infinite M200 Reader (Tecan).

5.3.4.14 RNA isolation and real-time RT-PCR

To analyze the knock down efficiency of pancreatic islets of control and ILK bKO mice, the islets were isolated as described above (see 5.3.4.10). On the following day islets were washed once with PBS and divided into similar groups. RNA extraction was performed with the RNeasy kit (Qiagen) and RNA concentration and quality were checked at the BioMateTM 3 (Thermo Fisher Scientific). To obtain complementary DNA 0.2 µg purified RNA and the MMLV-RT enzyme (Promega) was used. Reverse transcription reaction was performed according to the manufacturer's protocol with following master mix:

Component	+ RT	- RT control
RNasin (Promega)	0.5 µl	0.5 µl
dNTPs (Sigma)	1.25 µl	1.25 µl
MMLV-RT buffer (Promega)	5 µl	5 µl
MMLV-RT enzyme (Promega)	1 µl	0 µl
H_2O	2.25 µl	3.25 µl

Reverse transcription was performed for 1 hour at 42°C. Finally, cDNA was diluted 1:5 with H_2O and stored at -20°C.

The cDNA obtained from reverse transcription was used as template for real-time RT-PCR. Protocol was performed to the manufacturer's instructions (Aligent). Following master mix was used for one sample:

Component	Volume
SYBER green (2x Brilliant III SYBR Green QPCR Master Mix, Agilent)	5 µl
Primer mix (see below, fwd and rev primer diluted to 3 µM)	1 µl
H_2O	1 µl
cDNA	3 µl

Every sample was run in triplicates (gene of interest) plus a single -RT control. Housekeeping gene Hypoxanthine-guanine-phosphoribosyltransferase (Hprt) was used and samples were analyzed according the cycle threshold (Ct) method. Primers with following sequences were used:

Gene	Primer sequence (5'→ 3')
Mouse *Ilk* forward	GTG GCT GGA CAA CAC AGA GA
Mouse *Ilk* reverse	ATC CCC ACG ATT CAT CAC AT
Mouse *Hprt* forward	CAC AGG ACT AGA ACA CCT GC
Mouse *Hprt* reverse	GCT GGT GAA AAG GAC CTC T

5.3.4.15 EdU Click-IT reaction

Tissue sections were obtained as described above (see 5.3.4.9). To visualize proliferating cells, EdU staining was performed according to the protocol provided by the company (Sigma). Briefly, slides were washed once with PBS^+ (Ca^{2+}, Mg^{2+}) and once with 0.5% Triton X-100 in PBS^+ for 5 minutes each and subsequently blocked with 3% BSA in PBS^+ four times for 3 minutes. Click-IT reaction cocktail was prepared and 200 µl Click-IT reaction cocktail was added to every slide and incubated for 30 minutes at RT:

Click-IT reaction cocktail	µl
Deionized water	151.6
Reaction buffer (10x)	20
Catalyst solution	8
6-FAM Azide (10 mM)	0.4
Buffer additive (10x)	20

Subsequently, slides were blocked three times with 3% BSA in PBS^+ and washed two times for 10 minutes with 0.2% Triton in PBS^+. After this step, the staining protocol described in 5.3.4.16 was continued.

5.3.4.16 Immunostaining

For immunostaining slides where washed once 5 min with PBS^+ and once 5 min with PBS^+ containing 0.2% Triton X-100 (Carl Roth) (0.2% PBS-T). Blocking solution was made of 3% normal donkey serum (NDS, Jackson ImmunoResearch), 5% bovine serum albumin (BSA, AppliChem) in 0.2% PBS-T. Slides were blocked in a humid chamber for 1 hour with 200 µl blocking solution at RT. Subsequently, the following primary antibodies were diluted in 150µl blocking solution and added to the slides:

Primary antibodies	**Dilution**
Polyclonal guinea pig anti-insulin (Dako, A0564)	1:500
Polyclonal rat anti-CD31 (BD Pharmingen, 550274)	1:50
Polyclonal rabbit anti-phospho-Histone H3 (Millipore, 06-570)	1:200
Monoclonal rabbit anti-cleaved caspase-3 (Cell Signaling, 9664)	1:200

Slides incubated with the primary antibody solution over night at 4°C. The next day, slides were washed four times for 10 minutes with 0.2% PBS-T. For each slide 150 µl blocking solution with diluted secondary antibody (see below) were added for one hour at RT:

Secondary antibodies	**Dilution**
Dapi (Sigma)	1:1000
Donkey anti-guinea pig conjugated with Cy3 (Jackson ImmunoResearch)	1:500
Donkey anti-rat conjugated with Alexa Fluor 488 (Life Technologies)	1:500
Donkey anti-rat conjugated with Cy5 (Jackson ImmunoResearch)	1:500
Donkey anti-rabbit conjugated with Alexa Fluor 488 (Jackson ImmunoResearch)	1:500
Donkey anti-rabbit conjugated with Alexa Fluor Cy5 (Jackson ImmunoResearch)	1:500

Next, slides were washed four times with 0.2% PBS-T. Finally, slides were mounted with Fluoroshield (Sigma) and a coverslip. All slides were stored dark at 4°C until imaging.

5.3.4.17 Imaging and image analysis

Images were captured with a confocal laser scanning microscope (LSM 880) coupled to an Axio Observer.Z1 and Zen black software (Carl Zeiss). Images of islets were taken with either 10x or 20x objectives and as z-stacks. For image analysis, Fiji (ImageJ) software was used[189]. Maximum intensity projections were performed before analysis. Of each mouse, at least 10 islets from at least four different pancreatic sections were analyzed, if not stated otherwise. For blood vessel density analysis (Figure 13b-d), endothelial cell number and localization was analyzed by hand and normalized to total $insulin^+$ cell number, which was analyzed using

threshold analysis and extended particle analyzer (The BioVoxxel Image Processing and Analysis Toolbox. Brocher, 2015, EuBIAS-Conference, 2015, Jan 5) in Fiji (ImageJ). For analysis of blood vessel morphology (Figure 13e-g), only islets with a ratio <0.04 of intra-islet ECs to insulin$^+$ cells were analyzed. For analysis of blood vessel size (Figure 13e), CD31$^+$ area was determined using Fiji threshold method and extended particle analyzer (BioVoxxel). For analysis of blood vessel diameter (Figure 13f), at least six blood vessels of an islet and at least six islets per mouse were measured by hand. For the analysis of blood vessel coverage (Figure 13g), the CD31$^+$ area was determined using Fiji threshold method and insulin$^+$ area was determined by hand. For analysis of cell proliferation and apoptosis (Figure 15b-d), EdU$^+$, PH3$^+$ or CC3$^+$ positive cells were counted/ analyzed by hand and normalized to total insulin$^+$ cells. Total insulin$^+$ cell number was determined using threshold analysis (Fiji) and extended particle analyzer (BioVoxxel). Islet size (Figure 15e) was determined by insulin$^+$ area, which was measured by hand. For beta cell size analysis (Figure 15f), insulin$^+$ cell number was normalized to insulin$^+$ area. All image analysis was performed blinded.

5.3.4.18 Statistical analyses

Statistical significance was determined by using GraphPad Prism (GraphPad Software) or Excel (Microsoft) software. For comparison of two groups an unpaired two-tailed Student's t-test was performed (Excel). For comparison of more than two groups, two-way ANOVAs was performed (Prism). In addition, for multiple comparisons, Tukey`s multiple comparison test was performed (Prism). Significant outliers were detected for beta cell proliferation analysis (Figure 15b, c) by the extreme studentized deviate method (Grubbs' test) and excluded from the statistical analysis (Prism). Throughout this thesis, quantifications are shown as means ± standard deviations (s.d.). In all cases, *P* value < 0.05 was considered statistically significant.

5.3.5 Additional Information

5.3.5.1 Supplementary Information

Supplementary information can be found in section 9.3.

5.3.6 Personal Contribution and general information

Haiko Karsjens performed all experiments and was supervised by Prof. Dr. Eckhard Lammert; funded by the Competence Network Diabetes mellitus (KKNDm) and the German Center for Diabetes Research (DZD e.V.), as well as the German Diabetes Center (DDZ), the Federal Ministry of Health and the Ministry of Culture and Science of North Rhine-Westphalia.

Okka Scholz assisted during glucose tolerance tests and Barbara Bartosinska during islet isolation.

Celina Uhlemeyer was co-supervised by Haiko Karsjens during her Bachelor Thesis in 2017 and Oksana Lewandowska who was supervised by Haiko Karsjens during her Pilotarbeit in 2019. Both worked on related topics to this thesis.

In sum, Haiko Karsjens contributed to the work of this manuscript with approximately 95%.

6 Conclusion & Outlook

This thesis combines published articles and unpublished experiments that provide new insights into the analysis of sprouting angiogenesis as well as the role of ILK in pancreatic islets.

The presented bead sprouting angiogenesis assay provides a robust *in vitro* assay using primary human endothelial cells and pericytes. For the first time, our new setup allows the analysis of sprouting endothelial cells and their supporting pericytes in a defined cellular setup. Our ImageJ plugin provides an automated and time-saving method to analyze different vascular parameters like sprout length, branch points and pericyte coverage. However, *in vitro* assays can always just mimic the conditions present *in vivo.* The absence of blood flow, which influences endothelial cell signaling and is regulated by pericytes cannot be recapitulated in our assay[97, 267]. Furthermore, it would be worthwhile to analyze the effects of blood plasma or supernatants from cells (e.g. adipocytes) of diabetic patients on sprouting angiogenesis and pericyte coverage. Here, we offer a new *in vitro* assay that completes a range of other *in vitro* assays[184, 268-274] and will help to characterize the effects of different compounds on sprouting angiogenesis and pericyte coverage in more detail and under more physiological conditions.

Furthermore, we show for the first time that not only cellular and molecular components like growth factors but also the biochemical properties of an epithelial tissue (pancreatic islets), namely their actomyosin-mediated cortex tension and their adhesion forces to endothelial cells, determine its vascularization. We suggest that ILK negatively regulates non-muscle myosin-II via inhibition of Rho/ROCK signaling, which in turn leads to a decreased cell cortex tension in islet cells. This enables their adhesion to endothelial cells and thereby the vascularization of pancreatic islets. Future studies will have to keep under consideration that the biomechanical properties of an epithelial tissue influence its vascularization.

We continued our work with a more detailed analysis of ILK and the intra-islet vasculature for beta cell function and proliferation. *Ilk*-deficient beta cells form pancreatic islets with a reduced number of intra-islet endothelial cells, which is most likely due to an increased cell cortex tension and a decreased adhesion to endothelial cells - similar to *Ilk* in the pancreatic epithelium. To prove this assumption, single-cell force spectroscopy (SCFS) experiments should be performed to determine the cortex tension of *Ilk*-deficient beta cells. We show that adult quiescent beta cells regain proliferative capability within 14 days of chronic hyperglycemia and that *Ilk* supports beta cell proliferation. Future experiments should focus on altered signaling pathways in *Ilk*-deficient beta cells to reveal the underlying mechanisms, which could be identified by isolation and FACS-sorting of beta cells followed by single qPCR or single-cell RNA sequencing (scRNA-seq). Furthermore, insulin resistant *Ilk* knockout mice show a reduced insulin secretion during a glucose tolerance test. Since the reduced insulin secretion does not lead to changes in glucose tolerance between insulin resistant control and beta cell-specific *Ilk* knockout mice, future experiments should further investigate insulin

resistance in these mice. An insulin tolerance test shows an improved insulin tolerance of *Ilk* knockout mice by tendency. However, the gold standard method of *in vivo* measurement of insulin sensitivity, is the euglycemic hyperinsulinemic clamp technique[275], which should be performed in future experiments. Furthermore, immunofluorescence staining could reveal whether insulin is trapped in *Ilk*-deficient beta cells, followed by analysis of altered insulin signaling in beta cells. In addition, since pericyte coverage in pancreatic islets drops during T2D[97], it would be worthwhile to determine pericyte coverage in insulin resistant *Ilk* knockout mice.

New targets for the development of new treatments, which halt the progression from insulin resistance to T2D, are greatly needed and require a deeper understanding of the underlying molecular mechanisms. One approach is to support beta cell survival and to replenish beta cell mass in order to increase insulin production. My thesis introduces ILK as a regulator for beta cell proliferation and insulin secretion during insulin resistance and thus is a potentially candidate for future T2D treatment.

7 List of abbreviations

A	
ADP	Adenosine diphosphate
AF	Alexa Fluor
ANOVA	Analysis of variance
ATP	Adenosine triphosphate
B	
bKO	Beta cell-specific knockout
bp	base pairs
BSA	Bovine serum albumin
C	
Ca^{2+}	Calcium
$CaCl_2$	Calcium chloride
CAMs	Cell adhesion molecules
cDNA	Complementary DNA
cKO	Conditional knockout
Cre	Cre recombinase
Ct	Cycle threshold
D	
Dapi	4′,6-Diamidino-2-phenylindole
DNA	Deoxyribonucleic acid
E	
EC	Endothelial cell
ECM	Extracellular matrix
EDTA	Ethylenediaminetetraacetic acid
EdU	5-ethynyl-2'-deoxyuridine
EGM-2	Endothelial growth medium-2
ELISA	Enzyme-linked immunosorbent assay
F	
FFA	Free fatty acids
fwd	Forward
G	
GLUT	Glucose transporter
GPR40	G-protein coupled receptor 40
GSIS	Glucose-stimulated insulin secretion
GWAS	Genome-wide association study

H

HBVP	Human brain vascular pericytes
HEPES	4-(2-hydroxyethyl)-1-piperazineethanesulfonic acid
HIF-1α	Hypoxia-inducible factor 1α
Hprt	Hypoxanthine-guanine-phosphoribosyltransferase
HSF	Human skin fibroblasts
HUVEC	Human umbilical vein endothelial cells

I

ILK	Integrin-linked kinase
Ins	Insulin
IPP	ILK PINCH PARVIN
IR	Insulin receptor
IRS	Insulin receptor substrates
i.p.	Intraperitoneal

K

KCl	Potassium chloride
KO	Knockout
KRH	Krebs Ringer HEPPES

L

LSM	Laser scanning microscopy

M

M	Molar
Mafa	MAF BZIP transcription factor A
MAPK	Mitogen-activated protein kinase
Mg^{2+}	Magnesium
Min	Minute
MIP	Maximum intensity projection
Munc	Mammalian uncoordinated

N

NaCl	Sodium chloride
NADP	Nicotinamide adenine dinucleotide phosphate
$NaHCO_3$	Sodium bicarbonate
NDS	Normal donkey serum
NEFA	Non-esterified fatty acid

P	
PBS	Phosphate buffered saline
PCR	Polymerase chain reaction
PDGF	Platelet-derived growth factor
Pdx1	Pancreatic and duodenal homeobox 1
PH3	Phospho-Histone H3
PI3K	Phosphoinositide 3-kinase
PIGF	Placental growth factor
PINCH	Particularly interesting new cysteine-histidine-rich protein
R	
rev	Reverse
RNA	Ribonucleic acid
ROS	reactive oxygen species
rpm	Revolutions per minute
RRP	Readily releasable pool
RT	Room temperature
RTK	Receptor tyrosine kinase
S	
s.c.	Subcutaneous
SDS	Sodium dodecyl sulfate
SNARE	soluble N-ethylmaleimide-sensitive factor attachment protein receptor
SNP	Single nucleotide polymorphism
T	
TSP-1	Thrombospondin-1
Tris	Tris-aminomethan
U	
U	Unit
V	
V	Volt
VEGF	Vascular endothelial growth factor
VEGFR	Vascular endothelial growth factor receptor
W	
WHO	World Health Organization
0-9	
6-FAM Azide	6-Carboxyfluorescein Azide

8 References

1. Eglinger, J., Karsjens, H. & Lammert, E. Quantitative assessment of angiogenesis and pericyte coverage in human cell-derived vascular sprouts. *Inflammation and Regeneration* **37** (2017).
2. Kragl, M. *et al.* The biomechanical properties of an epithelial tissue determine the location of its vasculature. *Nature Communications* **7**, 13560 (2016).
3. Saeedi, P. *et al.* Global and regional diabetes prevalence estimates for 2019 and projections for 2030 and 2045: Results from the International Diabetes Federation Diabetes Atlas, 9(th) edition. *Diabetes Res Clin Pract* **157**, 107843-107843 (2019).
4. World-Health-Organization Global health estimates 2016 (deaths by cause, age, sex, by country and by region, 2000–2016; and life expectancy, 2000–2016). (2018).
5. Röder, P.V., Wu, B., Liu, Y. & Han, W. Pancreatic regulation of glucose homeostasis. *Exp Mol Med* **48**, e219 (2016).
6. Zhou, Q. & Melton, D.A. Pancreas regeneration. *Nature* **557**, 351-358 (2018).
7. Baskin, D.G. A Historical Perspective on the Identification of Cell Types in Pancreatic Islets of Langerhans by Staining and Histochemical Techniques. *Journal of Histochemistry & Cytochemistry (The Histochemical Society)* **63**, 543-558 (2015).
8. Kim, A. *et al.* Islet architecture: A comparative study. *Islets* **1**, 129-136 (2009).
9. Dolenšek, J., Rupnik, M.S. & Stožer, A. Structural similarities and differences between the human and the mouse pancreas. *Islets* **7**, e1024405 (2015).
10. Brissova, M. *et al.* Assessment of human pancreatic islet architecture and composition by laser scanning confocal microscopy. *J Histochem Cytochem* **53**, 1087-1097 (2005).
11. Eberhard, D., Kragl, M. & Lammert, E. 'Giving and taking': endothelial and beta-cells in the islets of Langerhans. *Trends Endocrinol Metab* **21**, 457-463 (2010).
12. Britannica, T.E.o.E. Islets of Langerhans. *Encyclopædia Britannica, Inc.* (July 11, 2018).
13. Reno, C.M. *et al.* Severe hypoglycemia-induced sudden death is mediated by both cardiac arrhythmias and seizures. *American Journal of Physiology-Endocrinology and Metabolism* **315**, E240-E249 (2018).
14. Laakso, M. & Kuusisto, J. Insulin resistance and hyperglycaemia in cardiovascular disease development. *Nat Rev Endocrinol* **10**, 293-302 (2014).
15. Dunn, M.F. Zinc-ligand interactions modulate assembly and stability of the insulin hexamer - a review. *Biometals* **18**, 295-303 (2005).
16. Olofsson, C.S. *et al.* Fast insulin secretion reflects exocytosis of docked granules in mouse pancreatic B-cells. *Pflugers Arch* **444**, 43-51 (2002).
17. Rorsman, P. *et al.* The Cell Physiology of Biphasic Insulin Secretion. *News Physiol Sci* **15**, 72-77 (2000).
18. Jiang, G. & Zhang, B.B. Glucagon and regulation of glucose metabolism. *American journal of physiology. Endocrinology and metabolism* **284**, E671-E678 (2003).
19. Mueckler, M. & Thorens, B. The SLC2 (GLUT) family of membrane transporters. *Mol Aspects Med* **34**, 121-138 (2013).
20. Thorens, B. GLUT2, glucose sensing and glucose homeostasis. *Diabetologia* **58**, 221-232 (2015).
21. Lenzen, S. A fresh view of glycolysis and glucokinase regulation: history and current status. *The Journal of biological chemistry* **289**, 12189-12194 (2014).
22. Ashcroft, F.M. & Rorsman, P. ATP-sensitive K+ channels: a link between B-cell metabolism and insulin secretion. *Biochem Soc Trans* **18**, 109-111 (1990).
23. Mancini, A.D. & Poitout, V. The fatty acid receptor FFA1/GPR40 a decade later: how much do we know? *Trends in Endocrinology & Metabolism* **24**, 398-407 (2013).
24. Gaisano, H.Y. Here come the newcomer granules, better late than never. *Trends in endocrinology and metabolism: TEM* **25**, 381-388 (2014).
25. Rorsman, P. & Braun, M. Regulation of Insulin Secretion in Human Pancreatic Islets. *Annual Review of Physiology* **75**, 155-179 (2013).
26. Rorsman, P. & Renström, E. Insulin granule dynamics in pancreatic beta cells. *Diabetologia* **46**, 1029-1045 (2003).
27. Newsholme, P., Bender, K., Kiely, A. & Brennan, L. Amino acid metabolism, insulin secretion and diabetes. *Biochem Soc Trans* **35**, 1180-1186 (2007).
28. Newsholme, P., Brennan, L. & Bender, K. Amino acid metabolism, β-cell function, and diabetes. *Diabetes* **55**, S39-S47 (2006).
29. Dobbins, R.L. *et al.* A fatty acid- dependent step is critically important for both glucose- and non-glucose-stimulated insulin secretion. *The Journal of Clinical Investigation* **101**, 2370-2376 (1998).

30. Prentki, M., Franz & S.R Metabolic Signaling in Fuel-Induced Insulin Secretion. *Cell Metabolism* **18**, 162-185 (2013).
31. Qin, T. *et al.* Munc18b Increases Insulin Granule Fusion, Restoring Deficient Insulin Secretion in Type-2 Diabetes Human and Goto-Kakizaki Rat Islets with Improvement in Glucose Homeostasis. *EBioMedicine* **16**, 262-274 (2017).
32. Zhao, S. *et al.* α/β-Hydrolase Domain-6-Accessible Monoacylglycerol Controls Glucose-Stimulated Insulin Secretion. *Cell Metabolism* **19**, 993-1007 (2014).
33. Renström, E., Ding, W.G., Bokvist, K. & Rorsman, P. Neurotransmitter-induced inhibition of exocytosis in insulin-secreting beta cells by activation of calcineurin. *Neuron* **17**, 513-522 (1996).
34. Nauck, M.A. & Meier, J.J. Incretin hormones: Their role in health and disease. *Diabetes, Obesity and Metabolism* **20**, 5-21 (2018).
35. Drucker, D.J. The biology of incretin hormones. *Cell Metabolism* **3**, 153-165 (2006).
36. Haeusler, R.A., McGraw, T.E. & Accili, D. Biochemical and cellular properties of insulin receptor signalling. *Nature Reviews Molecular Cell Biology* **19**, 31-44 (2018).
37. Boucher, J., Kleinridders, A. & Kahn, C.R. Insulin Receptor Signaling in Normal and Insulin-Resistant States. *Cold Spring Harbor Perspectives in Biology* **6**, a009191-a009191 (2014).
38. Mosthaf, L. *et al.* Functionally distinct insulin receptors generated by tissue-specific alternative splicing. *The EMBO journal* **9**, 2409-2413 (1990).
39. Belfiore, A. *et al.* Insulin Receptor Isoforms in Physiology and Disease: An Updated View. *Endocrine Reviews* **38**, 379-431 (2017).
40. Taniguchi, C.M., Emanuelli, B. & Kahn, C.R. Critical nodes in signalling pathways: insights into insulin action. *Nature reviews. Molecular cell biology* **7**, 85-96 (2006).
41. Kraegen, E.W., James, D.E., Jenkins, A.B. & Chisholm, D.J. Dose-response curves for in vivo insulin sensitivity in individual tissues in rats. *Am J Physiol* **248**, E353-E362 (1985).
42. Martin, S. *et al.* Effects of insulin on intracellular GLUT4 vesicles in adipocytes: evidence for a secretory mode of regulation. *Journal of cell science* **113 Pt 19**, 3427-3438 (2000).
43. Bryant, N.J., Govers, R. & James, D.E. Regulated transport of the glucose transporter GLUT4. *Nature reviews. Molecular cell biology* **3**, 267-277 (2002).
44. Guo, S. Insulin signaling, resistance, and the metabolic syndrome: insights from mouse models into disease mechanisms. *J Endocrinol* **220**, T1-T23 (2014).
45. Saltiel, A.R. & Kahn, C.R. Insulin signalling and the regulation of glucose and lipid metabolism. *Nature* **414**, 799-806 (2001).
46. Titchenell, P.M., Lazar, M.A. & Birnbaum, M.J. Unraveling the Regulation of Hepatic Metabolism by Insulin. *Trends in Endocrinology & Metabolism* **28**, 497-505 (2017).
47. Dimitriadis, G., Mitrou, P., Lambadiari, V., Maratou, E. & Raptis, S.A. Insulin effects in muscle and adipose tissue. *Diabetes Res Clin Pract* **93 Suppl 1**, S52-S59 (2011).
48. Oakie, A. *et al.* Postnatal knockout of beta cell insulin receptor impaired insulin secretion in male mice exposed to high-fat diet stress. *Mol Cell Endocrinol* **499**, 110588 (2020).
49. Rhodes, C.J., White, M.F., Leahy, J.L. & Kahn, S.E. Direct Autocrine Action of Insulin on B-Cells: Does It Make Physiological Sense? *Diabetes* **62**, 2157-2163 (2013).
50. Kitamura, T., Kahn, C.R. & Accili, D. Insulin Receptor Knockout Mice. *Annual Review of Physiology* **65**, 313-332 (2003).
51. Cavaghan, M.K., Ehrmann, D.A. & Polonsky, K.S. Interactions between insulin resistance and insulin secretion in the development of glucose intolerance. *Journal of Clinical Investigation* **106**, 329-333 (2000).
52. Ferrannini, E. The Stunned β Cell: A Brief History. *Cell Metabolism* **11**, 349-352 (2010).
53. Bonner-Weir, S., Deery, D., Leahy, J.L. & Weir, G.C. Compensatory growth of pancreatic beta-cells in adult rats after short-term glucose infusion. *Diabetes* **38**, 49-53 (1989).
54. Kahn, S.E., Hull, R.L. & Utzschneider, K.M. Mechanisms linking obesity to insulin resistance and type 2 diabetes. *Nature* **444**, 840-846 (2006).
55. Talchai, C., Xuan, S., Lin, H.V., Sussel, L. & Accili, D. Pancreatic β cell dedifferentiation as a mechanism of diabetic β cell failure. *Cell* **150**, 1223-1234 (2012).
56. Butler, A.E. *et al.* Beta-Cell Deficit and Increased Beta-Cell Apoptosis in Humans With Type 2 Diabetes. *Diabetes* **52**, 102-110 (2003).
57. Butler, A.E. *et al.* β-Cell Deficit in Obese Type 2 Diabetes, a Minor Role of β-Cell Dedifferentiation and Degranulation. *J Clin Endocrinol Metab* **101**, 523-532 (2016).
58. Yaribeygi, H., Farrokhi, F.R., Butler, A.E. & Sahebkar, A. Insulin resistance: Review of the underlying molecular mechanisms. *Journal of Cellular Physiology* **234**, 8152-8161 (2019).
59. Fasshauer, M. & Blüher, M. Adipokines in health and disease. *Trends in Pharmacological Sciences* **36**, 461-470 (2015).

60. Guilherme, A., Virbasius, J.V., Puri, V. & Czech, M.P. Adipocyte dysfunctions linking obesity to insulin resistance and type 2 diabetes. *Nature reviews. Molecular cell biology* **9**, 367-377 (2008).
61. Muse, E.D. *et al.* Role of resistin in diet-induced hepatic insulin resistance. *The Journal of clinical investigation* **114**, 232-239 (2004).
62. Dunmore, S.J. & Brown, J.E.P. The role of adipokines in β-cell failure of type 2 diabetes. *Journal of Endocrinology* **216**, T37-T45 (2013).
63. Wang, J. & Wang, H. Oxidative Stress in Pancreatic Beta Cell Regeneration. *Oxidative Medicine and Cellular Longevity* **2017**, 1-9 (2017).
64. Sun, J. *et al.* Proinsulin misfolding and endoplasmic reticulum stress during the development and progression of diabetes. *Mol Aspects Med* **42**, 105-118 (2015).
65. Stumvoll, M., Goldstein, B.J. & van Haeften, T.W. Type 2 diabetes: principles of pathogenesis and therapy. *Lancet* **365**, 1333-1346 (2005).
66. Godoy-Matos, A.F. The role of glucagon on type 2 diabetes at a glance. *Diabetology & Metabolic Syndrome* **6**, 91 (2014).
67. Wewer Albrechtsen, N.J., Kuhre, R.E., Pedersen, J., Knop, F.K. & Holst, J.J. The biology of glucagon and the consequences of hyperglucagonemia. *Biomark Med* **10**, 1141-1151 (2016).
68. Brown, A.E. & Walker, M. Genetics of Insulin Resistance and the Metabolic Syndrome. *Curr Cardiol Rep* **18**, 75-75 (2016).
69. Mayans, S. *et al.* TCF7L2 polymorphisms are associated with type 2 diabetes in northern Sweden. *European Journal of Human Genetics* **15**, 342-346 (2007).
70. Huang, Z.-Q., Liao, Y.-Q., Huang, R.-Z., Chen, J.-P. & Sun, H.-L. Possible role of TCF7L2 in the pathogenesis of type 2 diabetes mellitus. *Biotechnology & Biotechnological Equipment* **32**, 830-834 (2018).
71. Cheung, N., Mitchell, P. & Wong, T.Y. Diabetic retinopathy. *Lancet* **376**, 124-136 (2010).
72. American-Diabetes-Association 2. Classification and Diagnosis of Diabetes: Standards of Medical Care in Diabetes - 2020. *Diabetes Care* **43**, S14-S31 (2020).
73. Nyaga, D.M., Vickers, M.H., Jefferies, C., Perry, J.K. & O'Sullivan, J.M. The genetic architecture of type 1 diabetes mellitus. *Mol Cell Endocrinol* **477**, 70-80 (2018).
74. Atkinson, M.A., Eisenbarth, G.S. & Michels, A.W. Type 1 diabetes. *Lancet* **383**, 69-82 (2014).
75. Del Prato, S. Loss of early insulin secretion leads to postprandial hyperglycaemia. *Diabetologia* **46**, M2-M8 (2003).
76. Zaharia, O.P. *et al.* Risk of diabetes-associated diseases in subgroups of patients with recent-onset diabetes: a 5-year follow-up study. *The Lancet Diabetes & Endocrinology* **7**, 684-694 (2019).
77. Plows, J.F., Stanley, J.L., Baker, P.N., Reynolds, C.M. & Vickers, M.H. The Pathophysiology of Gestational Diabetes Mellitus. *International journal of molecular sciences* **19**, 3342 (2018).
78. Welters, A., and Lammert, E Diabetes Mellitus. In Metabolism of Human Diseases. E. Lammert, and M. Zeeb, eds. (Springer-Verlag Wien), pp. 163-169. (2014).
79. Kahn, S.E., Cooper, M.E. & Del Prato, S. Pathophysiology and treatment of type 2 diabetes: perspectives on the past, present, and future. *The Lancet* **383**, 1068-1083 (2014).
80. Bailey, C.J., Tahrani, A.A. & Barnett, A.H. Future glucose-lowering drugs for type 2 diabetes. *The Lancet Diabetes & Endocrinology* **4**, 350-359 (2016).
81. Sandler, S. & Andersson, A. Islet implantation into diabetic mice with pancreatic insulitis. *Acta Pathol Microbiol Scand A* **89**, 107-112 (1981).
82. El-Gohary, Y. *et al.* Three-dimensional analysis of the islet vasculature. *Anat Rec (Hoboken)* **295**, 1473-1481 (2012).
83. Konstantinova, I. & Lammert, E. Microvascular development: learning from pancreatic islets. *Bioessays* **26**, 1069-1075 (2004).
84. Jansson, L. *et al.* Pancreatic islet blood flow and its measurement. *Upsala Journal of Medical Sciences* **121**, 81-95 (2016).
85. Jansson, L. & Carlsson, P.O. Graft vascular function after transplantation of pancreatic islets. *Diabetologia* **45**, 749-763 (2002).
86. Gan, W.J. *et al.* Cell polarity defines three distinct domains in pancreatic β-cells. *Journal of Cell Science* **130**, 143-151 (2017).
87. Bonner-Weir, S. Morphological evidence for pancreatic polarity of beta-cell within islets of Langerhans. *Diabetes* **37**, 616-621 (1988).
88. Henderson, J.R. & Moss, M.C. A morphometric study of the endocrine and exocrine capillaries of the pancreas. *Q J Exp Physiol* **70**, 347-356 (1985).
89. Meyer, H.H., Vetterlein, F., Schmidt, G. & Hasselblatt, A. Measurement of blood flow in pancreatic islets of the rat: effect of isoproterenol and norepinephrine. *Am J Physiol* **242**, E298-E304 (1982).

90. Bonner-Weir, S. & Orci, L. New perspectives on the microvasculature of the islets of Langerhans in the rat. *Diabetes* **31**, 883-889 (1982).
91. Brissova, M. *et al.* Pancreatic islet production of vascular endothelial growth factor-a is essential for islet vascularization, revascularization, and function. *Diabetes* **55**, 2974-2985 (2006).
92. Lammert, E. *et al.* Role of VEGF-A in vascularization of pancreatic islets. *Current biology : CB* **13**, 1070-1074 (2003).
93. Hogan, M.F. & Hull, R.L. The islet endothelial cell: a novel contributor to beta cell secretory dysfunction in diabetes. *Diabetologia* **60**, 952-959 (2017).
94. Nikolova, G., Strilic, B. & Lammert, E. The vascular niche and its basement membrane. *Trends Cell Biol* **17**, 19-25 (2007).
95. Nikolova, G. *et al.* The Vascular Basement Membrane: A Niche for Insulin Gene Expression and β Cell Proliferation. **10**, 397-405 (2006).
96. Johansson, M., Mattsson, G., Andersson, A., Jansson, L. & Carlsson, P.-O. Islet endothelial cells and pancreatic beta-cell proliferation: studies in vitro and during pregnancy in adult rats. *Endocrinology* **147**, 2315-2324 (2006).
97. Almaça, J., Weitz, J., Rodriguez-Diaz, R., Pereira, E. & Caicedo, A. The Pericyte of the Pancreatic Islet Regulates Capillary Diameter and Local Blood Flow. *Cell Metabolism* **27**, 630-644.e634 (2018).
98. Armulik, A., Abramsson, A. & Betsholtz, C. Endothelial/pericyte interactions. *Circulation research* **97**, 512-523 (2005).
99. Lindahl, P., Johansson, B.R., Levéen, P. & Betsholtz, C. Pericyte loss and microaneurysm formation in PDGF-B-deficient mice. *Science (New York, N.Y.)* **277**, 242-245 (1997).
100. von Tell, D., Armulik, A. & Betsholtz, C. Pericytes and vascular stability. *Experimental cell research* **312**, 623-629 (2006).
101. Epshtein, A. *et al.* Neonatal pancreatic pericytes support β-cell proliferation. *Mol Metab* **6**, 1330-1338 (2017).
102. Sasson, A. *et al.* Islet Pericytes Are Required for β-Cell Maturity. *Diabetes* **65**, 3008-3014 (2016).
103. Lammert, E., Cleaver, O. & Melton, D. Induction of pancreatic differentiation by signals from blood vessels. *Science (New York, N.Y.)* **294**, 564-567 (2001).
104. Reinert, R.B. *et al.* Vascular Endothelial Growth Factor-A and Islet Vascularization Are Necessary in Developing, but Not Adult, Pancreatic Islets. *Diabetes* **62**, 4154-4164 (2013).
105. Gerhardt, H. VEGF and endothelial guidance in angiogenic sprouting. *Organogenesis* **4**, 241-246 (2008).
106. Kamba, T. *et al.* VEGF-dependent plasticity of fenestrated capillaries in the normal adult microvasculature. *Am J Physiol Heart Circ Physiol* **290**, H560-576 (2006).
107. Jiménez, B. *et al.* Signals leading to apoptosis-dependent inhibition of neovascularization by thrombospondin-1. *Nature medicine* **6**, 41-48 (2000).
108. Olerud, J., Johansson, M., Lawler, J., Welsh, N. & Carlsson, P.O. Improved Vascular Engraftment and Graft Function After Inhibition of the Angiostatic Factor Thrombospondin-1 in Mouse Pancreatic Islets. *Diabetes* **57**, 1870-1877 (2008).
109. Carlsson, P.-O., Jansson, L., Östenson, C.-G. & Källskog, Ö. Islet Capillary Blood Pressure Increase Mediated by Hyperglycemia in NIDDM GK Rats. *Diabetes* **46**, 947 (1997).
110. Dai, C. *et al.* Pancreatic Islet Vasculature Adapts to Insulin Resistance Through Dilation and Not Angiogenesis. *Diabetes* **62**, 4144-4153 (2013).
111. Nakamura, M. *et al.* The endocrine pancreas of spontaneously diabetic mice: microangiopathy as revealed by transmission electron microscopy. *Diabetes Res Clin Pract* **30**, 89-100 (1995).
112. Hellström, M. *et al.* Lack of pericytes leads to endothelial hyperplasia and abnormal vascular morphogenesis. *The Journal of cell biology* **153**, 543-553 (2001).
113. Li, X. *et al.* Islet Microvasculature in Islet Hyperplasia and Failure in a Model of Type 2 Diabetes. *Diabetes* **55**, 2965-2973 (2006).
114. Lacraz, G. *et al.* Islet Endothelial Activation and Oxidative Stress Gene Expression Is Reduced by IL-1Ra Treatment in the Type 2 Diabetic GK Rat. *PLoS ONE* **4**, e6963 (2009).
115. Theocharis, A.D., Skandalis, S.S., Gialeli, C. & Karamanos, N.K. Extracellular matrix structure. *Adv Drug Deliv Rev* **97**, 4-27 (2016).
116. Kuehn, C., Vermette, P. & Fülöp, T. Cross talk between the extracellular matrix and the immune system in the context of endocrine pancreatic islet transplantation. A review article. *Pathol Biol* **62**, 67-78 (2014).
117. Rozario, T. & DeSimone, D.W. The extracellular matrix in development and morphogenesis: a dynamic view. *Developmental biology* **341**, 126-140 (2010).

118. Arous, C. & Wehrle-Haller, B. Role and impact of the extracellular matrix on integrin-mediated pancreatic β-cell functions. *Biol Cell* **109**, 223-237 (2017).
119. Llacua, L.A., Faas, M.M. & De Vos, P. Extracellular matrix molecules and their potential contribution to the function of transplanted pancreatic islets. *Diabetologia* **61**, 1261-1272 (2018).
120. Kaido, T. *et al.* Impact of defined matrix interactions on insulin production by cultured human beta-cells: effect on insulin content, secretion, and gene transcription. *Diabetes* **55**, 2723-2729 (2006).
121. Kaido, T., Yebra, M., Cirulli, V. & Montgomery, A.M. Regulation of human beta-cell adhesion, motility, and insulin secretion by collagen IV and its receptor alpha1beta1. *The Journal of biological chemistry* **279**, 53762-53769 (2004).
122. Pankov, R. Fibronectin at a glance. *Journal of Cell Science* **115**, 3861-3863 (2002).
123. Hadavi, E. *et al.* Fibronectin and Collagen IV microcontact printing can improve insulin secretion by INS1E cells. *Tissue Engineering Part C: Methods* (2018).
124. Aumailley, M. *et al.* A simplified laminin nomenclature. *Matrix Biology* **24**, 326-332 (2005).
125. Banerjee, M., Virtanen, I., Palgi, J., Korsgren, O. & Otonkoski, T. Proliferation and plasticity of human beta cells on physiologically occurring laminin isoforms. *Mol Cell Endocrinol* **355**, 78-86 (2012).
126. Kragl, M. & Lammert, E. Basement membrane in pancreatic islet function. *Adv Exp Med Biol* **654**, 217-234 (2010).
127. Diaferia, G.R. *et al.* beta1 integrin is a crucial regulator of pancreatic beta-cell expansion. *Development* **140**, 3360-3372 (2013).
128. Hynes, R.O. Cell-matrix adhesion in vascular development. *Journal of Thrombosis and Haemostasis* **5**, 32-40 (2007).
129. Saleem, S. *et al.* β1 integrin/FAK/ERK signalling pathway is essential for human fetal islet cell differentiation and survival. *The Journal of Pathology* **219**, 182-192 (2009).
130. Yebra, M. *et al.* Endothelium-derived Netrin-4 supports pancreatic epithelial cell adhesion and differentiation through integrins alpha2beta1 and alpha3beta1. *PLoS One* **6**, e22750 (2011).
131. Klapholz, B. *et al.* Alternative mechanisms for talin to mediate integrin function. *Current biology : CB* **25**, 847-857 (2015).
132. Legate, K.R., Montañez, E., Kudlacek, O. & Fässler, R. ILK, PINCH and parvin: the tIPP of integrin signalling. *Nature Reviews Molecular Cell Biology* **7**, 20-31 (2006).
133. Gan, W.J. *et al.* Local Integrin Activation in Pancreatic β Cells Targets Insulin Secretion to the Vasculature. *Cell reports* **24**, 2819-2826.e2813 (2018).
134. Schiller, H.B., Friedel, C.C., Boulegue, C. & Fässler, R. Quantitative proteomics of the integrin adhesome show a myosin II-dependent recruitment of LIM domain proteins. *EMBO Rep* **12**, 259-266 (2011).
135. Hannigan, G.E. *et al.* Regulation of cell adhesion and anchorage-dependent growth by a new beta 1-integrin-linked protein kinase. *Nature* **379**, 91-96 (1996).
136. Delon, I. & Brown, N.H. Integrins and the actin cytoskeleton. *Curr Opin Cell Biol* **19**, 43-50 (2007).
137. Sakai, T. Integrin-linked kinase (ILK) is required for polarizing the epiblast, cell adhesion, and controlling actin accumulation. *Genes & Development* **17**, 926-940 (2003).
138. Fässler, R. & Meyer, M. Consequences of lack of beta 1 integrin gene expression in mice. *Genes & Development* **9**, 1896-1908 (1995).
139. Stephens, L.E. *et al.* Deletion of beta 1 integrins in mice results in inner cell mass failure and peri-implantation lethality. *Genes & Development* **9**, 1883-1895 (1995).
140. Zervas, C.G., Gregory, S.L. & Brown, N.H. Drosophila Integrin-Linked Kinase Is Required at Sites of Integrin Adhesion to Link the Cytoskeleton to the Plasma Membrane. *The Journal of Cell Biology* **152**, 1007-1018 (2001).
141. Mackinnon, A.C., Qadota, H., Norman, K.R., Moerman, D.G. & Williams, B.D. C. elegans PAT-4/ILK Functions as an Adaptor Protein within Integrin Adhesion Complexes. *Curr Biol* **12**, 787-797 (2002).
142. Lange, A. *et al.* Integrin-linked kinase is an adaptor with essential functions during mouse development. *Nature* **461**, 1002-1006 (2009).
143. Fukuda, K., Gupta, S., Chen, K., Wu, C. & Qin, J. The Pseudoactive Site of ILK Is Essential for Its Binding to α-Parvin and Localization to Focal Adhesions. *Mol Cell* **36**, 819-830 (2009).
144. Yang, Y. *et al.* Structural Basis of Focal Adhesion Localization of LIM-only Adaptor PINCH by Integrin-linked Kinase. *J Biol Chem* **284**, 5836-5844 (2009).
145. Chiswell, B.P., Zhang, R., Murphy, J.W., Boggon, T.J. & Calderwood, D.A. The structural basis of integrin-linked kinase–PINCH interactions. *Proceedings of the National Academy of Sciences* **105**, 20677-20682 (2008).

146. Liang, X. *et al.* PINCH1 Plays an Essential Role in Early Murine Embryonic Development but Is Dispensable in Ventricular Cardiomyocytes. *Mol Cell Biol* **25**, 3056-3062 (2005).
147. Li, S. *et al.* PINCH1 regulates cell-matrix and cell-cell adhesions, cell polarity and cell survival during the peri-implantation stage. *Journal of Cell Science* **118**, 2913-2921 (2005).
148. Stanchi, F. *et al.* Consequences of loss of PINCH2 expression in mice. *Journal of Cell Science* **118**, 5899-5910 (2005).
149. Tu, Y., Huang, Y., Zhang, Y., Hua, Y. & Wu, C. A New Focal Adhesion Protein That Interacts with Integrin-Linked Kinase and Regulates Cell Adhesion and Spreading. *The Journal of Cell Biology* **153**, 585-598 (2001).
150. Nikolopoulos, S.N. & Turner, C.E. Actopaxin, a new focal adhesion protein that binds paxillin LD motifs and actin and regulates cell adhesion. *The Journal of cell biology* **151**, 1435-1448 (2000).
151. Montanez, E., Wickström, S.A., Altstätter, J., Chu, H. & Fässler, R. α-parvin controls vascular mural cell recruitment to vessel wall by regulating RhoA/ROCK signalling. *EMBO J* **28**, 3132-3144 (2009).
152. Kogata, N., Tribe, R.M., Fassler, R., Way, M. & Adams, R.H. Integrin-linked kinase controls vascular wall formation by negatively regulating Rho/ROCK-mediated vascular smooth muscle cell contraction. *Genes Dev* **23**, 2278-2283 (2009).
153. Assi, K. *et al.* Integrin-linked kinase regulates cell proliferation and tumour growth in murine colitis-associated carcinogenesis. *Gut* **57**, 931-940 (2008).
154. Potente, M., Gerhardt, H. & Carmeliet, P. Basic and therapeutic aspects of angiogenesis. *Cell* **146**, 873-887 (2011).
155. Conway, E.M., Collen, D. & Carmeliet, P. Molecular mechanisms of blood vessel growth. *Cardiovasc Res* **49**, 507-521 (2001).
156. Gerhardt, H. & Betsholtz, C. How do endothelial cells orientate? *EXS*, 3-15 (2005).
157. Herbert, S.P. & Stainier, D.Y.R. Molecular control of endothelial cell behaviour during blood vessel morphogenesis. *Nature reviews. Molecular cell biology* **12**, 551-564 (2011).
158. Armulik, A. *et al.* Pericytes regulate the blood-brain barrier. *Nature* **468**, 557-561 (2010).
159. Mishra, A. *et al.* Imaging pericytes and capillary diameter in brain slices and isolated retinae. *Nature protocols* **9**, 323-336 (2014).
160. Armulik, A., Genové, G. & Betsholtz, C. Pericytes: developmental, physiological, and pathological perspectives, problems, and promises. *Developmental cell* **21**, 193-215 (2011).
161. Hammes, H.-P. *et al.* Angiopoietin-2 causes pericyte dropout in the normal retina: evidence for involvement in diabetic retinopathy. *Diabetes* **53**, 1104-1110 (2004).
162. Pfister, F. *et al.* Pericyte migration: a novel mechanism of pericyte loss in experimental diabetic retinopathy. *Diabetes* **57**, 2495-2502 (2008).
163. Gerhardt, H. & Betsholtz, C. Endothelial-pericyte interactions in angiogenesis. *Cell Tissue Res* **314**, 15-23 (2003).
164. Raza, A., Franklin, M.J. & Dudek, A.Z. Pericytes and vessel maturation during tumor angiogenesis and metastasis. *Am J Hematol* **85**, 593-598 (2010).
165. Beltramo, E. & Porta, M. Pericyte loss in diabetic retinopathy: mechanisms and consequences. *Curr Med Chem* **20**, 3218-3225 (2013).
166. Hammes, H.-P., Feng, Y., Pfister, F. & Brownlee, M. Diabetic retinopathy: targeting vasoregression. *Diabetes* **60**, 9-16 (2011).
167. Hall, C.N. *et al.* Capillary pericytes regulate cerebral blood flow in health and disease. *Nature* **508**, 55-60 (2014).
168. Ribatti, D., Nico, B. & Crivellato, E. The role of pericytes in angiogenesis. *Int J Dev Biol* **55**, 261-268 (2011).
169. Nakatsu, M.N. *et al.* Angiogenic sprouting and capillary lumen formation modeled by human umbilical vein endothelial cells (HUVEC) in fibrin gels: the role of fibroblasts and Angiopoietin-1. *Microvasc Res* **66**, 102-112 (2003).
170. Nakatsu, M.N., Davis, J. & Hughes, C.C.W. Optimized fibrin gel bead assay for the study of angiogenesis. *J Vis Exp*, 186-186 (2007).
171. Nakatsu, M.N. & Hughes, C.C.W. An optimized three-dimensional in vitro model for the analysis of angiogenesis. *Methods Enzymol* **443**, 65-82 (2008).
172. Zudaire, E., Gambardella, L., Kurcz, C. & Vermeren, S. A computational tool for quantitative analysis of vascular networks. *PloS one* **6**, e27385-e27385 (2011).
173. Boettcher, M., Gloe, T. & de Wit, C. Semiautomatic quantification of angiogenesis. *The Journal of surgical research* **162**, 132-139 (2010).
174. Mendel, D.B. *et al.* The angiogenesis inhibitor SU5416 has long-lasting effects on vascular endothelial growth factor receptor phosphorylation and function. *Clin Cancer Res* **6**, 4848-4858 (2000).

175. Strilić, B. *et al.* The molecular basis of vascular lumen formation in the developing mouse aorta. *Developmental cell* **17**, 505-515 (2009).
176. Schulz, B. *et al.* ADAM10 regulates endothelial permeability and T-Cell transmigration by proteolysis of vascular endothelial cadherin. *Circulation research* **102**, 1192-1201 (2008).
177. Namkoong, S. *et al.* Forskolin increases angiogenesis through the coordinated cross-talk of PKA-dependent VEGF expression and Epac-mediated PI3K/Akt/eNOS signaling. *Cell Signal* **21**, 906-915 (2009).
178. Strilić, B. *et al.* Electrostatic cell-surface repulsion initiates lumen formation in developing blood vessels. *Current biology : CB* **20**, 2003-2009 (2010).
179. Kachgal, S. & Putnam, A.J. Mesenchymal stem cells from adipose and bone marrow promote angiogenesis via distinct cytokine and protease expression mechanisms. *Angiogenesis* **14**, 47-59 (2011).
180. van Meeteren, L.A. *et al.* Anti-human activin receptor-like kinase 1 (ALK1) antibody attenuates bone morphogenetic protein 9 (BMP9)-induced ALK1 signaling and interferes with endothelial cell sprouting. *The Journal of biological chemistry* **287**, 18551-18561 (2012).
181. Wilson, C.W. *et al.* Rasip1 regulates vertebrate vascular endothelial junction stability through Epac1-Rap1 signaling. *Blood* **122**, 3678-3690 (2013).
182. Wimmer, R., Cseh, B., Maier, B., Scherrer, K. & Baccarini, M. Angiogenic sprouting requires the fine tuning of endothelial cell cohesion by the Raf-1/Rok-α complex. *Developmental cell* **22**, 158-171 (2012).
183. Zheng, W. *et al.* Notch restricts lymphatic vessel sprouting induced by vascular endothelial growth factor. *Blood* **118**, 1154-1162 (2011).
184. Liang, C.-C., Park, A.Y. & Guan, J.-L. In vitro scratch assay: a convenient and inexpensive method for analysis of cell migration in vitro. *Nature protocols* **2**, 329-333 (2007).
185. Arganda-Carreras, I., Fernández-González, R., Muñoz-Barrutia, A. & Ortiz-De-Solorzano, C. 3D reconstruction of histological sections: Application to mammary gland tissue. *Microsc Res Tech* **73**, 1019-1029 (2010).
186. Bouïs, D., Hospers, G.A., Meijer, C., Molema, G. & Mulder, N.H. Endothelium in vitro: a review of human vascular endothelial cell lines for blood vessel-related research. *Angiogenesis* **4**, 91-102 (2001).
187. Shepro, D. & Morel, N.M. Pericyte physiology. *FASEB journal : official publication of the Federation of American Societies for Experimental Biology* **7**, 1031-1038 (1993).
188. Preibisch, S., Saalfeld, S. & Tomancak, P. Globally optimal stitching of tiled 3D microscopic image acquisitions. *Bioinformatics* **25**, 1463-1465 (2009).
189. Schindelin, J. *et al.* Fiji: an open-source platform for biological-image analysis. *Nature methods* **9**, 676-682 (2012).
190. Meadows, S.M. & Cleaver, O. Vascular patterning: coordinated signals keep blood vessels on track. *Curr Opin Genet Dev* **32C**, 86-91 (2015).
191. Claesson-Welsh, L. & Welsh, M. VEGFA and tumour angiogenesis. *Journal of internal medicine* **273**, 114-127 (2013).
192. Richards, O.C., Raines, S.M. & Attie, A.D. The role of blood vessels, endothelial cells, and vascular pericytes in insulin secretion and peripheral insulin action. *Endocr Rev* **31**, 343-363 (2010).
193. Rondas, D., Tomas, A., Soto-Ribeiro, M., Wehrle-Haller, B. & Halban, P.A. Novel mechanistic link between focal adhesion remodeling and glucose-stimulated insulin secretion. *J Biol Chem* **287**, 2423-2436 (2011).
194. Kren, A. *et al.* Increased tumor cell dissemination and cellular senescence in the absence of beta1-integrin function. *EMBO J* **26**, 2832-2842 (2007).
195. Riopel, M. *et al.* Conditional beta1-integrin-deficient mice display impaired pancreatic beta cell function. *J Pathol* **224**, 45-55 (2011).
196. Shih, H.P., Panlasigui, D., Cirulli, V. & Sander, M. ECM Signaling Regulates Collective Cellular Dynamics to Control Pancreas Branching Morphogenesis. *Cell reports* **14**, 169-179 (2016).
197. Johansson, A. *et al.* Endothelial cell signalling supports pancreatic beta cell function in the rat. *Diabetologia* **52**, 2385-2394 (2009).
198. Thorens, B. *et al.* Ins1 Cre knock-in mice for beta cell-specific gene recombination. *Diabetologia* **58**, 558-565 (2015).
199. Yang, Y. *et al.* Anti-VEGF- and anti-VEGF receptor-induced vascular alteration in mouse healthy tissues. *Proc Natl Acad Sci U S A* **110**, 12018-12023 (2013).
200. Tan, C. *et al.* Regulation of tumor angiogenesis by integrin-linked kinase (ILK). *Cancer Cell* **5**, 79-90 (2004).

201. Wani, A.A., Jafarnejad, S.M., Zhou, J. & Li, G. Integrin-linked kinase regulates melanoma angiogenesis by activating NF-kappaB/interleukin-6 signaling pathway. *Oncogene* **30**, 2778-2788 (2011).
202. Fagiani, E., Lorentz, P., Kopfstein, L. & Christofori, G. Angiopoietin-1 and -2 exert antagonistic functions in tumor angiogenesis, yet both induce lymphangiogenesis. *Cancer Res* **71**, 5717-5727 (2011).
203. Calderari, S. *et al.* Angiopoietin 2 alters pancreatic vascularization in diabetic conditions. *PLoS One* **7**, e29438 (2012).
204. Cai, Q. *et al.* Enhanced expression of VEGF-A in beta cells increases endothelial cell number but impairs islet morphogenesis and beta cell proliferation. *Dev Biol* **367**, 40-54 (2012).
205. Xu, J. *et al.* The evolution of alternative splicing exons in vascular endothelial growth factor A. *Gene* **487**, 143-150 (2011).
206. Gkretsi, V. *et al.* Liver-specific ablation of integrin-linked kinase in mice results in abnormal histology, enhanced cell proliferation, and hepatomegaly. *Hepatology* **48**, 1932-1941 (2008).
207. Georgia, S. & Bhushan, A. Beta cell replication is the primary mechanism for maintaining postnatal beta cell mass. *J Clin Invest* **114**, 963-968 (2004).
208. Gliem, M. *et al.* Expression of classical cadherins in the cerebellar anlage: quantitative and functional aspects. *Mol Cell Neurosci* **33**, 447-458 (2006).
209. Krieg, M. *et al.* Tensile forces govern germ-layer organization in zebrafish. *Nat Cell Biol* **10**, 429-436 (2008).
210. Reintsch, W.E., Habring-Mueller, A., Wang, R.W., Schohl, A. & Fagotto, F. beta-Catenin controls cell sorting at the notochord-somite boundary independently of cadherin-mediated adhesion. *J Cell Biol* **170**, 675-686 (2005).
211. Steinberg, M.S. Reconstruction of tissues by dissociated cells. Some morphogenetic tissue movements and the sorting out of embryonic cells may have a common explanation. *Science* **141**, 401-408 (1963).
212. Steinberg, M.S. Differential adhesion in morphogenesis: a modern view. *Curr Opin Genet Dev* **17**, 281-286 (2007).
213. Friedrich, E.B. *et al.* Integrin-linked kinase regulates endothelial cell survival and vascular development. *Mol Cell Biol* **24**, 8134-8144 (2004).
214. Grashoff, C., Aszodi, A., Sakai, T., Hunziker, E.B. & Fassler, R. Integrin-linked kinase regulates chondrocyte shape and proliferation. *EMBO Rep* **4**, 432-438 (2003).
215. Pereira, J.A. *et al.* Integrin-linked kinase is required for radial sorting of axons and Schwann cell remyelination in the peripheral nervous system. *J Cell Biol* **185**, 147-161 (2009).
216. Terpstra, L. *et al.* Reduced chondrocyte proliferation and chondrodysplasia in mice lacking the integrin-linked kinase in chondrocytes. *J Cell Biol* **162**, 139-148 (2003).
217. Mancuso, M.R. *et al.* Rapid vascular regrowth in tumors after reversal of VEGF inhibition. *J Clin Invest* **116**, 2610-2621 (2006).
218. Beckmann, J., Schubert, R., Chiquet-Ehrismann, R. & Muller, D.J. Deciphering teneurin domains that facilitate cellular recognition, cell-cell adhesion, and neurite outgrowth using atomic force microscopy-based single-cell force spectroscopy. *Nano Lett* **13**, 2937-2946 (2013).
219. Benoit, M., Gabriel, D., Gerisch, G. & Gaub, H.E. Discrete interactions in cell adhesion measured by single-molecule force spectroscopy. *Nat Cell Biol* **2**, 313-317 (2000).
220. Muller, D.J., Helenius, J., Alsteens, D. & Dufrene, Y.F. Force probing surfaces of living cells to molecular resolution. *Nat Chem Biol* **5**, 383-390 (2009).
221. Kucera, T. & Lammert, E. Ancestral vascular tube formation and its adoption by tumors. *Biol Chem* **390**, 985-994 (2009).
222. Miyazaki, J. *et al.* Establishment of a pancreatic beta cell line that retains glucose-inducible insulin secretion: special reference to expression of glucose transporter isoforms. *Endocrinology* **127**, 126-132 (1990).
223. Harris, A.K. Is Cell sorting caused by differences in the work of intercellular adhesion? A critique of the Steinberg hypothesis. *J Theor Biol* **61**, 267-285 (1976).
224. Youssef, J., Nurse, A.K., Freund, L.B. & Morgan, J.R. Quantification of the forces driving self-assembly of three-dimensional microtissues. *Proc Natl Acad Sci U S A* **108**, 6993-6998 (2011).
225. Maitre, J.L. *et al.* Adhesion functions in cell sorting by mechanically coupling the cortices of adhering cells. *Science* **338**, 253-256 (2012).
226. Amack, J.D. & Manning, M.L. Knowing the boundaries: extending the differential adhesion hypothesis in embryonic cell sorting. *Science* **338**, 212-215 (2012).
227. Stirbat, T.V. *et al.* Fine tuning of tissues' viscosity and surface tension through contractility suggests a new role for alpha-catenin. *PLoS One* **8**, e52554 (2013).

228. David, R. *et al.* Tissue cohesion and the mechanics of cell rearrangement. *Development* **141**, 3672-3682 (2014).
229. Brodland, G.W. & Chen, H.H. The mechanics of heterotypic cell aggregates: insights from computer simulations. *J Biomech Eng* **122**, 402-407 (2000).
230. Manning, M.L., Foty, R.A., Steinberg, M.S. & Schoetz, E.M. Coaction of intercellular adhesion and cortical tension specifies tissue surface tension. *Proc Natl Acad Sci U S A* **107**, 12517-12522 (2010).
231. Winklbauer, R. Cell adhesion strength from cortical tension - an integration of concepts. *J Cell Sci* **128**, 3687-3693 (2015).
232. Dai, J., Ting-Beall, H.P., Hochmuth, R.M., Sheetz, M.P. & Titus, M.A. Myosin I contributes to the generation of resting cortical tension. *Biophys J* **77**, 1168-1176 (1999).
233. Evans, E. & Yeung, A. Apparent viscosity and cortical tension of blood granulocytes determined by micropipet aspiration. *Biophys J* **56**, 151-160 (1989).
234. Thoumine, O., Cardoso, O. & Meister, J.J. Changes in the mechanical properties of fibroblasts during spreading: a micromanipulation study. *Eur Biophys J* **28**, 222-234 (1999).
235. Arous, C. & Halban, P.A. The skeleton in the closet: actin cytoskeletal remodeling in beta-cell function. *Am J Physiol Endocrinol Metab* **309**, E611-620 (2015).
236. Shin, J.W. *et al.* Contractile forces sustain and polarize hematopoiesis from stem and progenitor cells. *Cell Stem Cell* **14**, 81-93 (2014).
237. Barry, D.M. *et al.* Rasip1-Mediated Rho GTPase Signaling Regulates Blood Vessel Tubulogenesis via Nonmuscle Myosin II. *Circulation research* **119**, 810-826 (2016).
238. Swaminathan, V. *et al.* Mechanical stiffness grades metastatic potential in patient tumor cells and in cancer cell lines. *Cancer Res* **71**, 5075-5080 (2011).
239. Traister, A. *et al.* Integrin-linked kinase mediates force transduction in cardiomyocytes by modulating SERCA2a/PLN function. *Nature communications* **5**, 4533-4533 (2014).
240. Korn, C. *et al.* Endothelial cell-derived non-canonical Wnt ligands control vascular pruning in angiogenesis. *Development* **141**, 1757-1766 (2014).
241. Franco, C.A. *et al.* Dynamic endothelial cell rearrangements drive developmental vessel regression. *PLoS Biol* **13**, e1002125 (2015).
242. Engler, A.J., Sen, S., Sweeney, H.L. & Discher, D.E. Matrix elasticity directs stem cell lineage specification. *Cell* **126**, 677-689 (2006).
243. Plodinec, M. *et al.* The nanomechanical signature of breast cancer. *Nat Nanotechnol* **7**, 757-765 (2012).
244. Herrera, P.L. Adult insulin- and glucagon-producing cells differentiate from two independent cell lineages. *Development (Cambridge, England)* **127**, 2317-2322 (2000).
245. Yesil, P. *et al.* A new collagenase blend increases the number of islets isolated from mouse pancreas. *Islets* **1**, 185-190 (2009).
246. Chmelova, H. *et al.* Distinct roles of β-cell mass and function during type 1 diabetes onset and remission. *Diabetes* **64**, 2148-2160 (2015).
247. Speier, S. *et al.* Noninvasive high-resolution in vivo imaging of cell biology in the anterior chamber of the mouse eye. *Nature protocols* **3**, 1278-1286 (2008).
248. Spurr, A.R. A low-viscosity epoxy resin embedding medium for electron microscopy. *J Ultrastruct Res* **26**, 31-43 (1969).
249. Marrif, H.I. & Al-Sunousi, S.I. Pancreatic β Cell Mass Death. *Frontiers in Pharmacology* **7** (2016).
250. Wang, P. *et al.* A high-throughput chemical screen reveals that harmine-mediated inhibition of DYRK1A increases human pancreatic beta cell replication. *Nature medicine* **21**, 383-388 (2015).
251. Abdelfattah *et al.* Liver-Derived Systemic Factors Drive β Cell Hyperplasia in Insulin-Resistant States. *Cell Rep* **3**, 401-410 (2013).
252. Vikram, A. & Jena, G. S961, an insulin receptor antagonist causes hyperinsulinemia, insulin-resistance and depletion of energy stores in rats. *Biochem Biophys Res Commun* **398**, 260-265 (2010).
253. Schäffer, L. *et al.* A novel high-affinity peptide antagonist to the insulin receptor. *Biochem Biophys Res Commun* **376**, 380-383 (2008).
254. Fajardo, R.J., Karim, L., Calley, V.I. & Bouxsein, M.L. A Review of Rodent Models of Type 2 Diabetic Skeletal Fragility. *Journal of Bone and Mineral Research* **29**, 1025-1040 (2014).
255. Mosser, R.E. *et al.* High-fat diet-induced β-cell proliferation occurs prior to insulin resistance in C57Bl/6J male mice. *American journal of physiology. Endocrinology and metabolism* **308**, E573-E582 (2015).

256. Kleiner, S. *et al.* Mice harboring the human SLC30A8 R138X loss-of-function mutation have increased insulin secretory capacity. *Proceedings of the National Academy of Sciences* **115**, E7642-E7649 (2018).
257. Magnuson, M.A. & Osipovich, A.B. Pancreas-Specific Cre Driver Lines and Considerations for Their Prudent Use. *Cell Metabolism* **18**, 9-20 (2013).
258. Offield, M.F. *et al.* PDX-1 is required for pancreatic outgrowth and differentiation of the rostral duodenum. *Development (Cambridge, England)* **122**, 983-995 (1996).
259. Abraham, S., Kogata, N., Fässler, R. & Adams, R.H. Integrin β1 Subunit Controls Mural Cell Adhesion, Spreading, and Blood Vessel Wall Stability. *Circulation Research* **102**, 562-570 (2008).
260. Park, H. *et al.* Integrin-linked kinase controls retinal angiogenesis and is linked to Wnt signaling and exudative vitreoretinopathy. *Nature Communications* **10** (2019).
261. D'Hoker, J. *et al.* Conditional Hypovascularization and Hypoxia in Islets Do Not Overtly Influence Adult B-Cell Mass or Function. *Diabetes* **62**, 4165-4173 (2013).
262. Levitt, H.E. *et al.* Glucose stimulates human beta cell replication in vivo in islets transplanted into NOD-severe combined immunodeficiency (SCID) mice. *Diabetologia* **54**, 572-582 (2011).
263. Alonso, L.C. *et al.* Glucose infusion in mice: a new model to induce beta-cell replication. *Diabetes* **56**, 1792-1801 (2007).
264. Porat, S. *et al.* Control of pancreatic β cell regeneration by glucose metabolism. *Cell metabolism* **13**, 440-449 (2011).
265. Toyofuku, Y. *et al.* Normal islet vascularization is dispensable for expansion of beta-cell mass in response to high-fat diet induced insulin resistance. *Biochemical and Biophysical Research Communications* **383**, 303-307 (2009).
266. Qu, Y. *et al.* ILK promotes cell proliferation in breast cancer cells by activating the PI3K/Akt pathway. *Molecular Medicine Reports* **16**, 5036-5042 (2017).
267. Lorenz, L. *et al.* Mechanosensing by β1 integrin induces angiocrine signals for liver growth and survival. *Nature* **562**, 128-132 (2018).
268. Albini, A. & Benelli, R. The chemoinvasion assay: a method to assess tumor and endothelial cell invasion and its modulation. *Nature protocols* **2**, 504-511 (2007).
269. Bayless, K.J., Kwak, H.-I. & Su, S.-C. Investigating endothelial invasion and sprouting behavior in three-dimensional collagen matrices. *Nature protocols* **4**, 1888-1898 (2009).
270. Zeitlin, B.D., Dong, Z. & Nör, J.E. RAIN-Droplet: a novel 3D in vitro angiogenesis model. *Lab Invest* **92**, 988-998 (2012).
271. Arnaoutova, I. & Kleinman, H.K. In vitro angiogenesis: endothelial cell tube formation on gelled basement membrane extract. *Nature protocols* **5**, 628-635 (2010).
272. Korff, T. & Augustin, H.G. Tensional forces in fibrillar extracellular matrices control directional capillary sprouting. *Journal of cell science* **112**, 3249-3258 (1999).
273. Morgan, J.P. *et al.* Formation of microvascular networks in vitro. *Nature protocols* **8**, 1820-1836 (2013).
274. van der Meer, A.D., Orlova, V.V., ten Dijke, P., van den Berg, A. & Mummery, C.L. Three-dimensional co-cultures of human endothelial cells and embryonic stem cell-derived pericytes inside a microfluidic device. *Lab Chip* **13**, 3562-3568 (2013).
275. Kim, J.K. Hyperinsulinemic-euglycemic clamp to assess insulin sensitivity in vivo. *Methods Mol Biol* **560**, 221-238 (2009).

9 Supplementary information

9.1 Supplementary information of section 5.1

This section contains an overview of the supplementary information that accompanies the manuscript Eglinger et al. - “Quantitative assessment of angiogenesis and pericyte coverage in human cell-derived vascular sprouts”[1]. All additional files are available at: https://inflammregen.biomedcentral.com/articles/10.1186/s41232-016-0033-2

Additional file 1: Movie introducing the bead sprouting assay and our software analysis. (MOV 22013 kb)

Additional file 2: Movie demonstrating the analysis of human EC/ pericyte-derived vascular sprouts. (MOV 4946 kb)

Additional file 3: Step-by-step protocol for the pericyte sprouting assay. This protocol contains several options of performing the bead sprouting assay, e.g., with or without pericytes, in a glass-bottom dish or a 96-well plate format, and with different stainings. (DOCX 132 kb)

Additional file 4: ImageJ macro to create maximum intensity projections. ImageJ macro (ijm) format; open the file using ImageJ, e.g., by dragging onto the ImageJ main window. (IJM 1 kb)

Additional file 5: ImageJ macro to process image folders. ImageJ macro (ijm) format; open the file using ImageJ, e.g., by dragging onto the ImageJ main window. (IJM 1 kb)

Additional file 6: Table S1. List of compounds and concentrations used. The compounds were used at two concentrations, indicated in the columns 10 × IC50 and 100 × IC50, respectively. The values were chosen according to published values for the half maximal inhibitory concentrations of the inhibitors with respect to their target molecules *in vitro* or in accordance with literature using the respective compounds in a similar assay setup. Literature references for each compound are listed in the reference column. (DOCX 193 kb)

Additional file 7: Table S2. Results of a pilot screen for EC-derived vascular sprouts. Changes considered significant with a cut-off p value of $p < 0.05$ (two-sided one-sample t test compared to solvent control) are colored in red and green to indicate decrease and increase compared to controls, respectively. N = 3 assays with 8 wells per compound each. (PDF 66 kb).

Additional file 8: Table S3. Results of a pilot screen for EC/pericyte- derived vascular sprouts. Changes considered significant with a cut-off p value of $p < 0.05$ (two-sided one-sample t test compared to solvent control) are colored in red and green to indicate decrease and increase compared to controls, respectively. N = 3 assays with 8 wells per compound each. (PDF 67 kb)

Additional file 9: Table S4. Comparison of *in vitro* and *ex vivo* assays. Comparison of *in vitro* and *ex vivo* assays to study sprouting angiogenesis, EC migration, and pericyte coverage. The method presented here is highlighted in green. Symbols used are the following: +, possible/present; −, not possible/ not present; n.s., not shown. (DOCX 148 kb)

Additional file 10: Figure S1. Quantification of branching level. (a) Confocal micrograph (maximum intensity projection) of a sprouting vascular plexus growing from four microcarrier beads, stained for F-actin (green) and nuclei (red). (b) Result image showing bead (dark grey) and sprout (light grey) segmentation. (c) Result image showing the sprout skeletons; branch points have been highlighted in red. (d) The option to measure branching level (red box) is available in the configuration dialog. (e) Result table reporting the average number of branch points per sprout (avg n(branch points), red box). (PNG 375 kb)

9.2 Supplementary information of section 5.2

This section contains the supplementary information of the manuscript: Kragl et al. - "The biomechanical properties of an epithelial tissue determine the location of its vasculature"[2]. Supplementary movies are available at: http://www.nature.com/naturecommunications.

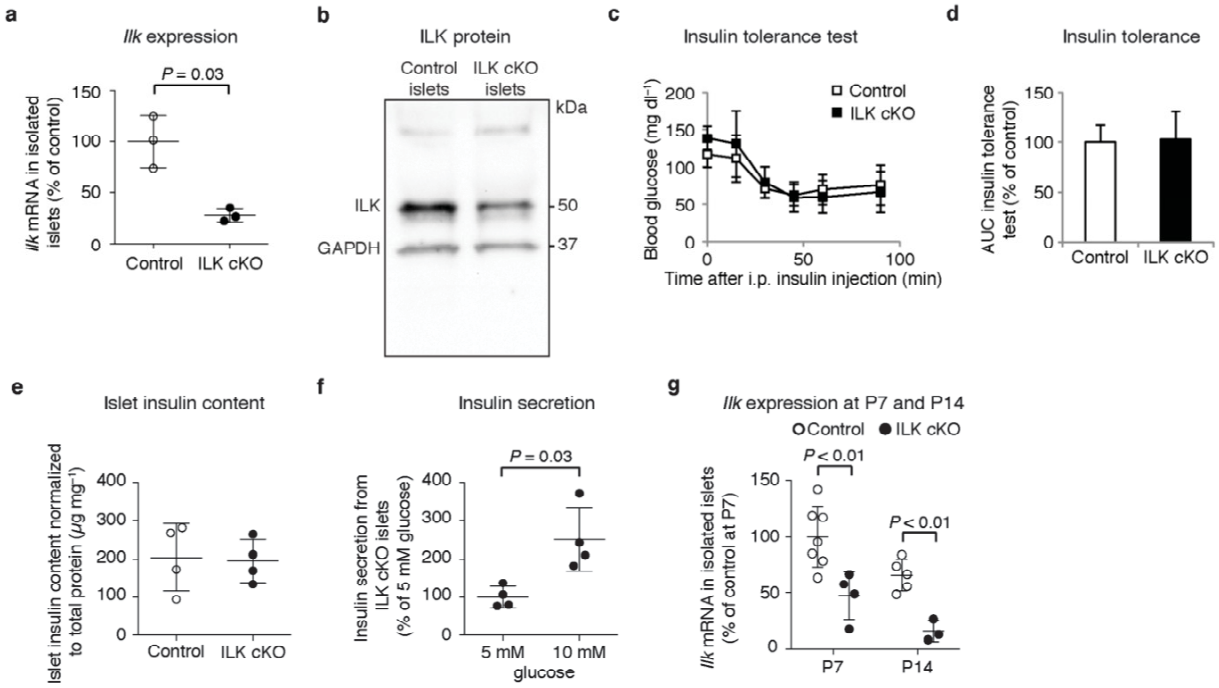

Supplementary Figure 1: ***Knockout efficiency and insulin tolerance of ILK cKO mice.*** (**a**) Quantification of relative Ilk mRNA expression in control versus ILK cKO islets. *N* = 3 animals per experimental group. (**b**) Western blot of ILK and GAPDH from control and ILK cKO islets. Around 90 islets from two mice were combined to gain lysates for western blot. (**c**) Blood glucose concentrations during an insulin tolerance test in male mice (12 weeks). Insulin (0.75 IU kg^{-1} body weight) was injected at 0 minutes. *N* = 7-8 mice per experimental group. (**d**) Area under curve of data shown in (**c**). (**e**) Insulin content from isolated control and ILK cKO islets. *N* = 4 islet batches per experimental condition (genotype). (**f**) Insulin secretion from isolated ILK cKO islets at 5 and 10 mM glucose. *N* = 4 islet batches per experimental condition (glucose concentration) each. (**g**) Quantification of relative *Ilk* mRNA expression in control versus ILK cKO islets of 7 (P7) and 14 (P14) day old mice. *N* = 3-7 animals per experimental group. Data are shown as mean values ± SD, **P* < 0.05 in an unpaired, two-sided Student's t-test with (**c**) Holm-Bonferroni correction.

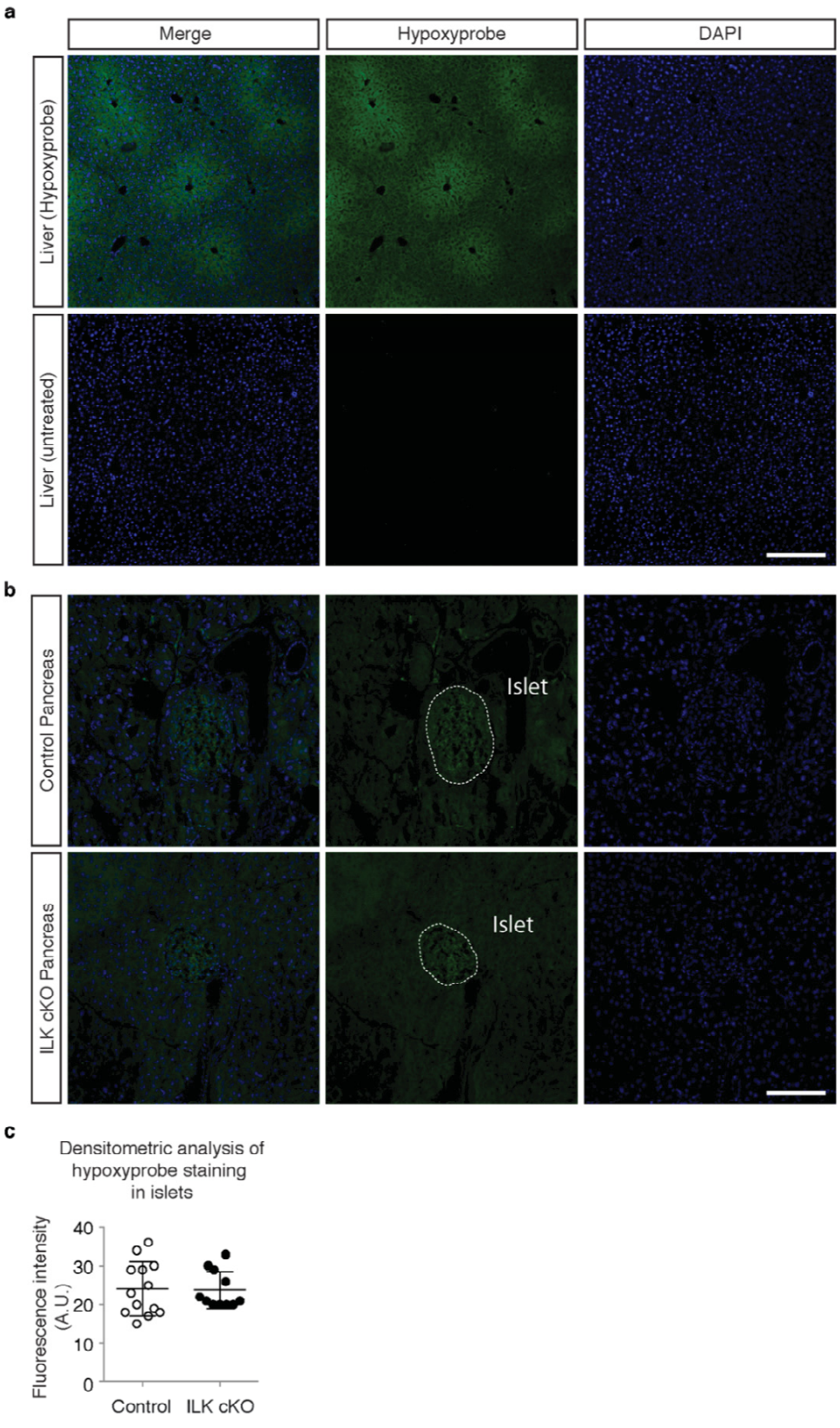

Supplementary Figure 2: ***Analysis of hypoxia in islets using pimonidazole (Hypoxyprobe*****).** LSM images of Hypoxyprobe (green) and DAPI nuclear staining (blue) in the (**a**) liver of pimonidazole injected (upper panels) and untreated animals (lower panels) and in the (**b**) pancreas of pimonidazole injected control (upper panels) and ILK cKO mice (lower panels). (**c**) Densitometric quantification of fluorescent intensity in sections of *N* = 13 control and 11 ILK cKO islets combined from two mice per genotype. Data are shown as mean values ± SD, **P* < 0.05 in an unpaired, two-sided Student's t-test. Scale bars, 100 µm (**a**); 200 µm (**b**).

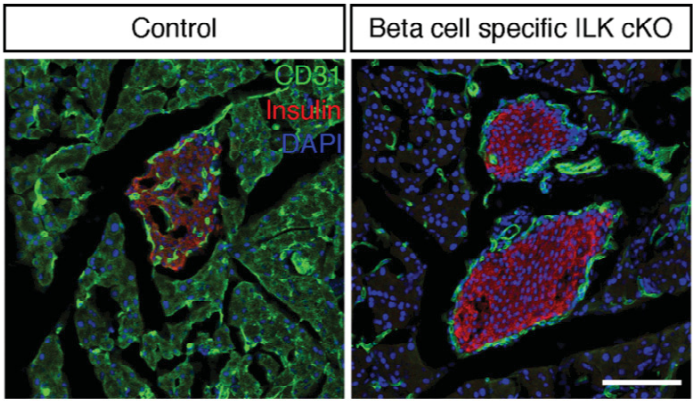

Supplementary Figure 3: ***Vascular phenotype in a beta cell specific knockout of Ilk.*** LSM images of immunofluorescence staining for cell nuclei (DAPI, blue), insulin (red) and CD31 (green) in pancreatic sections from insulin 1 *(Ins1)-Cre; Ilk*$^{loxP/loxP}$ mice and heterozygous control mice. Scale bar, 100 µm.

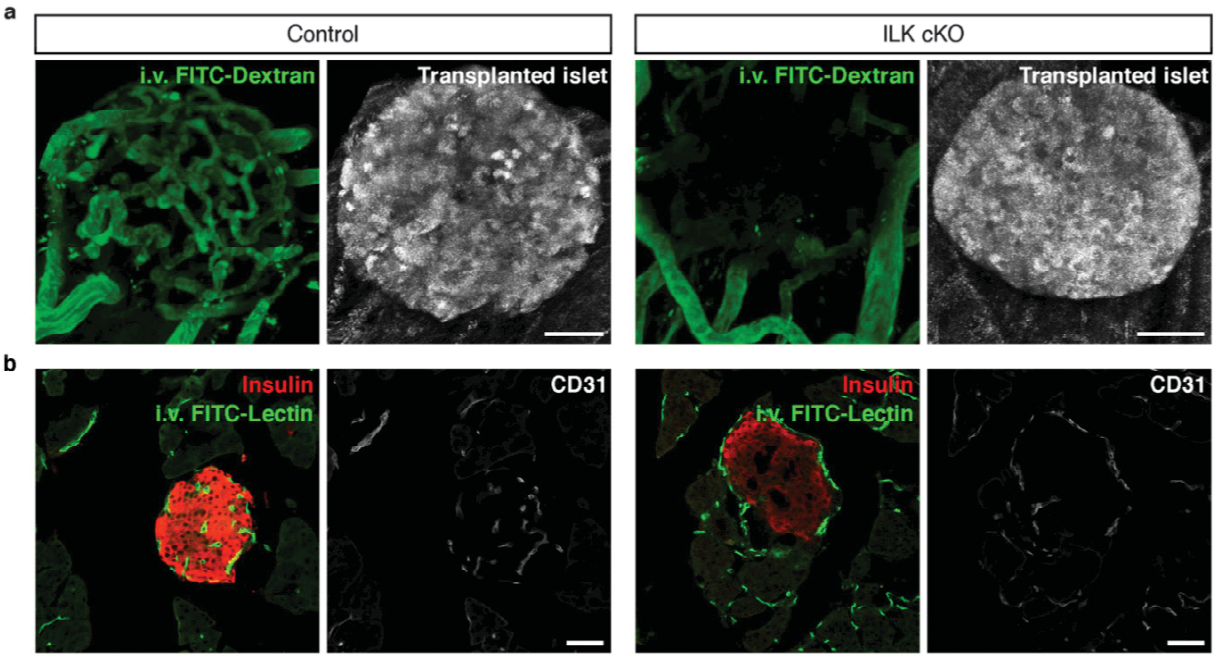

Supplementary Figure 4: ***Perfusion of ILK cKO islets after transplantation or in situ.*** (**a**) *In vivo* images of a control islet and an ILK cKO islet 28 days post transplantation into the anterior eye chamber. The islets are visualized by backscatter and an i.v. injected FITC-conjugated dextran (green) that highlights the perfused blood vessels. (**b**) LSM images showing immunofluorescence staining for insulin (red) of pancreatic sections from a control and an ILK cKO mouse that have been i.v. injected with a FITC-conjugated tomato lectin (green), indicating perfused blood vessels. Scale bars, 50 µm (**a**, **b**).

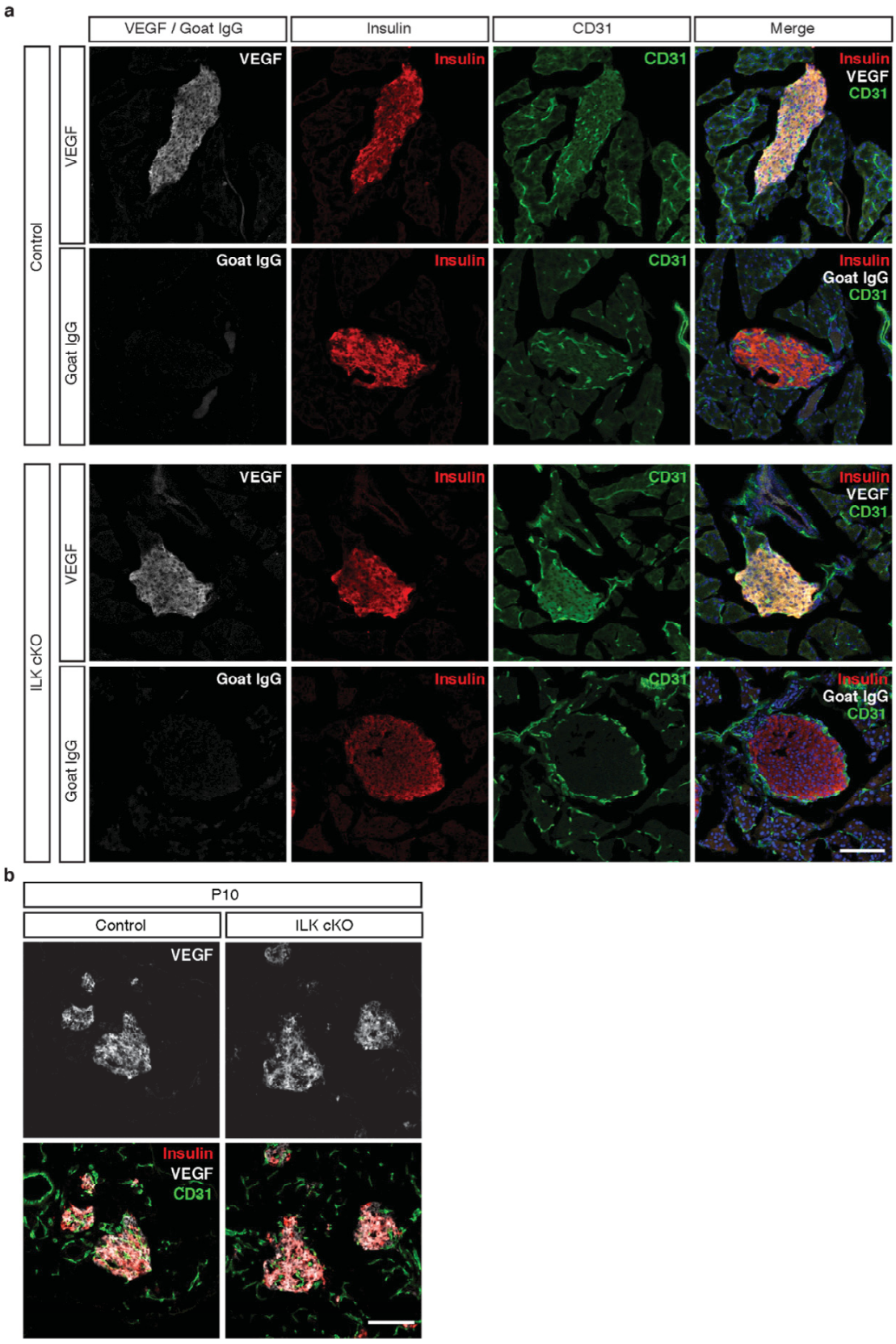

Supplementary Figure 5*: Localization of VEGF-A in ILK cKO pancreas*. (**a**) LSM images of immunofluorescence staining for insulin (red), CD31 (green) and VEGF (white) or Goat IgG (white) in pancreatic sections from adult control and ILK cKO islets. (**b**) LSM images of immunofluorescence staining for insulin (red), CD31 (green) and VEGF (white) in pancreatic sections from 10 days old (P10) control and ILK cKO mice. Scale bars, 100 µm (**a**, **b**).

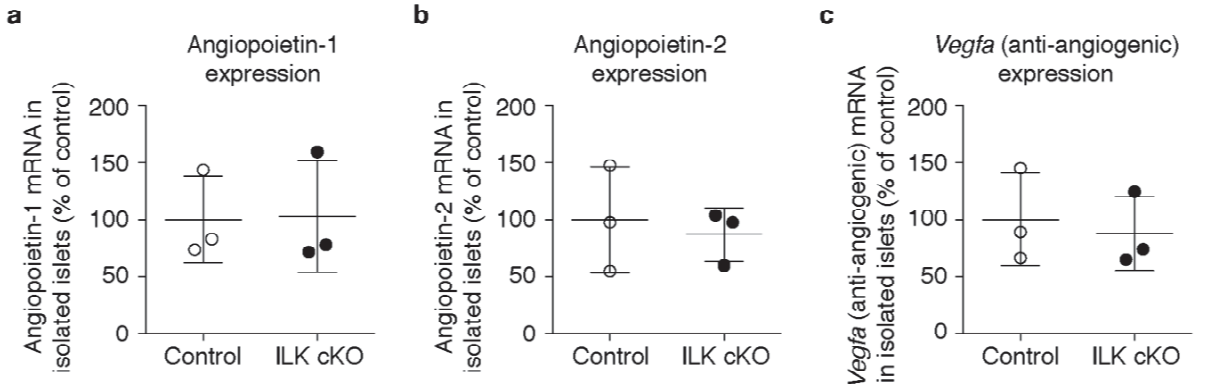

Supplementary Figure 6: ***Expression of pro- and anti-angiogenic factors in ILK cKO islets***. (**a**) Quantification of relative Angiopoietin-1 mRNA expression, (**b**) relative Angiopoietin-2 mRNA expression, and (**c**) relative anti-angiogenic *Vegf-a* mRNA expression in control versus ILK cKO islets. *N* = 3 animals per experimental group each. Data are shown as mean values ± SD, **P* < 0.05 in an unpaired, two-sided Student's t-test.

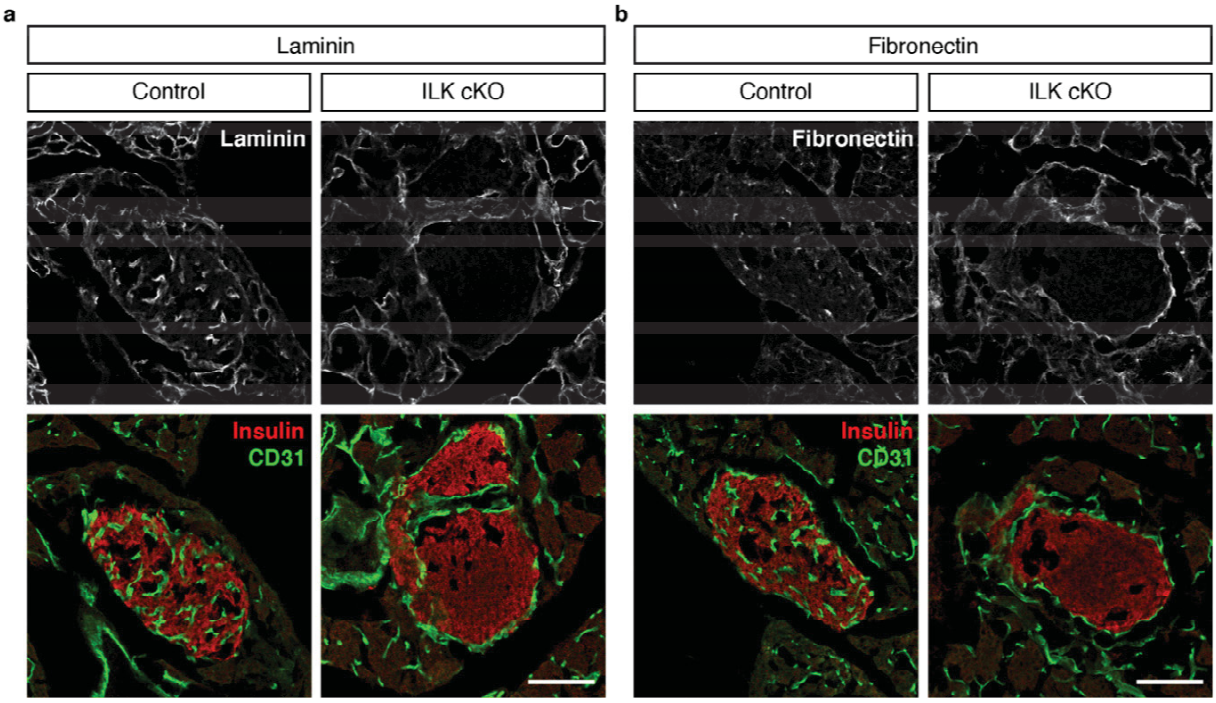

Supplementary Figure 7: ***Basement membrane in adult ILK cKO mice.*** (**a**, **b**) LSM images of immuno-fluorescence staining for laminin (**a**; white) or fibronectin (**b**; white), CD31 (green) and insulin (red) in pancreatic sections from adult control and ILK cKO islets. Scale bars, 100 µm (**a**, **b**).

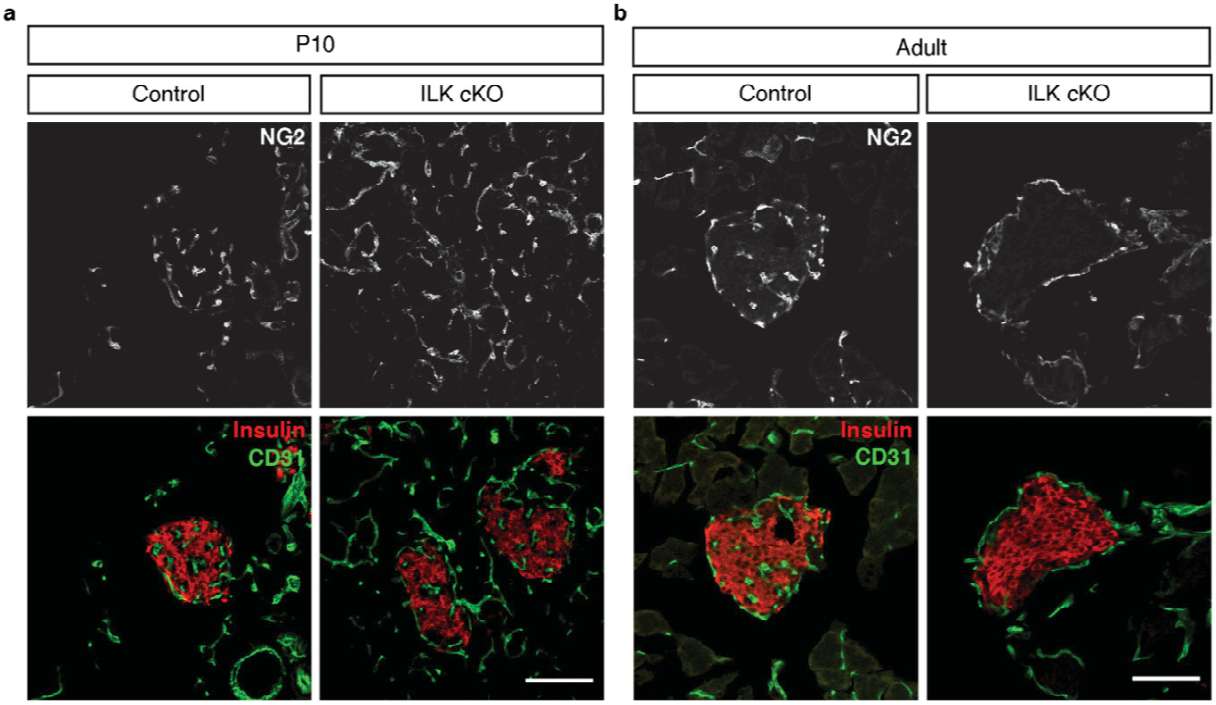

Supplementary Figure 8: ***Staining of pericytes in P10 and adult ILK cKO mice.*** (**a**, **b**) LSM images of immunofluorescence staining for pericyte marker NG2 (white), CD31 (green), and insulin (red) in pancreatic sections from control and ILK cKO islets of 10 days (P10) (**a**) or three week (adult) (**b**) old mice. Scale bars, 100 µm (**a**, **b**).

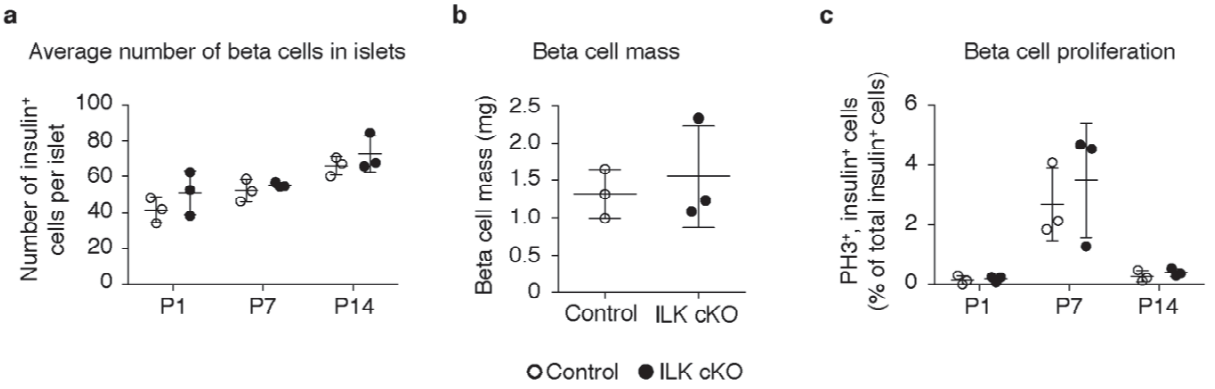

Supplementary Figure 9: ***Quantification of beta cell numbers, mass and proliferation.*** (**a**) Quantification of the average number of beta cells in islets at P1, P7 and P14. *N* = 3 animals per experimental group. Clusters of ≥ 10 insulin$^+$ beta cells were considered as islets for the quantification. 28-39 (P1), 53-114 (P7) and 47-77 (P14) islets were analyzed per animal. (**b**) Beta cell mass per mouse in control and ILK cKO mice. *N* = 3 mice per genotype. (**c**) Quantification of proliferating pancreatic beta cells. Insulin$^+$, PH3$^+$ cells are shown as percentages of the total number of insulin$^+$ cells in islets of pancreatic sections from mice at the age of 1, 7 and 14 days. *N* = 3 animals per experimental group. A total number of 933-2319 (P1), 2646-4852 (P7) and 2976-5183 (P14) insulin$^+$ beta cells were analyzed per animal. Data are shown as mean values ± SD, **P* < 0.05 in an unpaired, two-sided Student's t- test.

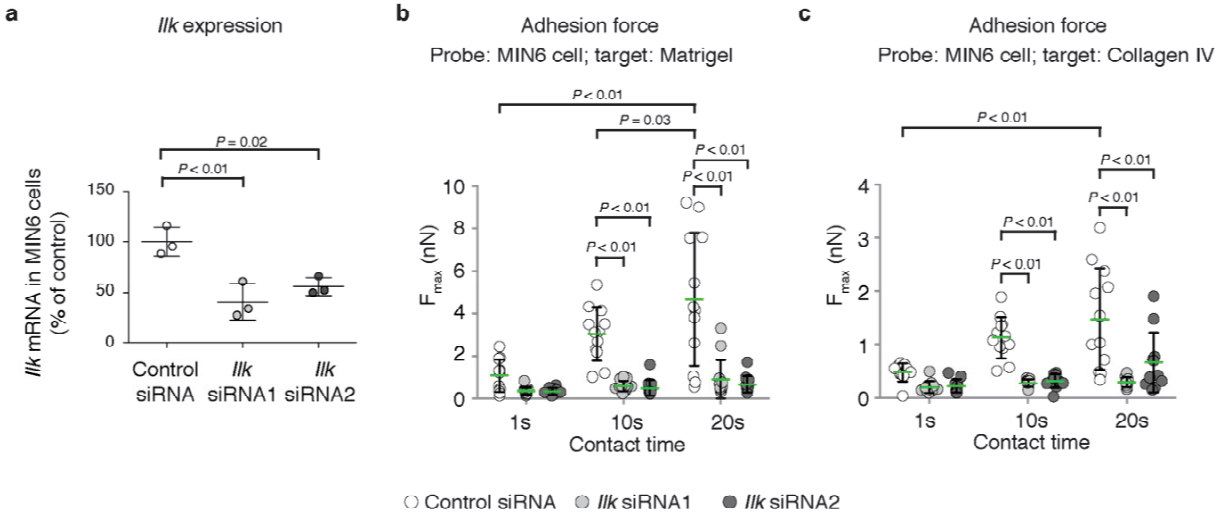

Supplementary Figure 10: ***Requirement of ILK for adhesion to basement membrane.*** (**a**) Quantification of relative *Ilk* mRNA expression in MIN6 cells, a mouse insulinoma cell line treated with either a control siRNA or two siRNAs against *Ilk*. (**b**, **c**) SCFS measurement of the adhesion force between MIN6 cells (probe), treated with either control or two *Ilk* siRNAs, and matrigel (**b**) or collagen IV (**c**) as targets. *N* = 10-13 MIN6 cells versus matrices were tested per experimental condition (contact time and siRNA treatment). The green lines indicate average values. Data are shown as mean values ± SD, **P* < 0.05 in a one-way ANOVA followed by Dunnett's multiple comparisons test (**a**) or a two-way ANOVA followed by Tukey's multiple comparisons test (**b**, **c**).

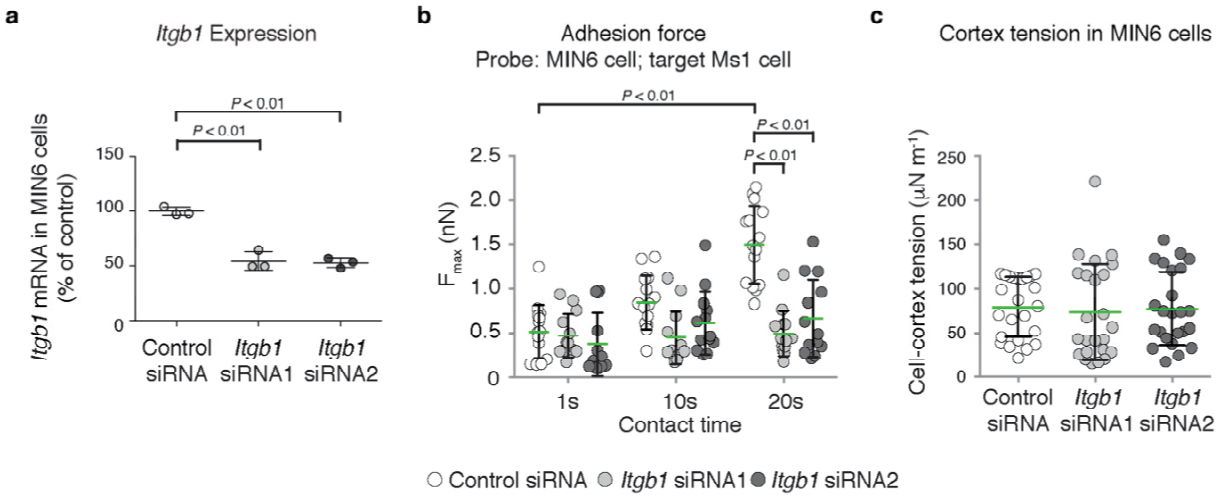

Supplementary Figure 11: ***Adhesion to Ms1 endothelial cells requires β1 integrin.*** (**a**) Quantification of relative β1 integrin (*Itgb1*) mRNA expression in MIN6 cells treated with either a control siRNA or two siRNAs against *Itgb1*. (**b**) SCFS measurements of adhesion force between MIN6 cells (probe), treated with either control or two *Itgb1* siRNAs, and Ms1 endothelial cells (target). *N* = 13-15 MIN6 cells versus 13-15 different Ms1 cells were tested per experimental condition (contact time and siRNA treatment). The green lines indicate average values. (**c**) Colloidal force microscopy measurements of cortex tension in MIN6 cells treated with either a control or two different *Itgb1* siRNAs. *N* = 24 cells were tested per experimental condition (siRNA). Data are shown as mean values ± SD, **P* < 0.05 in a one- way ANOVA followed by Dunnett's multiple comparisons test (**a**), a two-way ANOVA followed by Tukey's multiple comparisons test (**b**) or a one-way ANOVA followed by Tukey's multiple comparisons test (**c**).

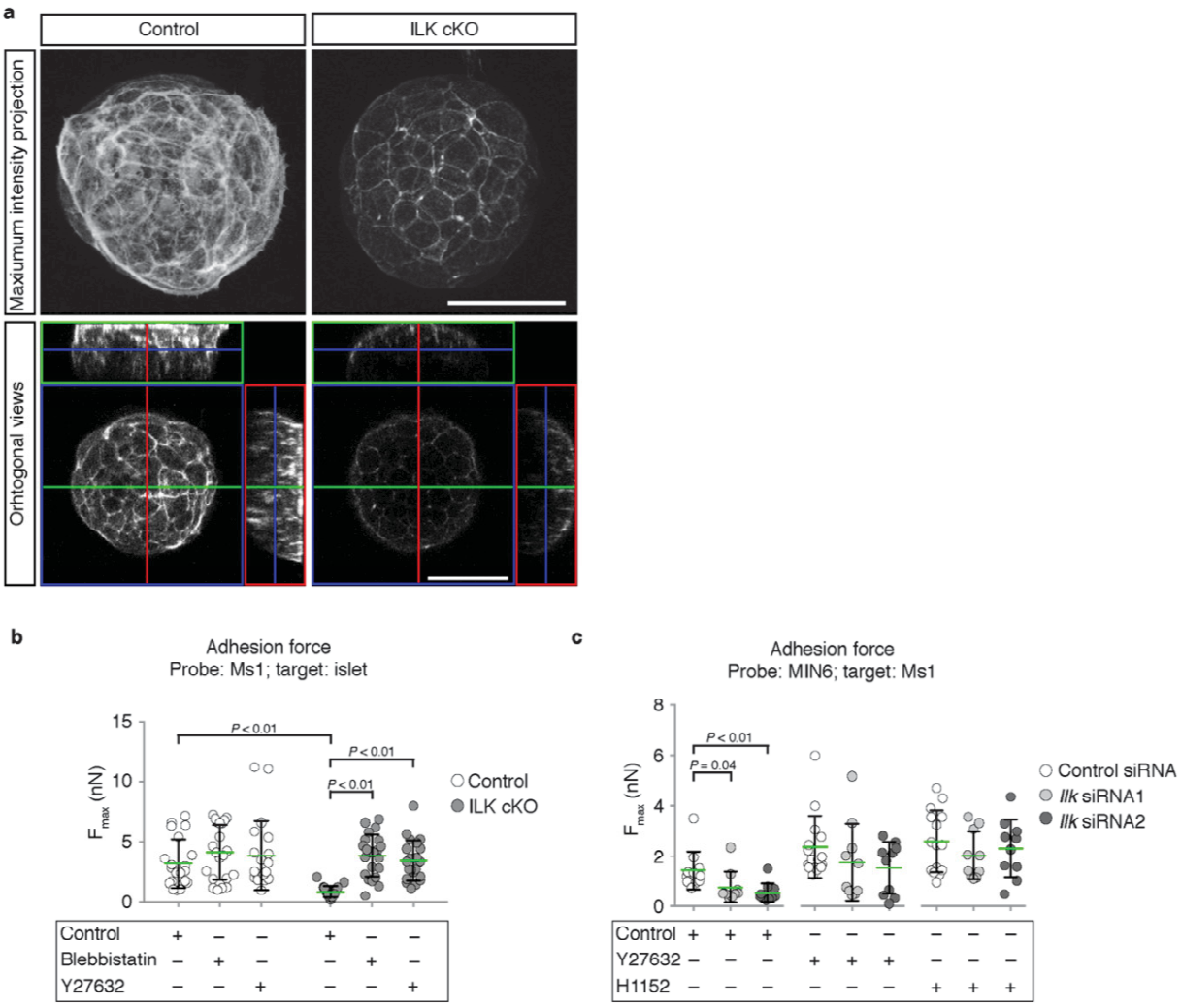

Supplementary Figure 12: ***ILK dependent adhesion to fibronectin and Ms1 endothelial cells via cortical actomyosin.*** (**a**) Maximum intensity projection images of LSM z-stacks from F-actin staining of representative control and ILK cKO islets 7 days after plating on fibronectin. Orthogonal views of LSM z-stacks of F-actin-stained control and ILK cKO islets (blue box). The view in XY plane is presented in the green box and XZ plane the red box. (**b**) SCFS measurements of adhesion forces between Ms1 endothelial cells (probe) and ILK cKO versus control islets (targets) after a contact time of 5 minutes, with or without blebbistatin or Y27632 treatment prior to the experiment. *N* = 20-22 islets were tested for each condition (genotype ± blebbistatin ± Y27632). The green lines indicate average values. (**c**) Adhesion forces between MIN6 cells (probe) and Ms1 cells (target) after a contact time of 20 seconds, with or without treatment with Y27632 or H1152 (both inhibitors of ROCK) prior to the experiment. *N* = 10-15 MIN6 cells versus 10-15 different Ms1 cells were tested per experimental condition (siRNA, ± Y27632, ± H1151). Data are shown as mean values ± SD, **P* < 0.05 in a two-way ANOVA followed by Tukey's multiple comparisons (**b**) or a one-way ANOVA followed by Tukey's multiple comparisons (**c**). Scale bar, 50 µm (**a**).

Supplementary Tables

Supplementary Table 1: ***Islet endothelial cell apoptosis***

		Total ECs	Apoptotic ECs
P7	Control 1	75	1
	Control 2	309	0
	Control 3	269	0
	ILK cKO 1	132	0
	ILK cKO 2	334	0
	ILK cKO 3	193	0
P10	Control 1	300	0
	Control 2	161	0
	Control 3	239	0
	ILK cKO 1	95	0
	ILK cKO 2	104	1
	ILK cKO 3	346	0

Quantification of cleaved caspase-3$^+$ vascular endothelial cells in control and ILK cKO islets from mice at the age of 7 days (P7) and 10 days (P10). *N* = 3 animals per experimental group.

Supplementary Table 2. ***Primer sequences for real-time RT-PCR***

Gene	Sequence
mouse *Ilk* forward	5'-GTGGCTGGACAACACAGAGA-3'
mouse *Ilk* reverse	5'-ATCCCCACGATTCATCACAT-3'
mouse α-tubulin forward	5'-AGAGTCGCGCTGTAAGAAGC-3'
mouse α-tubulin reverse	5'-TCTTCTCACTTGGCATCTGG-3'
mouse *Hprt* forward	5'-CACAGGACTAGAACACCTGC-3'
mouse *Hprt* reverse	5'-GCTGGTGAAAAGGACCTCT-3'
mouse *Vegfa* forward	5'-CAAGATCCGCAGACGTGTAA-3'
mouse *Vegfa* reverse	5'-TTAATCGGTCTTTCCGGTGA-3'
mouse "antiangiogenic" *Vegfa* forward	5'-GGACACATTAGGGGGTGTTG-3'
mouse "antiangiogenic" *Vegfa* reverse	5'-GGTGAGAGGTCTGCAAGTACGTT-3'
mouse Angiopoietin 1 forward	5'-CAGCACGAAGGATGCTGATA-3'
mouse Angiopoietin 1 reverse	5'-ATGGTGGTGGAACGTAAGGA-3'
mouse Angiopoietin 2 forward	5'-GCACAAAGGATTCGGACAAT-3'
mouse Angiopoietin 2 reverse	5'-ATCATGGTTGTGGCCTTGAG-3'
mouse *Itgb1* forward	5'-AATGCCAAGTGGGACACGGG -3'
mouse *Itgb1* reverse	5'-TGACTAAGATGCTGCTGCTGTGAGC-3'

9.3 Supplementary information of section 5.3

This section contains the supplementary information of the paragraph 5.3 “Induced beta cell proliferation in *Ilk* knockout mice”.

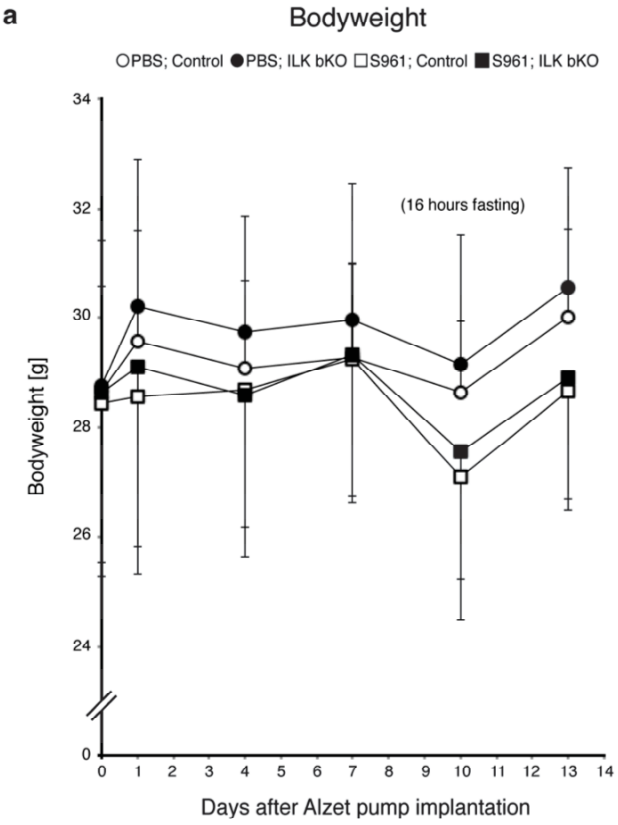

Supplementary Figure 13: ***Bodyweights of control and ILK bKO mice.*** (**a**) Bodyweights of mice before and after Alzet pump implantation. At day 10 all mice fasted for 16 hours, since a glucose tolerance test was performed at this day (see 5.3.4.6). $N \geq 5$ animals per experimental group. All values are shown as means ± SD; statistical significance ($^*P < 0.05$) was determined by unpaired two-tailed Student’s t-test.

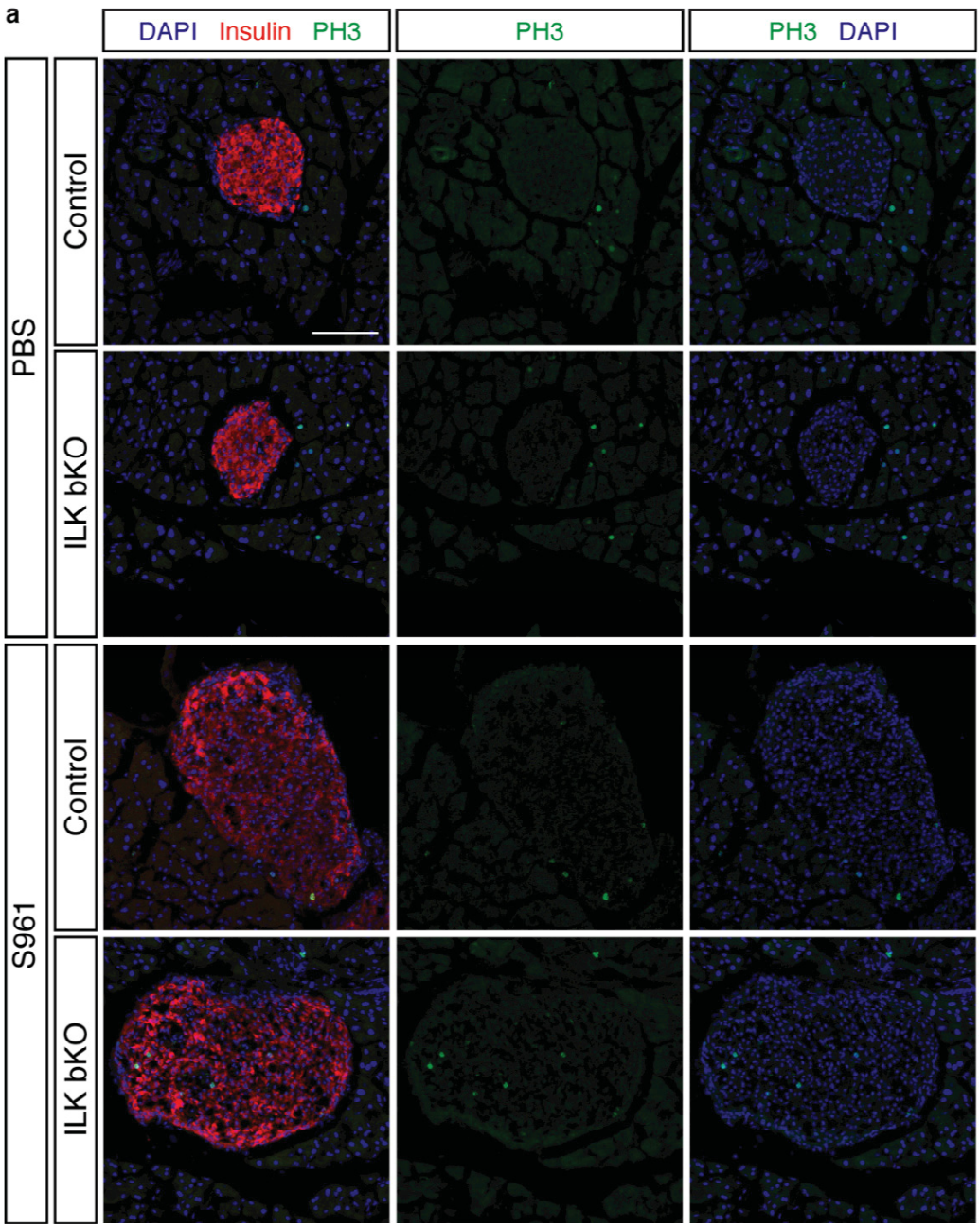

Supplementary Figure 14: ***ILK in beta cells supports beta cell proliferation during insulin resistance.*** **(a)** Representative laser scanning microscope immunofluorescence images stained for insulin (beta cells, red), Dapi (nuclei, blue) and PH3 (proliferating cells, green) of control and ILK bKO mice with either PBS or S961 filled Alzet pumps. Quantification of proliferating (PH3-positive) beta cells is presented in Figure 15c. $N \geq 5$ mice per experimental group. Scale bar, 100 µm.

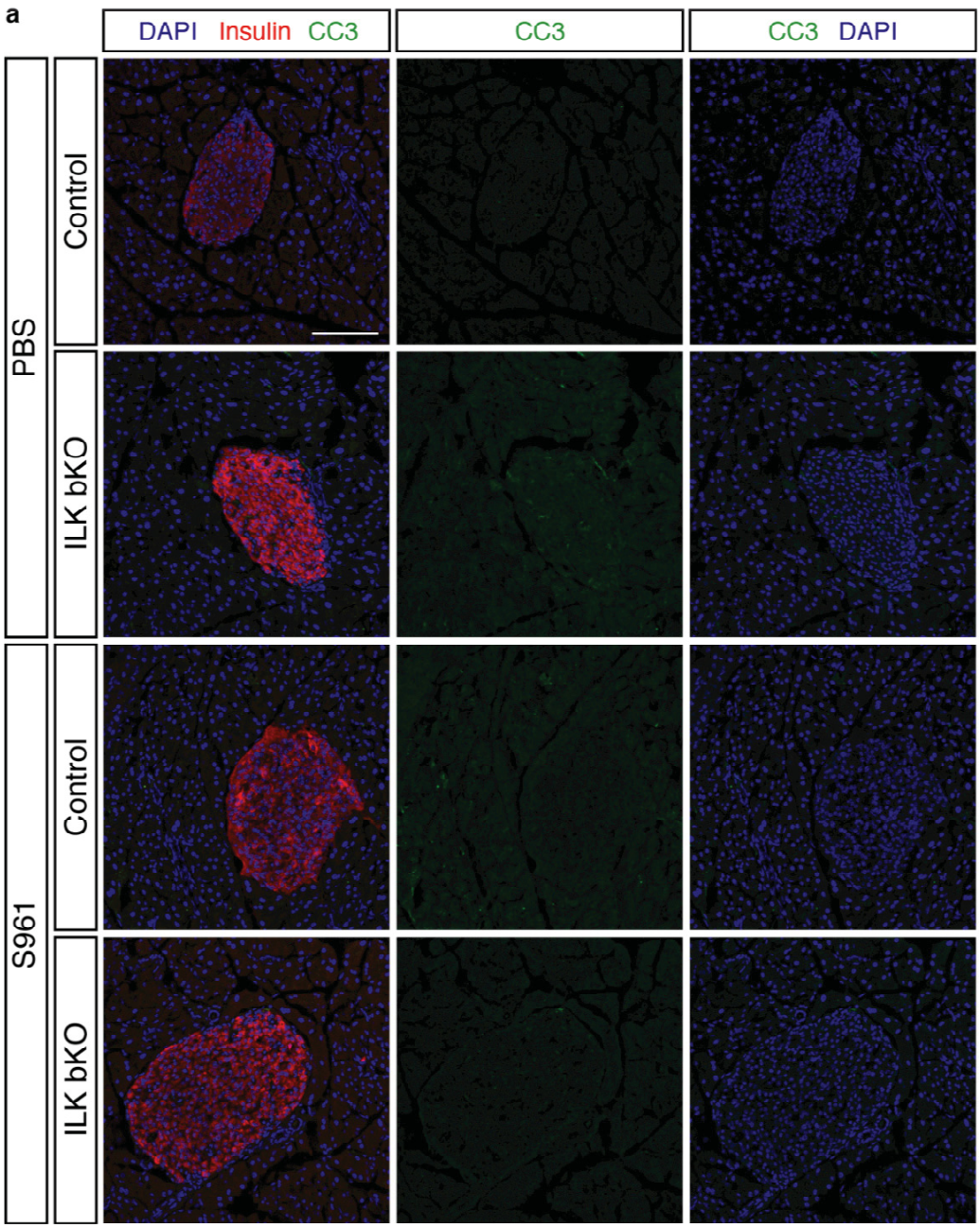

Supplementary Figure 15: ***No beta cell apoptosis is detected in insulin resistant ILK bKO mice.*** **(a)** Representative LSM immunofluorescence images stained for insulin (beta cells, red), Dapi (nuclei, blue) and Cleaved caspase-3 (CC3) (apoptotic cells, green) of control and ILK bKO mice with either PBS or S961 filled Alzet pumps. Quantification of apoptotic (CC3-positive) beta cells is presented in Figure 15d. $N \geq 5$ mice per experimental group. Scale bar, 100 µm.

Statutory declaration

I hereby declare that I wrote the dissertation “Einfluss der Integrin-Linked Kinase auf die Vaskularisierung von Langerhans-Inseln und die Blutglukose Homöostase” independently and without other resources as indicated in compliance with “Grundsätze zur Sicherung guter wissenschaftlicher Praxis an der Heinrich-Heine-Universität Düsseldorf”.

Furthermore, I declare that I did not submit this dissertation, either in full or in part, to any other academic institution and did not absolve any promotion trials before.

Düsseldorf,

_____

Haiko Karsjens

Eidesstattliche Erklärung

Ich versichere an Eides Statt, dass die Dissertation „Einfluss der Integrin-Linked Kinase auf die Vaskularisierung von Langerhans-Inseln und die Blutglukose Homöostase” von mir selbstständig und ohne unzulässige fremde Hilfe unter Beachtung der „Grundsätze zur Sicherung guter wissenschaftlicher Praxis an der Heinrich-Heine-Universität Düsseldorf“ erstellt worden ist.

Darüber hinaus versichere ich, dass ich die Dissertation weder in der hier vorgelegten noch in einer ähnlichen Form bei einem anderen Institut eingereicht habe und bisher keine Promotionsversuche unternommen habe.

Düsseldorf, den

_____

Haiko Karsjens

Acknowledgements

First of all, I would like to thank my supervisor Eckhard Lammert for introducing me into the field of angiogenesis and diabetes and for giving me the opportunity to write not only my bachelors and masters but also my PhD thesis in his lab. I am very grateful for your supervision, guidance and financial support.

Furthermore, I would like to thank Volker Burkart for being my second supervisor. For helpful comments and an enjoyable supervision.

I want to thank Jan Eglinger for being a great supervisor during my bachelors and masters thesis, which paved the way for my PhD.

I also want to thank Martin Kragl for handing over his exciting topic.

I want to thank all members of the institute of Metabolic Physiology at the Heinrich Heine University as well as all members of the institute for Vascular and Islet Cell Biology at the German diabetes center (DDZ). Especially, Barbara B., Silke J. & Andrea K. for all experimental but also all other kind of support. My buddy Jessi M., for all help, laugh and fun. Okka S. for experimental help and lots of fun (also outside the lab). Anna B. for sharing countless Mensa-dates. Daniel E. & Silke O. for all your help, especially during the stressful revision. Carina H. for showing me the Alzet pump operation. All other members of the institute: Esther H., Linda L., Laura W. Laura H., Fatma D., Astrid W., Tobi B., Alena W., Molly K-G., Lara P-P. and Martin Z.. Celina U. and Oksana L. for being diligent students. Furthermore, I want to thank Bengt-F. B., Kerstin G., Caro P., Nadine M. & Michael R. for making my life at the DDZ as enjoyable as possible.

A big thank to Sofia U., my neighbor and ILK partner, for all help, assistance and support during my PhD.

I want to thank Lauge Schäffer (from Novo Nordisk) who kindly gifted S961.
Rajib S. for an intense and successful revision.

I want to thank my family. My parents and my sisters who always believed in me.

Last but not least I want to thank all my friends, who made the recent years in Düsseldorf to a memorable time.